

PREDICTION OF GROUND BORNE VIBRATIONS  
DUE TO RAILWAY TRAFFIC

A THESIS SUBMITTED TO  
THE GRADUATE SCHOOL OF NATURAL AND APPLIED SCIENCES  
OF  
MIDDLE EAST TECHNICAL UNIVERSITY

BY

SALİH ALAN

IN PARTIAL FULFILMENT OF THE REQUIREMENTS  
FOR  
THE DEGREE OF DOCTOR OF PHILOSOPHY  
IN  
MECHANICAL ENGINEERING

JUNE 2016



Approval of the thesis:

**PREDICTION OF GROUND BORNE VIBRATIONS  
DUE TO RAILWAY TRAFFIC**

submitted by **SALİH ALAN** in partial fulfillment of the requirements for the degree of **Doctor of Philosophy in Mechanical Engineering Department, Middle East Technical University** by,

Prof. Dr. Gülbin Dural Ünver  
Dean, Graduate School of **Natural and Applied Sciences**

Prof. Dr. R. Tuna Balkan  
Head of Department, **Mechanical Engineering**

Prof. Dr. Mehmet Çalışkan  
Supervisor, **Mechanical Engineering Dept., METU**

**Examining Committee Members:**

Assoc. Prof. Dr. Ender Ciğeroğlu  
Mechanical Engineering Dept., METU

Prof. Dr. Mehmet Çalışkan  
Mechanical Engineering Dept., METU

Assoc. Prof. Dr. Ayşegül Askan Gündoğan  
Civil Engineering Dept., METU

Prof. Dr. K. Levend Parnas  
Mechanical Engineering Dept., TED University

Assoc. Prof. Dr. M. Bülent Özer  
Mechanical Engineering Dept., TOBB ETU

**Date:** 23.06.2016

**I hereby declare that all information in this document has been obtained and presented in accordance with academic rules and ethical conduct. I also declare that, as required by these rules and conduct, I have fully cited and referenced all material and results that are not original to this work.**

Name, Last Name : Salih ALAN

Signature :

## **ABSTRACT**

### **PREDICTION OF GROUND BORNE VIBRATIONS DUE TO RAILWAY TRAFFIC**

Alan, Salih

Ph.D., Department of Mechanical Engineering  
Supervisor: Prof. Dr. Mehmet Çalışkan

June 2016, 144 pages

The aim of this thesis is to analyze the ground borne vibrations originating from railway traffic. A numerical prediction model is developed and elements of the railway structure are analyzed for ground vibrations due to railway traffic. The proposed prediction model is a time domain three-dimensional model.

Modal parameters of track-and-ground-coupled structure and railway vehicle are obtained by modal analyses. Impulse response functions are calculated from modal parameters. The vibration responses are predicted by these impulse response functions. Modal coupling techniques are introduced to couple dynamic subsystems involving soil layers and track. Wave motion in ground layers are formulated by finite difference equations. A fourth-order staggered grid is implemented to extract system matrices from which modal parameters are obtained through eigenvalue analysis. Rayleigh damping model is implemented in time domain, for track and ground modeling.

The developed model is compared and validated with in situ measurements available in literature. Time domain and frequency domain results as well as vibration indicators such as root mean square velocity level, peak particle velocity and maximum weighted severity predictions are shown to be in good agreement with existing measurement results taken from literature.

Parametric studies of vehicle, track and ground parameters on ground vibration levels are presented. Ground vibration levels are compared for variation of the parameters: train type, train speed, rail unevenness, rail profile, sleeper spacing, ballast, subballast and subgrade stiffness, embankment material, Young's modulus, Poisson's ratio, density and damping ratio of ground layers. Effects of mitigation applications on ground vibration levels are analyzed. Under sleeper pad, under ballast mat and trench applications are modeled.

The modular structure of the proposed method enables the user to modify and analyze the coupled system without going through the burden of remodeling of all the subsystems. This results in considerable reduction in computational times.

**Keywords:** Railway Vibration, Ground Vibrations, Finite Element Method, Finite Difference Method, Modal Coupling

## ÖZ

### DEMİRYOLU TRAFİĞİ KAYNAKLI ZEMİN TİTREŞİMİNİN TAHMİNİ

Alan, Salih

Doktora, Makine Mühendisliği Bölümü  
Tez Yöneticisi: Prof. Dr. Mehmet Çalışkan

Haziran 2016, 144 sayfa

Bu tez çalışmasında demiryolu ulaşımından kaynaklanan zemin titreşiminin araştırılması amaçlanmaktadır. Bir sayısal tahmin modeli geliştirilmektedir ve demiryolu yapısal elemanlarının zemin titreşimine etkileri incelenmektedir. Sunulan tahmin modeli zaman tanım alanında ve üç boyutlu bir modeldir.

Modal analiz işlemleriyle, hat ve zemin birleşik yapısı için ve demiryolu taşıtı için modal parametreler elde edilmektedir. Modal parametreler kullanılarak darbe tepki fonksiyonları hesaplanmaktadır. Bu darbe tepki fonksiyonları aracılığı ile titreşim tepkileri tahmin edilmektedir. Sistem alt elemanlarının birleştirilmesi için modal birleştirme sunulmaktadır. Zemin katmanlarındaki dalga hareketi sonlu farklar denklemleriyle formüle edilmiştir. Dördüncü mertebeden şaşırtmalı nokta ağı uygulanarak sistem matrisleri elde edilmiştir. Bu sistem matrislerinin özdeğer analizinden modal parametreler bulunmuştur. Hat ve zemin modellenmesinde, Rayleigh sönümlenme modeli zaman tanım alanında uygulanmıştır.

Geliştirilen yöntem literatürde verilmiş olan ölçüm sonuçlarıyla doğrulanmıştır. Zaman ve frekans tanım alanındaki sonuçlarla birlikte, titreşim hızı ortalama karekök değeri, tepe titreşim hızı değeri ve en yüksek ağırlıklı titreşim şiddeti değeri gibi titreşim göstergeleri karşılaştırılmış ve tahminlerin ölçüm sonuçlarıyla uyumlu olduğu gösterilmiştir.

Hat ve taşıt parametrelerinin zemin titreşim düzeylerine etkisi parametrik analizlerle araştırılmıştır. Zemin titreşim düzeyleri şu parametrelerdeki değişim için karşılaştırılmıştır: tren tipi, tren hızı, ray pürüzlülüğü, ray profili, travers aralığı, balast, balast altı ve alt temel direngenliği, toprak dolgu malzemesi, zemin katmanlarının Young modülü, Poisson oranı, yoğunluğu ve sönümlenme oranı. Değişik yalıtım uygulamalarının zemin titreşim düzeylerine etkisi incelenmiştir. Travers altı pedi, balast altı şiltesi ve hat boyunca hendek uygulamaları modellenmiştir.

Önerilen yöntemin modüler yapısı sayesinde, demiryolu yapısının tüm alt sistemlerinin en baştan modellenmesine gerek duyulmadan, birleşik sistem sadece gerekli bileşenlerin etkisi için değiştirilip analiz edilebilmektedir. Bu durum hesaplama sürelerinde önemli bir azalma sağlamaktadır.

**Anahtar kelimeler:** Demiryolu Titreşimi, Zemin Titreşimleri, Sonlu Eleman Yöntemi, Sonlu Fark Yöntemi, Modal Birleştirme

Babam Durali Alan'ın anısına

## ACKNOWLEDGEMENTS

I would like to express my sincere gratitude to my supervisor, Prof. Dr. Mehmet Çalışkan, for his invaluable supervision, advice, criticism and support that made this study possible.

Discussions with Prof. Dr. K. Önder Çetin, Assoc. Prof. Dr. Ender Cigeroğlu and Assoc. Prof. Dr. Ayşegül Askan Gündoğan are gratefully acknowledged.

I would like to thank the Scientific and Technological Research Council of Turkey (TÜBİTAK) for the scholarship with the code BİDEB 2211.

I would like to express my special thanks to my friends Bekir Bediz and Hakan Çalışkan for their insightful comments and great help throughout the whole thesis study.

I want to thank my friends in the department as well as my puzzle friends for their encouragement and help. My friend Serdar Hiçdurmaz made valuable contribution by sharing his computer for a couple of runs. I have to also thank my rehearsal listeners.

I am in debt to my family for their love and support in my long educational career.

## TABLE OF CONTENTS

ABSTRACT .....	v
ÖZ .....	vii
ACKNOWLEDGEMENTS .....	x
TABLE OF CONTENTS .....	xi
LIST OF TABLES .....	xiv
LIST OF FIGURES .....	xv
LIST OF SYMBOLS AND ABBREVIATIONS .....	xix
CHAPTERS	
1 INTRODUCTION .....	1
1.1 Motivation .....	1
1.2 Objectives and research contribution .....	2
1.3 Scope of the thesis .....	3
2 REVIEW OF RAILWAY INDUCED GROUND VIBRATIONS .....	5
2.1 Vibration generation .....	5
2.2 Rail surface irregularity .....	6
2.3 Wave propagation through railway track .....	6
2.4 Wave propagation in ground layers .....	7
2.5 Assessment of vibrations .....	8
2.6 Prediction models .....	10

2.7	Vibration measurements .....	17
2.8	Effects of track and ground parameters on vibration .....	18
2.9	Vibration mitigation techniques .....	19
2.10	Conclusion .....	19
3	THEORETICAL BACKGROUND .....	21
3.1	Response to arbitrary excitation by convolution .....	21
3.2	Modal parameters for an undamped system .....	22
3.3	Unit impulse response function for an undamped system.....	23
3.4	Modal parameters for a damped system .....	25
3.5	Damped modes from undamped modes and damping properties.....	27
3.6	Unit impulse response function for a damped system.....	34
3.7	Modal coupling.....	37
3.8	Fixed boundary application by modal coupling .....	40
3.9	Damping boundary application by modal coupling .....	41
3.10	Selection of degrees of freedom for modal coupling .....	43
3.11	Modal parameters for proportional material properties.....	43
4	FINITE DIFFERENCE FORMULATION .....	47
4.1	Governing equations.....	47
4.2	Staggered grid modeling.....	49
4.3	Finite difference formulation for general equations .....	50
4.4	Boundary conditions.....	51
4.5	Implementation of equations .....	55
4.6	Mesh size comparison and convergence considerations .....	58
4.7	Concluding remarks.....	60
5	NUMERICAL MODELING .....	61
5.1	Multibody vehicle modeling.....	61

5.2 Rail wheel contact modeling .....	63
5.3 Finite element modeling of track .....	64
5.4 Finite difference modeling of ground layers .....	67
5.5 Impulse response function calculations .....	72
5.6 Response calculations .....	73
5.7 Computational details .....	75
6 VALIDATION OF PREDICTION MODEL.....	79
6.1 Thalys high speed train at Leuze-en-Hainaut, 2012.....	79
6.2 Thalys high speed train at Mévergnies, 2005.....	87
7 PARAMETRIC STUDY FOR GROUND VIBRATION.....	93
7.1 Reference parameters .....	93
7.2 Effects of vehicle parameters on ground vibration .....	96
7.3 Effects of track parameters on ground vibration.....	103
7.4 Effects of ground parameters on ground vibration .....	114
8 VIBRATION MITIGATION APPLICATIONS .....	123
8.1 Under sleeper pad application.....	123
8.2 Under ballast mat application.....	125
8.3 Trench application.....	127
9 CONCLUSIONS.....	129
9.1 Summary and conclusions .....	129
9.2 Recommendations for future work .....	136
REFERENCES.....	139
CURRICULUM VITAE .....	143

## LIST OF TABLES

### TABLES

Table 5-1. Computation times for steps in reference study.....	76
Table 6-1. Soil properties for Leuze-en-Hainaut 2012 [51] .....	80
Table 6-2. Ballasted track parameters [33].....	80
Table 6-3. Ballasted track mechanical properties [33].....	81
Table 6-4. Vehicle parameters for Thalys HST [45].....	81
Table 6-5. Soil properties for Mévergnies 2005 [26] .....	88
Table 7-1. Reference ballasted railway track mechanical properties .....	94
Table 7-2. Reference ballasted railway track properties .....	94
Table 7-3. Soil properties for reference study .....	95
Table 7-4. Parameters for Eurostar high speed train [45] .....	97
Table 7-5. Parameters for freight train [54].....	97
Table 7-6. Parameters for German Intercity Express (ICE) [45] .....	98
Table 7-7. Parameters for T2000 tram [45].....	98
Table 7-8. Axle loads for train types [45], [54].....	99
Table 7-9. Parameters for different rail profiles .....	106
Table 7-10. Parameters for different rail pads.....	108
Table 7-11. Young's modulus value for track components.....	111
Table 7-12. Parameters for embankment layers analyzed.....	113
Table 7-13. Young's modulus values for analyzed ground layers .....	115
Table 8-1. Parameters for under sleeper pads used in the analyses.....	123
Table 8-2. Parameters for under ballast mats used in the analyses .....	125

## LIST OF FIGURES

### FIGURES

Figure 3-1. Subsystems for modal coupling .....	37
Figure 4-1. Three-dimensional staggered grid .....	49
Figure 4-2. Finite difference nodes for normal stress components .....	50
Figure 4-3. Nodes for W-AFDA (left) and H-AFDA (right) formulations.....	52
Figure 4-4. Ground model.....	58
Figure 4-5. Modal analysis results for different mesh sizes.....	59
Figure 4-6. Modal analysis results for different mesh sizes.....	59
Figure 5-1. Typical three degree of freedom vehicle model.....	61
Figure 5-2. Rail wheel contact model .....	64
Figure 5-3. Rail pad model.....	65
Figure 5-4. Finite element model for track .....	66
Figure 5-5. Undamped modal analysis of track model in ANSYS .....	66
Figure 5-6. Modification of track modal parameters for material damping and rail pad damping application .....	67
Figure 5-7. Ground model.....	67
Figure 5-8. Calculation steps for soil layer 1 .....	68
Figure 5-9. Coupling of ground layers .....	69
Figure 5-10. Fixing coordinates on coupled ground model .....	70
Figure 5-11. Modification of undamped ground modes for damping.....	70
Figure 5-12. Local damping boundary coordinates on coupled ground model .....	71
Figure 5-13. Coupled ground track model .....	71
Figure 5-14. Response coordinates on coupled ground track model .....	72
Figure 5-15. Coupled ground and track model with vehicle response nodes .....	73
Figure 5-16. Initial positions of wheels .....	74
Figure 5-17. Position of wheels at an arbitrary step of calculations .....	74

Figure 6-1. Thalys HST configuration [26] .....	81
Figure 6-2. Vertical velocity time history 9 m from track center .....	82
Figure 6-3. Vertical velocity time history 11 m from track center .....	82
Figure 6-4. Vertical velocity frequency content at 9 m from track center .....	83
Figure 6-5. Vertical frequency content at 11 m from track center .....	83
Figure 6-6. Vertical velocity VdB variation with distance from track center .....	84
Figure 6-7. Longitudinal velocity VdB variation with distance from track center ....	85
Figure 6-8. Horizontal velocity VdB variation with distance from track center.....	85
Figure 6-9. Vertical velocity (r.m.s.) variation with distance from track center.....	86
Figure 6-10. Longitudinal velocity (r.m.s.) variation with distance from track center .....	86
Figure 6-11. Horizontal velocity (r.m.s.) variation with distance from track center .	87
Figure 6-12. Vertical velocity time history 7 m from track center, left: predicted, right: measurement [26] .....	89
Figure 6-13. Vertical velocity time history 15 m from track center, left: predicted, right: measurement [26] .....	89
Figure 6-14. Weighted severity ( $KB_F$ ) of vertical ground vibration 7 m from track center, left: predicted, right: measurement [26] .....	89
Figure 6-15. Weighted severity ( $KB_F$ ) of vertical ground vibration 15 m from track center, left: predicted, right: measurement [26] .....	90
Figure 6-16. Vertical velocity frequency content at 7 m from track center, left: predicted, right: measurement [26] .....	90
Figure 6-17. Vertical velocity frequency content at 15 m from track center, left: predicted, right: measurement [26] .....	91
Figure 6-18. Peak particle velocity (PPV) variation with distance from track center	91
Figure 6-19. Maximum weighted severity ( $KB_{F,max}$ ) variation with distance from track center .....	92
Figure 7-1. Vertical peak particle velocity (PPV) variation with distance from track center .....	95
Figure 7-2. Maximum weighted severity ( $KB_{F,max}$ ) variation for vertical velocity with distance from track center .....	96
Figure 7-3. Configuration for Eurostar high speed train [45] .....	97

Figure 7-4. Configuration for freight train [54] .....	97
Figure 7-5. Configuration for German Intercity Express (ICE) [45] .....	98
Figure 7-6. Configuration for T2000 tram [45] .....	98
Figure 7-7. $KB_{F,max}$ variation with distance for different train types .....	100
Figure 7-8. PPV variation with distance for different train types .....	100
Figure 7-9. $KB_{F,max}$ variation with distance for different train types considering axle loads .....	101
Figure 7-10. PPV variation with distance for different train types considering axle loads .....	101
Figure 7-11. $KB_{F,max}$ variation with distance for different train speeds .....	102
Figure 7-12. PPV variation with distance for different train speeds .....	103
Figure 7-13. Rail profiles for different unevenness classes .....	104
Figure 7-14. $KB_{F,max}$ variation with distance for different unevenness classes .....	104
Figure 7-15. PPV variation with distance for different unevenness classes .....	105
Figure 7-16. Frequency content of vibration response at 11 m from track, for different rail unevenness classes .....	106
Figure 7-17. $KB_{F,max}$ variation with distance for different rail profiles .....	107
Figure 7-18. PPV variation with distance for different rail profiles .....	107
Figure 7-19. $KB_{F,max}$ variation with distance for different rail pads .....	108
Figure 7-20. PPV variation with distance for different rail pads .....	109
Figure 7-21. $KB_{F,max}$ variation with distance for different sleeper spacing values ..	110
Figure 7-22. PPV variation with distance for different sleeper spacing values .....	110
Figure 7-23. $KB_{F,max}$ variation with distance for different track stiffness values ....	111
Figure 7-24. PPV variation with distance for different track stiffness values .....	112
Figure 7-25. $KB_{F,max}$ variation with distance for different embankment materials .	113
Figure 7-26. PPV variation with distance for different embankment materials .....	114
Figure 7-27. $KB_{F,max}$ variation with distance for different Young's modulus values of ground model .....	115
Figure 7-28. PPV variation with distance for different Young's modulus values of ground model .....	116
Figure 7-29. $KB_{F,max}$ variation with distance for different Poisson's ratio values of ground model .....	117

Figure 7-30. PPV variation with distance for different Poisson's ratio values of ground model.....	117
Figure 7-31. $KB_{F,max}$ variation with distance for different density values of ground model.....	118
Figure 7-32. PPV variation with distance for different density values of ground model.....	119
Figure 7-33. $KB_{F,max}$ variation with distance for different ground damping models	120
Figure 7-34. PPV variation with distance for different ground damping models ....	120
Figure 8-1. $KB_{F,max}$ variation with distance for different under sleeper pad models	124
Figure 8-2. PPV variation with distance for different under sleeper pad models ....	124
Figure 8-3. $KB_{F,max}$ variation with distance for different under ballast mat models	126
Figure 8-4. PPV variation with distance for different under ballast mat models.....	126
Figure 8-5. $KB_{F,max}$ variation with distance for trench application .....	128
Figure 8-6. PPV variation with distance for trench application .....	128

## LIST OF SYMBOLS AND ABBREVIATIONS

$\alpha$	Alpha damping ratio
$\beta$	Beta damping ratio
$\delta(t)$	Unit impulse function
$\zeta_r$	$r^{th}$ damping ratio
$\{\eta\}$	Displacement vector in modal coordinates
$\{\dot{\eta}\}$	Velocity vector in modal coordinates
$\{\ddot{\eta}\}$	Acceleration vector in modal coordinates
$\{\eta_r\}$	Displacement vector for $r^{th}$ mode
$[\eta_A]$	Modal coordinate vector for subsystem A
$\eta_d$	Dependent modal coordinates
$\eta_i$	Independent modal coordinates
$\lambda$	Lamé constant
$\lambda_r$	$r^{th}$ eigenvalue
$\lambda^*$	Frequency of state space variables
$\lambda_r^*$	$r^{th}$ eigenvalue in state space
$\bar{\lambda}_r^*$	Complex conjugate of $r^{th}$ eigenvalue in state space
$[\cdot \lambda^* \cdot]$	Diagonal eigenvalue matrix in state space
$\mu$	Lamé constant
$\nu$	Poisson's ratio
$\rho$	Density
$\phi$	Spatial frequency
$\phi_1$	Break spatial frequency
$\phi_2$	Break spatial frequency
$[\phi]$	Modal matrix
$\{\phi_r\}$	Mass normalized $r^{th}$ mode shape
$[\phi^*]$	Modal matrix in state space
$\{\phi_r^*\}$	Normalized $r^{th}$ eigenvector in state space

$[\phi_A]$	Modal matrix for subsystem A
$\psi$	Phase angle
$\{\psi^*\}$	Spatial component of state variables
$\{\psi_r^*\}$	$r^{th}$ eigenvector in state space
$\{\bar{\psi}_r^*\}$	Complex conjugate of $r^{th}$ eigenvalue in state space
$\omega$	Frequency
$\omega_r$	$r^{th}$ natural frequency
$[\cdot \omega_r^2 \cdot]$	Diagonal eigenvalue matrix
$\omega_{rd}$	$r^{th}$ damped natural frequency
$[\cdot \omega_{r,A}^2 \cdot]$	Eigenvalues for subsystem A
$\omega_{r,C}^2$	Eigenvalues of the coupled system
$\Delta_{st}$	Static deflection in contact spring
$\Delta t$	Time increment
$[\Psi]$	Mode shape for the overall system
$a(t)$	Acceleration history
$c_1$	Primary suspension damping coefficient
$c_2$	Secondary suspension damping coefficient
$f$	Frequency
$f_0$	Cut off frequency
$f(t)$	Forcing function
$g$	Gravitational acceleration
$h_{ij}(t)$	Unit impulse response function
$h_{r,ij}^*$	Unit impulse response function component
$\bar{h}_{r,ij}^*$	Unit impulse response function component
$k_1$	Primary suspension stiffness coefficient
$k_2$	Secondary suspension stiffness coefficient
$k_H$	Hertzian contact stiffness coefficient
$m_b$	Bogie mass
$m_c$	Car body mass
$m_w$	Wheel mass
$m_r$	$r^{th}$ modal mass
$\{p\}$	Independent modal coordinates vector

$r$	Rail unevenness
$rb$	Number of rigid body modes
r.m.s.	Root-mean-square
$t$	Time
$u$	Displacement in x-direction
$\{u\}$	Displacement vector in spatial coordinates
$\{\dot{u}\}$	Velocity vector in spatial coordinates
$\{\ddot{u}\}$	Acceleration vector in spatial coordinates
$\{u_r\}$	$r^{th}$ mode shape
$\{u_r^*\}$	$r^{th}$ mode shape in state space
$\{u_i\}$	Components of spatial displacement vector
$v$	Displacement in y-direction
$\{v_r^*\}$	Velocity components of $r^{th}$ mode shape in state space
$v(t)$	Velocity history
$v_{ref}$	Reference r.m.s. velocity value
$v_w$	r.m.s. velocity value
$w$	Displacement in z-direction
$x_i$	Spatial coordinate
$\{y\}$	State variables
$\{\dot{y}\}$	Time derivative of state variables
$A$	Roughness constant
$[A]$	State space matrix
$A_r^*$	$r^{th}$ modal mass in state space
$[B]$	State space matrix
$[C]$	Damping matrix
$[C_B]$	Damping matrix for subsystem B
$E$	Young's modulus
$\{F\}$	Force vector
$\{F_r\}$	Force vector for $r^{th}$ mode
$\{F_i\}$	Components of force vector
$\{F_p\}$	Force vector in independent coordinates
$F_{rwc}$	Rail wheel contact force
$F_{rail}$	Force on rail node

$F_{wheel}$	Force on rail wheel node
$H(f)$	High pass filter transfer function
$[K]$	Stiffness matrix
$[K_A]$	Stiffness matrix for subsystem A
$[K_{ij}]$	Components of stiffness matrix
$[K_p]$	Stiffness matrix for independent coordinates
$KB_F$	Filtered weighted severity
$KB_{F,max}$	Maximum filtered weighted severity
$L_v$	Root-mean-square velocity level
$L_z$	Length of model in z-direction
$M$	Number of response nodes on ground surface
$[M]$	Mass matrix
$[M_A]$	Mass matrix for subsystem A
$[M_{ij}]$	Components of mass matrix
$[M_p]$	Mass matrix for independent coordinates
$N$	Number of response nodes on rail surface
$PPV$	Peak particle velocity
$\{Q\}$	Force vector in state space
$[S]$	Constraint matrix
$S(\phi)$	Power spectral density
$S_d$	Components of constraint matrix for dependent coordinates
$S_i$	Components of constraint matrix for independent coordinates
$[T]$	Transformation matrix
$V$	Number of wheels
$V_p$	P-wave speed
$V_R$	Rayleigh wave speed
$V_S$	S-wave speed
$VdB$	Root-mean-square velocity level
$VDV$	Vibration dose value
$W$	Weight

## **CHAPTER 1**

### **INTRODUCTION**

#### **1.1 Motivation**

Railway transportation is one of the most thrusting agents of the modern civilization. High speed train systems have been developed for transportation between cities in several countries. Underground metro systems have been a remedy for the public transportation difficulties of modern cities. Ground borne vibrations are generated due to traffic of railway vehicles. These vibrations may pose serious problems for buildings nearby the railway and cause annoyance on people, not to mention malfunctioning of precise instruments in those buildings. Such environmental vibrations occur due to interaction of wheels of the train in motion with the track.

The interaction between the wheel and the rail causes dynamic loading due to irregularities on the wheel and the rail. These time varying loadings produce vibrations that can propagate in the form of waves through the soil for surface railways and in the tunnel and the soil around the tunnel for underground railway systems.

The buildings nearby the railway and the people inside these buildings will be affected by the vibrations transmitted to the foundations of the buildings. The buildings and the people are exposed to vibrations in the frequency range of about 2 and 80 Hz and to the re-radiated noise in the range of about 30 and 200 Hz [1].

It is essential to reduce annoyance of people living in nearby buildings to the track; sources of environmental vibrations generated, as well as the transmission paths must be extensively studied and identified in the design stage of the railway construction project.

Vibration prediction models are proposed to be practical tools in design stage. Amplitudes of ground borne vibrations depend on system components such as railway vehicle, rail irregularity profile, track and ground. These components should be modeled in detail as much as possible and with restricted level of assumptions for each component. A vibration prediction model should calculate vibration levels in a feasible time, with a good accuracy; and this is directly related to the accuracy in the modeling of system components. Furthermore, calculation steps and outputs of the vibration prediction model must be compatible with corresponding standard or regulation that is valid in the project.

Several models have been proposed to predict the level of vibrations. These models have some restrictions, such as long computation times and assumptions made in modeling of soil dynamics.

## **1.2 Objectives and research contribution**

In this thesis, a prediction model based on impulse response function and modal analysis is proposed. The specific objectives of this thesis can be listed as:

- to develop a numerical model capable of predicting track and ground vibration levels due to railway traffic for the use in detailed vibration assessments
- to use impulse response functions in the calculation of railway vibrations considering the transient behavior

- to model the wave motion in ground layers by applying modal analysis on finite difference equations
- to use modal coupling technique to couple track and ground components and so on to perform a detailed parametric study
- to use numerical modeling techniques to investigate vibration isolation techniques

The fundamental contributions of this thesis are:

- finite difference modeling of the wave motion in soil layers
- application of modal coupling for the coupling between soil layers as well as between track and ground
- implementation of impulse response functions in railway vibration predictions

### **1.3 Scope of the thesis**

Review of railway induced ground borne vibration is given in Chapter 2. Vibration generation and propagation mechanisms, assessment criteria and prediction models are summarized.

Theoretical background of the vibration prediction model is given in Chapter 3. Impulse response function calculation from modal parameters is introduced. Modal coupling technique is formulated for coupling subsystems and for different types of boundary condition applications.

In Chapter 4, finite difference modeling of soil layers is introduced. Fourth-order finite difference equations are given for displacement and stress components in

soil layer. Modal analysis of free boundary soil layer is implemented from these equations.

Numerical modeling details of proposed prediction model are presented in Chapter 5. First, multibody modeling of railway vehicle and calculation of rail wheel contact force are introduced. Second, finite element model for track dynamics and finite difference model for soil layer are presented in detail. Impulse response calculation from modal parameters of the system is shown. Vibration response calculation procedure is introduced and computational details are given.

Proposed vibration prediction model is implemented to predict ground borne vibrations at two railway sites for which measurement results are available in literature. The model is validated by comparison of predicted and measurement results. Chapter 6 outlines the results of these implementations.

The influences of various vehicle, track and soil parameters are studied by parametric analyses presented in Chapter 7.

By performing simulations of the presented vibration prediction model, practical vibration mitigation applications are studied in Chapter 8.

Chapter 9 includes summary of the thesis, discussions on the results of the work, and recommendations for future work.

## **CHAPTER 2**

### **REVIEW OF RAILWAY INDUCED GROUND VIBRATIONS**

#### **2.1 Vibration generation**

As the railway vehicle travels along the rail, two different loadings are present in the contact surface between wheel and rail: quasi static and dynamic loadings. Quasi static loading is due to the motion of the vehicle. The magnitude of this loading is invariant in time; however the loading locations change as the train moves. The contribution of quasi static loading on ground vibration is observed only at very low frequencies [2].

The dynamic loading component of the rail wheel contact force is basically due to the irregularity of the surfaces of rail and wheels. Local discontinuities such as weld connections on rail may also lead to dynamic loading. The vibrations generated due to dynamics loadings are present at a wide range of frequencies.

As the loading at the contact surface occurs, vibration propagates through wheels to vibrate the vehicle. Vibrations on the railway car may lead to discomfort to passengers and solution to this comfort problem is possible with design considerations. Similarly, propagation through the track components and ground layers is present to vibrate the ground. In this thesis work, vibration generation in the track and ground is investigated.

## 2.2 Rail surface irregularity

Empirical formulations are proposed for the irregularity of the rail surface. The rail surface profile is given by a power spectral density formulation by Garg and Dukkipati [3]:

$$S(\phi) = \frac{A\phi_2^2(\phi^2 + \phi_1^2)}{\phi^4(\phi^2 + \phi_2^2)} \quad (1)$$

In this formulation,  $S(\phi)$  is the power spectral density,  $\phi$  is the spatial frequency,  $A$  is the roughness constant, and  $\phi_1$  and  $\phi_2$  are the break frequencies. The values for the roughness constant and the break frequencies are given for six different track classes [3].

## 2.3 Wave propagation through railway track

Ballasted track is the most common type of railway track. The basic components of typical ballasted track are rail, rail pad, sleeper and ballast. It is also possible to see additional support layers such as subballast and subgrade, as well as mitigation layers such as under sleeper pad or under ballast mat.

The main functions of ballast and subballast layers are to support the track, to maintain water drainage and to distribute track loads over ground surface [4]. Sleepers are placed on the ballast to distribute the wheel loads on ballast and to transmit lateral and longitudinal forces. Resilient fasteners and rail pads are placed on sleepers. Two rails with a standard gauge of 1.435 m are present to guide the railway vehicle.

## 2.4 Wave propagation in ground layers

The vibrations generated due to the contact forces travel through the track and in the ground, in the form of waves. The waves in the ground are commonly in three forms, compressional waves, shear waves and Rayleigh waves. For compressional waves (P-waves), the motion of the wave is in the direction of the propagation. P-waves are the fastest of the three common wave types. For shear waves (S-waves), the direction of the motion is the transverse direction of the propagation. P- and S-waves propagate primarily beneath the surface and they are called body waves. Rayleigh waves propagate at the surface of the ground and the motion is in both horizontal and vertical directions. Rayleigh waves are slower than P- and S-waves. The other possible, but less common, forms of wave motion in the ground are Lamb waves in soil layers and Stoneley waves at interfaces. As a harmonic normal load is applied on a half space, Rayleigh waves transmit approximately 67% of the excitation energy, while S-waves transmit 26% and P-waves transmit 7% [5].

In the modeling of wave motion in ground layers, generally four material properties are used. These parameters are Young's modulus, Poisson's ratio, density and damping ratio. The wave speeds for the P- and S-waves can be expressed as:

$$V_P = \sqrt{\frac{\lambda + 2\mu}{\rho}} \quad (2)$$

$$V_S = \sqrt{\frac{\mu}{\rho}} \quad (3)$$

Here,  $\lambda$  and  $\mu$  are Lamé constants, defined by the Young's modulus,  $E$ , Poisson's ratio,  $\nu$ , and density,  $\rho$ .

$$\lambda = \frac{\nu E}{(1 + \nu)(1 - 2\nu)} \quad (4)$$

$$\mu = \frac{E}{2(1 + \nu)} \quad (5)$$

Rayleigh wave speed is approximated by the following equation in terms of S-wave speed and Poisson's ratio [6]:

$$V_R = \left( \frac{0.87 + 1.12\nu}{1 + \nu} \right) V_S \quad (6)$$

## 2.5 Assessment of vibrations

A detailed review of existing standards and/or regulations for different countries is presented in [7]. The measurement and assessment procedure for environmental vibrations are given in detail. Vibration criteria are given for acceleration amplitudes in Austria, Italy, Spain and the UK, for velocity amplitudes in Germany, France, Switzerland and the USA, for either acceleration or velocity in Norway and Sweden. Basic descriptors of vibration exposition are given below [1], [7].

Vibration dose value (*VDV*) is defined to quantify the intermittent vibration, in British standard BS 6472. For a single event, the *VDV* is expressed by:

$$VDV = \left[ \int_0^T a^4(t) dt \right]^{0.25} \quad (7)$$

The unit for the *VDV* is  $m/s^{1.75}$ .  $a(t)$  is the frequency weighted acceleration as a function of time and the duration of the event is  $T$ . For possible multiple events, the total *VDV* is obtained by summation using a fourth power law:

$$VDV_T = [VDV_1^4 + VDV_2^4 + VDV_3^4 + \dots]^{0.25} \quad (8)$$

The calculated *VDV* can be compared with acceptable criteria given in the standard.

$KB$  value is defined to compute the vibration severity, in German standard DIN 4150. Running root-mean-square (*rms*) vibration velocity measurements are used in the calculations:

$$KB_F(t) = \sqrt{\frac{1}{\tau} \int_0^t KB^2(\xi) e^{-(t-\xi)/\tau} d\xi} \quad (9)$$

Here,  $\tau$  is the time constant for calculation of *rms* and it is set as  $\tau = 0.125$  s for fast *rms*.  $KB(t)$  is the weighted velocity signal obtained by filtering the original signal by a high pass filter with cut off frequency of  $f_0 = 5.6$  Hz:

$$H(f) = \frac{1}{\sqrt{1 + (f_0/f)^2}} \quad (10)$$

The calculated  $KB_F$  values are labeled as acceptable, or not acceptable, after comparing with the criteria considering the type of building, and the evaluation time, namely day- or night-time. Maximum value of  $KB_F$  values,  $KB_{F,max}$ , may also be used as a vibration level descriptor:

$$KB_{F,max} = \max(|KB_F(t)|) \quad (11)$$

Peak particle velocity (*PPV*) is the absolute maximum value of a velocity signal. *PPV* is used to compare the vibration level with the criteria for building damage, given in international standard ISO 4866.

$$PPV = \max(|v(t)|) \quad (12)$$

Maximum running root-mean-square velocity level ( $L_v$  or *VdB*) is defined as the ratio of maximum running r.m.s. value ( $v_w$ ) to a reference value ( $v_{ref}$ ):

$$L_v = VdB = 20 \log \frac{v_w}{v_{ref}} \quad (13)$$

It is also possible to calculate *VdB* values in one-third octave bands between 1 to 80 Hz ranges.

As there are vibration metrics given in both time and frequency domains, a vibration prediction model should present outputs in both these domains.

## **2.6 Prediction models**

### **2.6.1 Analytical prediction models**

A prediction method for ground vibration generated by surface railway traffic is developed by the Dynamics Group of the Institute of Sound and Vibration Research (ISVR), at University of Southampton [8]–[13]. Several studies have been performed over the years starting late 90's. Sheng et al. proposed a method to calculate the Fourier transformed dynamic flexibility matrices of layered ground [8]. The layered ground model is coupled with a railway track structure which is modeled as an infinite, layered beam structure. The responses at a large number of positions can be calculated with the method. The loading is either a fixed position harmonic load on the railway track structure or directly on the ground surface. The track structure is shown to be strongly effective on the directivity and amplitude of the responses of the ground structure.

Sheng et al. presented the complete ground vibration prediction model including the vertical dynamics of the railway vehicle [13]. The vertical rail irregularity is the input of the system. The model is used to calculate the dynamic force between the wheel and the rail, and the maximum displacement along the track centerline on the ground. Two different ballasted tracks and a slab track are used in the calculations. The results show that, for a large range of frequency, the layered structure of the ground and the vehicle speed do not have significant effect on the dynamic contact force and the displacements at the wheel rail contact points. On the other hand, wave propagation depends strongly on the motion of the vehicle and the track parameters. The prediction model is applied for the traffic of a passenger coach in Britain. It is shown that; only for frequencies much below the

cut on frequency of the track ground system, quasi-static loading is dominant in response. Dynamic loading component is found to be more important in the response, for lower vehicle speeds and also for more distance from the track.

Karlström and Boström presented an analytical approach modeling the ground as a layered half space [14]. In this approach, Euler-Bernoulli beam is used to model the rails and sleepers are modeled as anisotropic Kirchhoff plate. Fourier transform based solution is performed for the traffic of X2 train in Ledsgard, Sweden. The predictions are validated by measurements for train speeds of 70 km/h and 200 km/h.

### **2.6.2 Finite difference prediction models**

Katou et al. applied a three-dimensional viscoelastic finite difference method to analyze the ground vibration induced by a high speed train [15]. In their work, force histories acting on the track are recorded and a realistic source function is computed for analyses. The numerical modeling of the track, embankment and ground and the computation details are given in detail. About 32 million grid points are used in the staggered grid model. The results of the model are compared and found to be closely resembled with the measured vibration levels.

### **2.6.3 Three-dimensional boundary element prediction models**

Galvin and Dominguez presented a boundary element based time domain model for prediction of railway induced vibrations by high speed trains [16], [17]. The track components are modeled by boundary elements. The formulation of the boundary elements is given briefly. Material damping is introduced in time domain, by considering the damping ratio at the dominant vibration period. Prediction model is tested against an analytical solution of half space under constant speed point load. The vehicle parameters, the axle load distribution and the boundary element distribution are described. Predicted vibration levels are

compared and shown to be in good agreement with experimental records for time domain comparisons. There are differences in the frequency distribution, since the excitation is modeled only for axle loads. Effects of different ballast and embankment configurations are studied. An underpass structure is modeled and considered in the analyses.

#### **2.6.4 Three-dimensional finite element prediction models**

A three-dimensional two-step vibration prediction model is proposed by Kouroussis et al. [18]. They proposed an uncoupled approach such that in the first step, ground forces are obtained from the vehicle-track system. A home-made C++ library is used at this level. Then, in the second step, these ground forces are applied to the soil model and the ground response is calculated. The soil model is developed as a half-sphere domain using a commercial finite element code, ABAQUS. The transition domain between finite and infinite elements is meshed to optimize the boundary performance. The infinite elements are modeled using the formulation given in [19]. The finite element performance considering the domain size and the maximum element size is studied. The roughness of the rail-wheel contact is introduced implementing a power spectrum density based model by [3]. The wheel-rail contact force is modeled by a nonlinear Hertzian spring. Modeling of different elements in the two-step formulation and conditions for which a ballast soil decoupling is valid are shown in [20].

Kouroussis et al. presented the simulations for prediction of vibrations from a tramway, T2000 LRV in Brussels, due to a discontinuity at the wheel-rail contact surface [18]. Prediction results for the response of the tramway vibrations, as well as the ground vibrations are shown to be in good agreement with measured data. The time domain solution is expressed to be appropriate to model transient dynamic loading. In studies [21], [22], the main contribution was the relatively detailed modeling of the vehicle. Effects of roughness and local discontinuities on vibrations are assessed. A resilient element is applied between the rolling tread

and the hub of the vehicle, and the effect of this mitigation on ground vibration is shown. Modal decomposition of the vehicle is studied to investigate the modal contributions on the wheel rail contact force in [23]. It is observed that the bogie pitch mode influences the ground vibration mainly.

Vibration response of a building near the tram line is calculated [24], [25]. The tram is T2000 LRV of Brussels. Calculation time examples are presented, a total of two day duration is stated. Soil is modeled as six layers, with 527,000 degrees of freedom. Layered prediction model predicts better than the homogeneous model. Modeling details of the building near tram are also given. The free field vibration response is compared for the cases with and without the building. When the vehicle passes the defect on the rail, the vibration amplitude is significant in both cases. When the vehicle passes close to the building, the ground wave distribution and extrema amplitudes are observed to be different in two cases. When the building is present, the surface vibration is amplified in the front side and attenuated in the back side of the building highlighting a barrier effect for vibrational waves.

Vibration measurements are presented for a high speed train running at Mévergnies (Belgium) between Brussels and Paris/London [26]. Measurement results are compared by predictions of the two-step compound model developed. The measurements are performed for the free field vibrations due to the traffic of two types of high speed train, Thalys and Eurostar, at various speeds. The significance of detailed vehicle modeling and soil layering are shown with several case studies. Kouroussis et al also presented the measurements of ground vibration due to traffic of InterCity and InterRegion trains in the study [27]. Measurements are performed on various sites in Belgium, on different track and soil configurations.

A coupled lumped mass model is proposed for the vertical coupling of railway track through the soil [28]. A mass-spring-damper system is presented between the foundations, in order to represent the contact area between the track and soil. Soil stiffness and soil layering are analyzed by numerical examples on high speed line at Mévergnies and Haren. Proposed method is shown to be more reliable than simple model to predict vibration level and reaction forces, by performing dynamic analyses of a track on various foundations.

Two-step prediction model is used to analyze different parameters in vehicle, track and ground system. Contribution of the pitch motion of the bogies and car bodies is presented in [29]. Minimal coordinates approach is implemented in vehicle dynamic modeling and it is concluded that light changes are present in ground vibration response when the pitch motion is considered.

The effect of soil parameters on ground vibration is studied in [30]. Homogeneous soil formation and two-layer ground formation are analyzed. For two-layer ground, a specific distance is observed, where the slope in amplitude versus distance plot changes. A sensitivity analysis is presented for variation in soil parameters and distance from the track.

The influence of the interaction between soil and structures on the ground vibration is presented in [31]. For T2000 tram, it is observed that for speeds higher than 20 km/h, the main contribution of generated noise is the rolling noise. Important levels of ground vibration are observed when rail joints or turnouts are present. A building model is inserted into the finite element for the ground dynamics and ground vibration levels are shown to be influenced by the presence of a building near the track.

Kouroussis et al. proposed a train speed calculation technique by using ground vibration information [32]. Conventional train speed calculation methods are

reviewed in detail. These methods are introduced with the practical considerations. By applying the two-step prediction model, numerical validation of the proposed method is presented. The method is proven on different track configurations for tram, intercity train and high speed train traffic, for different speeds.

Connolly et al. presented a three-dimensional numerical model to predict railway traffic induced ground vibrations [33]. Finite element modeling is used to simulate vibrations in time domain by considering the nonlinear excitation mechanisms. ABAQUS is used as finite element software. Absorbing boundary is applied for the truncation of the finite element boundary and in order to increase the absorption performance, the soil is modeled in a spherical geometry. The track components are modeled in detail. The multibody approach is used to include vehicle dynamics. FORTRAN subroutines are applied and developed to simulate the loadings on the rail and the vehicle. It is noted that in the typical ABAQUS subroutines, it is not directly possible to implement a displacement loading.

The influence of the embankment constituent material on vibration levels is analyzed by model proposed [33]. The proposed model is verified by comparing the results with the measurements on a high speed line [26]. The frequency content comparison is presented up to 60 Hz in narrow band. Ground vibration levels are predicted to be higher when a softer embankment material is applied.

An initial assessment ground vibration prediction model is presented by Connolly et al [34]. The soil dynamics is included in the model called ScopeRail, unlike the previous scoping models. The other advantage of the model is the zero run time that allows for rapid prediction. The modeling procedure and the machine learning details are given. The input parameters for the neural network are the train speed, Young's modulus, depth and damping ratio for the first layer, Young's modulus for the half space and the distance. Outputs are two vibration descriptors,

maximum weighted severity,  $KB_{F,max}$ , and peak particle velocity,  $PPV$ . A total 360 permutations of input parameters are computed for neural network. Simulation time for three seconds of modeling time is expressed as 50 hours. Sensitivity analysis is performed for soil parameters and train type. The soil is modeled as a two layer ground. In order to represent layered ground, a soil layer mapping is defined. The model accurately predicted vibration levels on four different high speed lines. The model decreases the cost of railway projects by reducing the computation requirements.

### **2.6.5 Prediction models for underground railway traffic**

The pipe-in-pipe model was developed to predict the ground borne vibration due to underground railway traffic, using analytical three-dimensional models [35]–[39]. In this model, the tunnel and the soil surrounding the tunnel are modeled as two concentric pipes. The continuum theory of elasticity in cylindrical coordinates is used to model the motion of the tunnel and the soil. The tunnel-soil interface is modeled with the equilibrium of stresses and the compatibility of the displacements. The tunnel is assumed to be invariant in the longitudinal direction. The motion of the tunnel and the soil are formulated in the frequency-wavenumber domain. Euler-Bernoulli beam theory is used to model the track and the track is coupled to model considering the structure. The railway vehicle is modeled as lumped masses. The excitation is due to the irregularity of the wheel and rail surfaces. Random process theory is applied to model the excitation. The results of the model give the displacements of the points on the tunnel and in the soil surrounding the tunnel. Later, the model is developed to predict the ground vibrations on the free surface over the underground railway.

The coupled periodic finite element-boundary element model is another formulation to model the ground borne vibration due to underground railway traffic [40], [41]. Soil is modeled by using a boundary element method and the tunnel is modeled with finite elements. The track is integrated to the tunnel

structure with the Craig-Bampton substructuring technique. The periodicity of the tunnel is used with the Floquet transformation to formulate the coupled problem and to compute the wave field radiated into the soil.

Gupta et al. compared the pipe-in-pipe model with the couple finite element-boundary element model [42]. The advantages and disadvantages of the two models are compared. They concluded that the pipe-in-pipe model is an analytical formulation and therefore it has computational efficiency. The disadvantages of the pipe-in-pipe model are given as it can work with only simple geometry for the tunnel and the presence of layering in the soil cannot be considered in this model. The coupled periodic FE-BE method has the advantages of full modeling of tunnels with complex geometry and modeling the layered soil impedance using the boundary elements. This model may be inefficient for large mesh sizes. The results of the case studies show that the two models have agreement for response predictions.

## **2.7 Vibration measurements**

Along with numerical studies, there are some experimental works published on ground vibration due to railway traffic. These publications are covered in this section.

Generally, soil wave speeds are also recorded in the studies with experimental measurements. Spectral analysis surface waves (SASW) testing procedure is commonly used to obtain wave speeds.

A detailed summary of railway vibration measurements in Europe is presented by Connolly et al. [43]. In this paper, the results of measured data at 17 different sites

are analyzed for distance effect, attenuation relations, speed effects, train type, critical velocity effects and discrepancy considerations.

## **2.8 Effects of track and ground parameters on vibration**

Effects of typical railway vehicle and track parameters on the ground vibrations are analyzed by Kouroussis et al. [44]. Two-step vibration prediction model is used in the analyses. The vehicle parameters considered are its type and its speed. The track parameters considered are rail type, rail pad stiffness, sleeper mass, sleeper spacing and ballast stiffness. For all the parameters, the range is defined from the values available in the literature. Three indicators are presented: ground acceleration, rail velocity and soil velocity. The influences of the vehicle and track parameters on these indicators are presented in detail. A high increase in the soil vibrations velocity is observed either of the following parameters is increased: axle load, vehicle speed, rail stiffness, rail pad stiffness and ballast stiffness. Increase in sleeper spacing leads to a light increase in soil velocity. The changes in rail mass and sleeper mass do not influence the soil velocity. It is concluded that rail type, rail pad, ballast and sleepers have a limited practical range of values, and the primary parameter to control the ground vibration is the track flexibility.

Kouroussis et al. presented a detailed review of the influence of vehicle characteristics on the ground and track vibrations [45]. The effect of different vehicle configurations on the vibration generation is studied. Vehicle dynamics are found to contribute to the ground vibration for low frequency range. For high speed trains, quasi-static excitation is the main reason for ground vibration due to very high quality of rolling surfaces. For light rail vehicles, singular rail surface defects, like rail joints, rail crossings or switching gears are the reasons for dynamic excitation. For intercity traffic, the speed is in a range between light rail traffic and high speed trains and both quasi-static excitation and singular defects are possible to exist. When the train speed exceeds half of the Rayleigh wave speed, vibrations levels start to increase promptly. Numerical prediction models

are briefly given and they are compared extensively for the suitability to include vehicle effects. The critical speed is defined for track and soil dynamics. Rail unevenness spectra available in the literature are given. A vehicle parameter database is presented. Vehicles from different speed ranges are listed by showing geometrical and dynamical parameters in detail. The research references are also given where each vehicle is presented in the analysis and measurements.

## **2.9 Vibration mitigation techniques**

Connolly et al. analyzed the influence of the wave barriers to mitigate the ground vibration [46]. The proposed numerical model is expressed to be validated by vibration measurements recorded near a high speed line outside Edinburgh. Validation is presented by simple time history comparison of velocity levels. In soil modeling, a cuboid geometry is preferred to insert the trench more easily. Several wave barrier configurations are compared for their effect on the ground vibration levels. The depth and the length of the wave barrier influence the vibration amplitude, however the width does not. For a specific example, a wave barrier configuration is recommended with large amount of cost saving. A practical observation is made that the ratio of the acoustical impedance of soil compared to wave barrier backfill material must be greater than eight.

## **2.10 Conclusion**

It can be concluded that railway traffic induced ground vibration is a complicated research field with vehicle dynamics, contact modeling, track dynamics and soil dynamics. The studies reviewed in the literature focus on different aspects such as modeling of vibration generation and propagation, measurement records, prediction of vibration levels and possible mitigation solutions.

Three-dimensional prediction models are recently introduced and they are shown to be successful, as they present the phenomena in much detail. These models have some drawbacks such as long computation times and modeling of system elements.

A practical vibration prediction model should give outputs in time and frequency domains as vibration metrics are defined in both of these domains.

## CHAPTER 3

### THEORETICAL BACKGROUND

This chapter presents the mathematical background that is utilized to calculate the response of dynamic systems to arbitrary loadings. In the calculations, modal parameters of a dynamic system are used to obtain unit impulse response functions. Convolution of these unit impulse response functions with the arbitrary loadings results in the response of the system.

First, unit impulse response functions are derived for an undamped system. Then, modal parameters of damped systems are shown to be obtained by undamped modal parameters and the damping coefficient. Damping model used in calculations is proportional viscous damping model.

It is quite possible that any system under consideration is composed of several subsystems. Modal coupling procedure is employed to unify these subsystems. The application of modal coupling for implementing fixed boundary condition and local viscous boundary condition is also formulated.

#### **3.1 Response to arbitrary excitation by convolution**

Unit impulse response function is defined as the response at a spatial coordinate in time domain for a unit impulsive loading applied at another or the same position. This function can be used to obtain the response to an arbitrary loading. In linear systems, convolution between the unit impulse response function and the excitation history gives the dynamic response as follows:

$$u(t) = \int_0^t f(t - \tau)h(\tau)d\tau \quad (14)$$

Here,  $f(t)$  is the forcing function and  $h(t)$  is the unit impulse response function. The MATLAB function  $conv(f, h)$  can be employed to calculate the convolution between the input parameters,  $f$  and  $h$ .

In the succeeding sections of this chapter, modal domain based formulations are presented to obtain the unit impulse response functions.

### 3.2 Modal parameters for an undamped system

Equation of motion for an undamped system can be written in spatial coordinates referred generalized coordinates as:

$$[M]\{\ddot{u}\} + [K]\{u\} = \{F\} \quad (15)$$

Modal parameters for this system can be obtained by solving this equation for free vibrations.

$$[M]\{\ddot{u}\} + [K]\{u\} = \{0\} \quad (16)$$

Assuming a harmonic response, the acceleration term can be written as:

$$\{\ddot{u}\} = -\omega^2\{u\} \quad (17)$$

$$-\omega^2[M]\{u\} + [K]\{u\} = \{0\} \quad (18)$$

$$[[K] - \omega^2[M]]\{u\} = \{0\} \quad (19)$$

$$[[K] - \lambda[M]]\{u\} = \{0\} \quad (20)$$

Equation (20) is the eigenvalue equation and the solution of this equation gives modes of vibration. The eigenvalues,  $\lambda_r = \omega_r^2$ , are the squares of the frequencies,

$\omega_r$ , of the vibration modes. The eigenvectors,  $u_r$ , are the mode shapes for the corresponding modes. The modal matrix  $[\phi]$  has the normalized eigenvectors,  $\{\phi_r\}$ , in its columns. The normalization is generally performed with respect to the mass matrix as:

$$\{u_r\}^T [M] \{u_r\} = m_r \quad (21)$$

$$\{\phi_r\} = \frac{1}{\sqrt{m_r}} \{u_r\} \quad (22)$$

$$\{\phi_r\}^T [M] \{\phi_r\} = 1 \quad (23)$$

It should be noted that the normalized mode shapes satisfy the following relationship:

$$\{\phi_r\}^T [K] \{\phi_r\} = \omega_r^2 \quad (24)$$

### 3.3 Unit impulse response function for an undamped system

As already described, unit impulse response function is the response at a spatial coordinate in time domain for a unit impulsive loading applied at another or the same position. Let  $h_{ij}(t)$  denote the unit impulse response function between two spatial coordinates  $x_i$  and  $x_j$ . Unit impulse response function can be obtained using modal parameters. The procedure to obtain this function is given below.

Equation of motion in the modal coordinates can be written as:

$$\{\ddot{\eta}\} + [\cdot \omega_r^2 \cdot] \{\eta\} = [\phi]^T \{F\} \quad (25)$$

For the  $r^{th}$  mode:

$$\ddot{\eta}_r + \omega_r^2 \eta_r = F_r \quad (26)$$

$$F_r = \{\phi_r\}^T \{F\} \quad (27)$$

The solution of this equation can be expressed as:

$$\eta_r(t) = \begin{cases} \int_0^t (t - \tau) F_r(\tau) d\tau & \omega_r = 0 \\ \frac{1}{\omega_r} \int_0^t F_r(\tau) \sin \omega_r (t - \tau) d\tau & \omega_r \neq 0 \end{cases} \quad (28)$$

The solution in spatial coordinates can be obtained using the transformation:

$$u(t) = [\phi] \eta(t) \quad (29)$$

For an impulsive loading application at spatial coordinate  $x_j$ :

$$F_r(t) = \phi_{r,j} F(t) \quad (30)$$

where

$$F(t) = \int_0^t \delta(\tau) d\tau \quad (31)$$

$$\eta_r(t) = \begin{cases} \phi_{r,j} \cdot t & \omega_r = 0 \\ \phi_{r,j} \frac{\sin \omega_r t}{\omega_r} & \omega_r \neq 0 \end{cases} \quad (32)$$

The impulse response function is written as:

$$h_{ij}(t) = \sum_{r=1}^{rb} \phi_{r,i} \phi_{r,j} \cdot t + \sum_{r=rb+1}^n \phi_{r,i} \phi_{r,j} \frac{\sin \omega_r t}{\omega_r} \quad (33)$$

The index for the summation covers the modes considered in the response and in the excitation. Number of rigid modes is shown by  $rb$ . For a linear system, this function has a reciprocity relation, meaning it gives the response at  $x_i$  due to a loading at  $x_j$ , or the response at  $x_j$  due to a loading at  $x_i$ .

$$h_{ij}(t) = h_{ji}(t) \quad (34)$$

It should be noted that, the unit impulse response function can be written between different degrees of freedom for a three-dimensional system. For instance,  $h_{ij}(t)$  can represent the displacement response in  $z$  direction at  $x_i$ ,  $w(x_i)$ , due to unit load in  $y$  direction at  $x_j$ ,  $f_y(x_j)$ . In Equation (33), corresponding elements of modal matrix,  $[\phi]$ , should be used.

### 3.4 Modal parameters for a damped system

Equation of motion for a system with viscous damping can be written as:

$$[M]\{\ddot{u}\} + [C]\{\dot{u}\} + [K]\{u\} = \{F\} \quad (35)$$

State space approach will be used to solve this equation. State variables are designated as velocity,  $\dot{u}$ , and displacement,  $u$ . In order to set up the state space equations, one can write a trivial equation as:

$$[M]\{\dot{u}\} - [M]\{\dot{u}\} = \{0\} \quad (36)$$

Then, these equations can be expressed as:

$$\begin{bmatrix} [0] & [M] \\ [M] & [C] \end{bmatrix} \begin{Bmatrix} \{\dot{u}\} \\ \{u\} \end{Bmatrix} + \begin{bmatrix} -[M] & [0] \\ [0] & [K] \end{bmatrix} \begin{Bmatrix} \{\dot{u}\} \\ \{u\} \end{Bmatrix} = \begin{Bmatrix} \{0\} \\ \{F\} \end{Bmatrix} \quad (37)$$

$$[A]\{y\} + [B]\{y\} = \{Q\} \quad (38)$$

Here  $[M]$ ,  $[C]$  and  $[K]$  are  $n \times n$  matrices,  $\{q\}$  and  $\{F\}$  are  $n \times 1$  vectors. Similarly,  $[A]$  and  $[B]$  are  $2n \times 2n$  matrices,  $\{y\}$  and  $\{Q\}$  are  $2n \times 1$  vectors.

Free vibrations will give the modal parameters. For free vibrations:  $\{F\} = \{0\}$ , then  $\{Q\} = \{0\}$ .

$$[A]\{\dot{y}\} + [B]\{y\} = \{0\} \quad (39)$$

Assuming harmonic motion,

$$\{y\} = \{\psi^*\}e^{\lambda^*t} \quad (40)$$

$$\{\dot{y}\} = \lambda^*\{\psi^*\}e^{\lambda^*t} \quad (41)$$

The state space equations can now be written as:

$$\lambda^*[A]\{\psi^*\}e^{\lambda^*t} + [B]\{\psi^*\}e^{\lambda^*t} = \{0\} \quad (42)$$

$$\lambda^*[A]\{\psi^*\} + [B]\{\psi^*\} = \{0\} \quad (43)$$

$$[B]\{\psi^*\} = -\lambda^*[A]\{\psi^*\} \quad (44)$$

Equation (44) is the eigenvalue problem with eigenvalues  $\lambda_r^*$  and corresponding eigenvectors  $\{\psi_r^*\}$  for  $r = 1, 2, \dots, 2n$ . Eigenvalues  $\lambda_r^*$  are found from:

$$|[B] + \lambda^*[A]| = 0 \quad (45)$$

The eigenvalues appear as complex conjugate pairs  $\lambda_r^*$  and  $\bar{\lambda}_r^*$  for  $r = 1, 2, \dots, n$ .

$$\lambda_r^* = -\zeta_r\omega_r + i\omega_{rd} \quad (46)$$

$$\bar{\lambda}_r^* = -\zeta_r\omega_r - i\omega_{rd} \quad (47)$$

$$\omega_{rd} = \omega_r\sqrt{1 - \zeta_r^2} \quad (48)$$

Similarly, the corresponding eigenvectors are also complex conjugates for  $\{\psi_r^*\}$  and  $\{\bar{\psi}_r^*\}$  for  $r = 1, 2, \dots, n$ . Following the definition of the state space formulation,

the ratio of the first half of eigenvectors to the second half is equal to the corresponding eigenvalue.

$$\{\psi_r^*\} = \begin{Bmatrix} \{v_r^*\} \\ \{u_r^*\} \end{Bmatrix} \quad (49)$$

$$\{v_r^*\} = \lambda_r^* \{u_r^*\} \quad (50)$$

The modal matrix  $[\phi^*]$  is formed by the normalized eigenvectors  $\{\phi_r^*\}$  and its size is  $2n \times 2n$ .

$$A_r^* = \{\psi_r^*\}^T [A] \{\psi_r^*\} \quad (51)$$

$$\{\phi_r^*\} = \frac{1}{\sqrt{A_r^*}} \{\psi_r^*\} \quad (52)$$

The modal matrix can be normalized to obtain the matrix  $[A^*]$  as an identity matrix of size  $2n \times 2n$ .

$$[\phi^*]^T [A] [\phi^*] = [I] \quad (53)$$

It should be noted that the normalized mode shapes satisfy the following relationship:

$$\{\phi_r^*\}^T [B] \{\phi_r^*\} = -\lambda_r^* \quad (54)$$

### 3.5 Damped modes from undamped modes and damping properties

For proportional viscous damping model, modal parameters for the damped systems can be obtained from undamped modal parameters and damping ratio of the material.

As shown preceding section, it is practical to use the state space approach for a damped system when the damping matrix is nonzero. One can set up the state space formulation for an undamped system as well. The state space formulation of an undamped system can be later modified to insert the effect of damping.

It should be noted that the size of the eigenvalue problem of damped system is twice that of undamped system. Eigenvalue analyses require long computational times for large systems. For damped system, as matrix sizes are doubled, this time requirement will increase. Therefore, it is computationally practical to calculate modal parameters for undamped system and then modify these parameters for damping ratio.

### 3.5.1 State space formulation for an undamped system

For free vibrations of an undamped system:

$$\begin{bmatrix} [0] & [M] \\ [M] & [0] \end{bmatrix} \begin{Bmatrix} \{\ddot{u}\} \\ \{\dot{u}\} \end{Bmatrix} + \begin{bmatrix} -[M] & [0] \\ [0] & [K] \end{bmatrix} \begin{Bmatrix} \{\dot{u}\} \\ \{u\} \end{Bmatrix} = \begin{Bmatrix} \{0\} \\ \{0\} \end{Bmatrix} \quad (55)$$

$$\begin{bmatrix} [0] & [M] \\ [M] & [0] \end{bmatrix} \{y\} + \begin{bmatrix} -[M] & [0] \\ [0] & [K] \end{bmatrix} \{y\} = \{0\} \quad (56)$$

$$\left[ \lambda \begin{bmatrix} [0] & [M] \\ [M] & [0] \end{bmatrix} + \begin{bmatrix} -[M] & [0] \\ [0] & [K] \end{bmatrix} \right] \{y\} = \{0\} \quad (57)$$

$$\left| \lambda \begin{bmatrix} [0] & [M] \\ [M] & [0] \end{bmatrix} + \begin{bmatrix} -[M] & [0] \\ [0] & [K] \end{bmatrix} \right| = 0 \quad (58)$$

$$\begin{vmatrix} -[M] & \lambda[M] \\ \lambda[M] & [K] \end{vmatrix} = 0 \quad (59)$$

Since  $[M]$  is positive definite and invertible,

$$|-[M]| |[K] - \lambda[M](-[M])^{-1}\lambda[M]| = 0 \quad (60)$$

$$|-[M]| |[K] + \lambda^2 [M][M]^{-1}[M]| = 0 \quad (61)$$

Since  $|-[M]| \neq 0$ ,

$$|[K] + \lambda^2 [M]| = 0 \quad (62)$$

The solution to this equation gives the eigenvalues:

$$\lambda_r^* = i\omega_r \quad (63)$$

$$\overline{\lambda_r^*} = -i\omega_r \quad (64)$$

The eigenvalues are complex conjugates with zero real part, the imaginary part being the natural frequencies,  $\omega_r$ , already obtained above.

In order to determine the eigenvector corresponding to the eigenvalue,  $\lambda_r^* = i\omega_r$ , one can assume a solution using the definition of the state space formulation:

$$\{\psi_r^*\} = \begin{Bmatrix} \lambda_r^* \{u_r^*\} \\ \{u_r^*\} \end{Bmatrix} \quad (65)$$

Normalization of this eigenvector by the matrix  $[A]$  in the state space equation of motion:

$$\begin{Bmatrix} \lambda_r^* \{u_r^*\} \\ \{u_r^*\} \end{Bmatrix}^T \begin{bmatrix} [0] & [M] \\ [M] & [0] \end{bmatrix} \begin{Bmatrix} \lambda_r^* \{u_r^*\} \\ \{u_r^*\} \end{Bmatrix} = 1 \quad (66)$$

$$\begin{Bmatrix} \lambda_r^* \{u_r^*\} \\ \{u_r^*\} \end{Bmatrix}^T \begin{Bmatrix} [M] \{u_r^*\} \\ [M] \lambda_r^* \{u_r^*\} \end{Bmatrix} = 1 \quad (67)$$

$$\lambda_r^* \{u_r^*\}^T [M] \{u_r^*\} + \{u_r^*\}^T [M] \lambda_r^* \{u_r^*\} = 1 \quad (68)$$

$$2\lambda_r^* \{u_r^*\}^T [M] \{u_r^*\} = 1 \quad (69)$$

Comparing with the undamped formulation:

$$\{\phi_r\}^T [M] \{\phi_r\} = 1 \quad (70)$$

The displacement part of the eigenvector,  $\{u_r^*\}$ , can be obtained from the undamped eigenvector,  $\{\phi_r\}$ , as:

$$\{u_r^*\} = \frac{1}{\sqrt{2\lambda_r^*}} \{\phi_r\} \quad (71)$$

The complete normalized eigenvector for  $\lambda_r^* = i\omega_r$  is:

$$\{\phi_r^*\} = \left\{ \begin{array}{l} \frac{\lambda_r^*}{\sqrt{2\lambda_r^*}} \{\phi_r\} \\ \frac{1}{\sqrt{2\lambda_r^*}} \{\phi_r\} \end{array} \right\} \quad (72)$$

The complete normalized eigenvector for  $\bar{\lambda}_r^* = -i\omega_r$  is:

$$\{\bar{\phi}_r^*\} = \left\{ \begin{array}{l} \frac{\bar{\lambda}_r^*}{\sqrt{2\bar{\lambda}_r^*}} \{\phi_r\} \\ \frac{1}{\sqrt{2\bar{\lambda}_r^*}} \{\phi_r\} \end{array} \right\} \quad (73)$$

which is actually the complex conjugate of  $\{\phi_r^*\}$ .

### 3.5.2 Modal parameters for proportional viscously damped system

For proportional viscous damping, the damping matrix is proportional to the mass and stiffness matrices as:

$$[C] = \alpha[M] + \beta[K] \quad (74)$$

These types of proportional damping are generally called as alpha and beta damping. Beta damping is more commonly applied, and the following formulation will be shown for beta damping.

For free vibrations of a proportional beta damped system:

$$\begin{bmatrix} [0] & [M] \\ [M] & \beta[K] \end{bmatrix} \begin{Bmatrix} \{\ddot{u}\} \\ \{\dot{u}\} \end{Bmatrix} + \begin{bmatrix} -[M] & [0] \\ [0] & [K] \end{bmatrix} \begin{Bmatrix} \{u\} \\ \{u\} \end{Bmatrix} = \begin{Bmatrix} \{0\} \\ \{0\} \end{Bmatrix} \quad (75)$$

$$\left[ \lambda \begin{bmatrix} [0] & [M] \\ [M] & \beta[K] \end{bmatrix} + \begin{bmatrix} -[M] & [0] \\ [0] & [K] \end{bmatrix} \right] \{y\} = \{0\} \quad (76)$$

$$\left| \lambda \begin{bmatrix} [0] & [M] \\ [M] & \beta[K] \end{bmatrix} + \begin{bmatrix} -[M] & [0] \\ [0] & [K] \end{bmatrix} \right| = 0 \quad (77)$$

$$\begin{vmatrix} -[M] & \lambda[M] \\ \lambda[M] & (\lambda\beta + 1)[K] \end{vmatrix} = 0 \quad (78)$$

Since  $[M]$  is positive definite and invertible,

$$|-[M]| |(\lambda\beta + 1)[K] - \lambda[M](-[M])^{-1}\lambda[M]| = 0 \quad (79)$$

$$|-[M]| |(\lambda\beta + 1)[K] + \lambda^2[M][M]^{-1}[M]| = 0 \quad (80)$$

Since  $|-[M]| \neq 0$ ,

$$|(\lambda\beta + 1)[K] + \lambda^2[M]| = 0 \quad (81)$$

$$\lambda^2 + \omega_r^2(\lambda\beta + 1) = 0 \quad (82)$$

$$\lambda^2 + \beta\omega_r^2\lambda + \omega_r^2 = 0 \quad (83)$$

$$\lambda = -\frac{\beta\omega_r^2}{2} \pm \frac{\sqrt{\beta^2\omega_r^4 - 4\omega_r^2}}{2} \quad (84)$$

Let  $\zeta_r = \frac{\beta\omega_r}{2}$ ,

$$\lambda = -\zeta_r\omega_r \pm \frac{\sqrt{4\zeta_r^2\omega_r^2 - 4\omega_r^2}}{2} \quad (85)$$

$$\lambda = -\zeta_r\omega_r \pm \frac{2\omega_r\sqrt{\zeta_r^2 - 1}}{2} \quad (86)$$

$$\lambda = -\zeta_r\omega_r \pm i\omega_r\sqrt{1 - \zeta_r^2} \quad (87)$$

One can express the complex conjugate eigenvalues, in terms of the undamped natural frequencies,  $\omega_r$ , and the damping ratio,  $\zeta_r = \frac{\beta\omega_r}{2}$ , as:

$$\lambda_r^* = -\zeta_r\omega_r + i\omega_{r,d} \quad (88)$$

$$\bar{\lambda}_r^* = -\zeta_r\omega_r - i\omega_{r,d} \quad (89)$$

$$\omega_{r,d} = \omega_r\sqrt{1 - \zeta_r^2} \quad (90)$$

In order to obtain the eigenvector corresponding to the eigenvalue,  $\lambda_r^* = -\zeta_r\omega_r + i\omega_{r,d}$ , one can assume a solution using the definition of the state space formulation:

$$\{\psi_r^*\} = \begin{Bmatrix} \lambda_r^*\{u_r^*\} \\ \{u_r^*\} \end{Bmatrix} \quad (91)$$

Normalization of this eigenvector by the matrix  $[A]$  in the state space equation of motion:

$$\begin{Bmatrix} \lambda_r^* \{u_r^*\} \\ \{u_r^*\} \end{Bmatrix}^T \begin{bmatrix} [0] & [M] \\ [M] & \beta[K] \end{bmatrix} \begin{Bmatrix} \lambda_r^* \{u_r^*\} \\ \{u_r^*\} \end{Bmatrix} = 1 \quad (92)$$

$$\begin{Bmatrix} \lambda_r^* \{u_r^*\} \\ \{u_r^*\} \end{Bmatrix}^T \begin{Bmatrix} [M] \{u_r^*\} \\ ([M] \lambda_r^* + \beta[K]) \{u_r^*\} \end{Bmatrix} = 1 \quad (93)$$

$$\lambda_r^* \{u_r^*\}^T [M] \{u_r^*\} + \{u_r^*\}^T ([M] \lambda_r^* + \beta[K]) \{u_r^*\} = 1 \quad (94)$$

$$2\lambda_r^* \{u_r^*\}^T [M] \{u_r^*\} + \beta \{u_r^*\}^T [K] \{u_r^*\} = 1 \quad (95)$$

Comparing with the undamped formulation:

$$\{\phi_r\}^T [M] \{\phi_r\} = 1 \quad (96)$$

$$\{\phi_r\}^T [K] \{\phi_r\} = \omega_r^2 \quad (97)$$

The displacement part of the eigenvector,  $\{u_r^*\}$ , can be obtained from the undamped eigenvector,  $\{\phi_r\}$ , as:

$$\{u_r^*\} = \frac{1}{\sqrt{2\lambda_r^* + \beta\omega_r^2}} \{\phi_r\} \quad (98)$$

Note that from Equation (88), the real part of the eigenvalue is:

$$Real(\lambda_r^*) = -\frac{\beta\omega_r^2}{2} \quad (99)$$

Then, Equation (98) can be rewritten as:

$$\{u_r^*\} = \frac{1}{\sqrt{2i \cdot Imag(\lambda_r^*)}} \{\phi_r\} \quad (100)$$

The complete normalized eigenvector for  $\lambda_r^*$  is:

$$\{\phi_r^*\} = \begin{Bmatrix} \frac{\lambda_r^*}{\sqrt{2i \cdot \text{Imag}(\lambda_r^*)}} \{\phi_r\} \\ 1 \\ \frac{1}{\sqrt{2i \cdot \text{Imag}(\lambda_r^*)}} \{\phi_r\} \end{Bmatrix} \quad (101)$$

The complete normalized eigenvector for  $\bar{\lambda}_r^* = -i\omega_r$  is:

$$\{\bar{\phi}_r^*\} = \begin{Bmatrix} \frac{\bar{\lambda}_r^*}{\sqrt{2i \cdot \text{Imag}(\bar{\lambda}_r^*)}} \{\phi_r\} \\ 1 \\ \frac{1}{\sqrt{2i \cdot \text{Imag}(\bar{\lambda}_r^*)}} \{\phi_r\} \end{Bmatrix} \quad (102)$$

which is actually the complex conjugate of  $\{\phi_r^*\}$ .

### 3.6 Unit impulse response function for a damped system

Equation of motion in the modal coordinates can be written as:

$$\{\dot{\eta}\} - [\cdot \lambda^* \cdot] \{\eta\} = [\phi^*]^T \{F\} \quad (103)$$

For  $r^{th}$  mode:

$$\dot{\eta}_r - \lambda_r^* \eta_r = F_r \quad (104)$$

$$F_r = \{\phi_r^*\}^T \{F\} \quad (105)$$

The solution for this equation is:

$$\eta_r(t) = \int_0^t F_r(\tau) e^{\lambda_r^*(t-\tau)} d\tau \quad (106)$$

The solution in spatial coordinates can be obtained using the transformation:

$$u(t) = [\phi^*]\eta(t) \quad (107)$$

For an impulsive loading application at  $x_j$ :

$$F_r(t) = \phi_{r,j}^* F(t) \quad (108)$$

$$F(t) = \int_0^t \delta(\tau) d\tau \quad (109)$$

$$\eta_r(t) = \phi_{r,j}^* e^{\lambda_r^* t} \quad (110)$$

The impulse response function components for this mode and the corresponding conjugate mode are:

$$h_{r,ij}^*(t) = \phi_{r,i}^* \phi_{r,j}^* e^{\lambda_r^* t} \quad (111)$$

$$\bar{h}_{r,ij}^*(t) = \bar{\phi}_{r,i}^* \bar{\phi}_{r,j}^* e^{\bar{\lambda}_r^* t} \quad (112)$$

Note that the eigenvalue,  $\lambda_r^*$ , and the eigenvectors,  $\phi_{r,i}^*, \phi_{r,j}^*$ , present in this equation is complex. Let these components be expressed as:

$$\lambda_r^* = -a + ib \quad (113)$$

$$\phi_{r,i}^* = c + id \quad (114)$$

$$\phi_{r,j}^* = e + if \quad (115)$$

Here,  $a$  is a nonnegative scalar, all the other components,  $b$  to  $f$ , are scalars.

$$\bar{\lambda}_r^* = -a - ib \quad (116)$$

$$\bar{\phi}_{r,i}^* = c - id \quad (117)$$

$$\bar{\phi}_{r,j}^* = e - if \quad (118)$$

$$h_{r,ij}^*(t) = (c + id)(e + if)e^{(-a+ib)t} \quad (119)$$

$$\bar{h}_{r,ij}^*(t) = (c - id)(e - if)e^{(-a-ib)t} \quad (120)$$

After some manipulations:

$$\begin{aligned} h_{r,ij}^*(t) + \bar{h}_{r,ij}^*(t) &= \frac{(2ce - 2df)}{\sqrt{1 - \zeta^2}} e^{-at} \sin(\omega_r \sqrt{1 - \zeta^2} t - \psi) + \\ &+ \frac{(2ace - 2adf - 2bcf - 2bde)}{\omega_r \sqrt{1 - \zeta^2}} e^{-at} \sin(\omega_r \sqrt{1 - \zeta^2} t) \end{aligned} \quad (121)$$

Where,

$$\psi = \tan^{-1} \frac{1 - \zeta_r^2}{\zeta_r} \quad (122)$$

$$\omega_r = \sqrt{a^2 + b^2} \quad (123)$$

$$\zeta_r = \frac{a}{\omega_r} \quad (124)$$

The impulse response function is obtained by the superposition of  $n$  complex conjugate pair modes:

$$h_{ij}(t) = \sum_{r=1}^n h_{r,ij}^*(t) + \bar{h}_{r,ij}^*(t) \quad (125)$$

### 3.7 Modal coupling

The above formulations can be applied for undamped or proportionally damped parts of the system. For a system with subsystems of different damping ratios, modal coupling can be applied. In modal coupling, the modal parameters of the subsystems are used to obtain the modal parameters of the coupled system. Impulse response functions can be calculated using the modal parameters of the coupled system.

Consider the system given in Figure 3-1. Two subsystems *A* and *B* are coupled to obtain the system *C*. The modal matrices and the eigenvalues of subsystems *A* and *B* are used to obtain the modal matrix and the eigenvalues of the coupled system *C* [47].

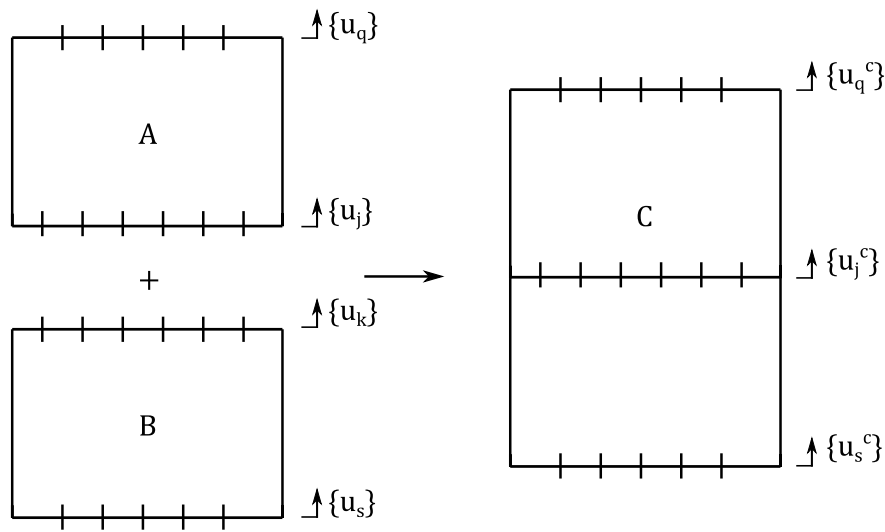


**Figure 3-1.** Subsystems for modal coupling

Equations of motion for these two subsystems are:

$$\begin{bmatrix} [M_{qq}] & [M_{qj}] \\ [M_{jq}] & [M_{jj}] \end{bmatrix} \begin{Bmatrix} \{\ddot{u}_q\} \\ \{\ddot{u}_j\} \end{Bmatrix} + \begin{bmatrix} [K_{qq}] & [K_{qj}] \\ [K_{jq}] & [K_{jj}] \end{bmatrix} \begin{Bmatrix} \{u_q\} \\ \{u_j\} \end{Bmatrix} = \begin{Bmatrix} \{0\} \\ \{F_j\} \end{Bmatrix} \quad (126)$$

$$\begin{bmatrix} [M_{kk}] & [M_{ks}] \\ [M_{sk}] & [M_{ss}] \end{bmatrix} \begin{Bmatrix} \{\dot{u}_k\} \\ \{\dot{u}_s\} \end{Bmatrix} + \begin{bmatrix} [K_{kk}] & [K_{ks}] \\ [K_{sk}] & [K_{ss}] \end{bmatrix} \begin{Bmatrix} \{u_k\} \\ \{u_s\} \end{Bmatrix} = \begin{Bmatrix} \{F_k\} \\ \{0\} \end{Bmatrix} \quad (127)$$

For subsystem  $A$ , the modal matrix,  $[\phi_A]$ , and the eigenvalues,  $[\cdot \omega_{r,A}^2]$ , can be obtained as:

$$[M_A] \begin{Bmatrix} \{\ddot{u}_q\} \\ \{\ddot{u}_j\} \end{Bmatrix} + [K_A] \begin{Bmatrix} \{u_q\} \\ \{u_j\} \end{Bmatrix} = \begin{Bmatrix} \{0\} \\ \{0\} \end{Bmatrix} \quad (128)$$

$$(-\omega^2 [M_A] + [K_A])\{u\} = \{0\} \quad (129)$$

$$[\phi_A]^T [M_A] [\phi_A] = [I] \quad (130)$$

$$[\phi_A]^T [K_A] [\phi_A] = [\cdot \omega_{r,A}^2] \quad (131)$$

Similarly for subsystem  $B$ :

$$[\phi_B]^T [M_B] [\phi_B] = [I] \quad (132)$$

$$[\phi_B]^T [K_B] [\phi_B] = [\omega_{r,B}^2] \quad (133)$$

For each subsystem physical displacements  $\{u\}$  can be written using the modal matrix  $[\phi]$  :

$$\{u_A\} = [\phi_A] \{\eta_A\} \quad (134)$$

$$\{u_B\} = [\phi_B] \{\eta_B\} \quad (135)$$

Here  $\{\eta\}$  is the modal coordinate vector.

$$\{u_A\} = \begin{Bmatrix} \{u_q\} \\ \{u_j\} \end{Bmatrix} = \begin{bmatrix} \phi_{q,A} \\ \phi_{j,A} \end{bmatrix} \{\eta_A\} \quad (136)$$

$$\{u_B\} = \begin{Bmatrix} \{u_k\} \\ \{u_s\} \end{Bmatrix} = \begin{bmatrix} \phi_{k,B} \\ \phi_{s,B} \end{bmatrix} \{\eta_B\} \quad (137)$$

The equations of motion are written in the modal coordinates as:

$$[I]\{\ddot{\eta}_A\} + [\omega_{r,A}^2]\{\eta_A\} = [\phi_{j,A}]^T \{F_j\} \quad (138)$$

$$[I]\{\ddot{\eta}_B\} + [\omega_{r,B}^2]\{\eta_B\} = [\phi_{k,B}]^T \{F_k\} \quad (139)$$

$$[I] \begin{Bmatrix} \ddot{\eta}_A \\ \ddot{\eta}_B \end{Bmatrix} + \begin{bmatrix} \omega_{r,A}^2 & 0 \\ 0 & \omega_{r,B}^2 \end{bmatrix} \begin{Bmatrix} \eta_A \\ \eta_B \end{Bmatrix} = \begin{bmatrix} \phi_{j,A}^T & 0 \\ 0 & \phi_{k,B}^T \end{bmatrix} \begin{Bmatrix} F_j \\ F_k \end{Bmatrix} \quad (140)$$

In order to have rigid coupling:

$$\{u_A\} = \{u_B\} \quad (141)$$

$$[\phi_{j,A} \quad -\phi_{k,B}] \begin{Bmatrix} \eta_A \\ \eta_B \end{Bmatrix} = [S]\{\eta\} = \{0\} \quad (142)$$

The constraint matrix  $[S]$  can be partitioned as:

$$[S_d \quad S_i] \begin{Bmatrix} \eta_d \\ \eta_i \end{Bmatrix} = \{0\} \quad (143)$$

Here, modal coordinates for the coupled system are divided into two groups as dependent,  $\{\eta_d\}$ , and independent coordinates,  $\{\eta_i\}$ .  $[S_d]$  is a non-singular square matrix and the matrix  $[S_i]$  is the remaining part of the constraint matrix  $[S]$ .

$$\{\eta_d\} = -[S_d]^{-1}[S_i]\{\eta_i\} \quad (144)$$

$$\begin{Bmatrix} \eta_A \\ \eta_B \end{Bmatrix} = \begin{Bmatrix} \eta_d \\ \eta_i \end{Bmatrix} = \begin{bmatrix} -[S_d]^{-1}[S_i] \\ [I] \end{bmatrix} \{\eta_i\} \quad (145)$$

$$\begin{Bmatrix} \eta_A \\ \eta_B \end{Bmatrix} = [T]\{p\} \quad (146)$$

Here, the vector  $\{p\}$  is the vector of independent modal coordinates. The equations of motion in modal coordinate can be rewritten as:

$$[M_p]\{\ddot{p}\} + [K_p]\{p\} = \{F_p\} \quad (147)$$

$$[M_p] = [T]^T [T] \quad (148)$$

$$[K_p] = [T]^T \begin{bmatrix} \omega_{r,A}^2 & 0 \\ 0 & \omega_{r,B}^2 \end{bmatrix} [T] \quad (149)$$

$$\{f_p\} = [T]^T \begin{bmatrix} \phi_{j,A}^T & 0 \\ 0 & \phi_{k,B}^T \end{bmatrix} \begin{Bmatrix} F_j \\ F_k \end{Bmatrix} \quad (150)$$

Eigenvalue solution of the matrices  $[K_p]$  and  $[M_p]$  gives the eigenvalues  $\omega_{r,C}^2$  and the eigenvectors  $[\Psi]$ .  $\omega_{r,C}^2$  are the square of the natural frequencies of the coupled system.  $[\Psi]$  is the mode shape for the overall system. The mode shapes are transformed to the original coordinates as:

$$[\phi_C] = \begin{bmatrix} \phi_A & 0 \\ 0 & \phi_B \end{bmatrix} [T][\Psi] \quad (151)$$

The modal coupling formulation presented above is for the undamped system. For the damped system, a similar procedure could be applied. The modal matrices,  $[\phi_A]$  and  $[\phi_B]$ , are replaced by the state space modal matrices,  $[\phi_A^*]$  and  $[\phi_B^*]$ . Similarly the eigenvalue matrices,  $[\cdot \omega_{r,A}^2 \cdot]$  and  $[\cdot \omega_{r,B}^2 \cdot]$ , are replaced by the state space eigenvalue matrices,  $[\cdot \lambda_A^* \cdot]$  and  $[\cdot \lambda_B^* \cdot]$ . The outcomes of the procedure are the state space modal matrix,  $[\phi_C^*]$ , and the state space eigenvalue matrix,  $[\cdot \lambda_C^* \cdot]$ , for the coupled system.

### 3.8 Fixed boundary application by modal coupling

In Chapter 4 of this thesis, formulations will be provided for obtaining modal parameters of soil layers. The formulations will be given for free surface soil

layers. As it will be introduced in Chapter 5, some degrees of freedom are required to be fixed in the proposed model.

Modal coupling procedure can be followed to obtain fixed surface boundary from a free surface boundary. Let the degrees of freedom to be fixed are included in vector  $\{u_{j,A}\}$ . The coupling equations are:

$$\{u_{j,A}\} = \{0\} \quad (152)$$

$$[\phi_{j,A}]\{\eta_A\} = \{0\} \quad (153)$$

Here, the number of rows,  $n_j$ , in matrix  $[\phi_{j,A}]$  is equal to the number of degrees of freedom, and it should be lower than the number of columns in matrix  $[\phi_{j,A}]$ ,  $n_A$ , which is the number of modes considered in the analysis. The constraint matrix can be written using parts of the matrix  $[\phi_{j,A}]$ , obtained by separating in columns:

$$[S_d] = [\phi_{j,A}]_{(:,1:n_j)} \quad (154)$$

$$[S_i] = [\phi_{j,A}]_{(:,n_j+1:n_A)} \quad (155)$$

Equations (144) to (151) can be followed to obtain the modal parameters for the fixed boundary system.

### 3.9 Damping boundary application by modal coupling

Local viscous boundary application is used to model absorption at the boundary [25]. The viscous damping effect can be implemented by the modal coupling method.

The equations of motion are written in the modal coordinates as:

$$[I]\{\dot{\eta}_A\} - [\lambda_A^*]\{\eta_A\} = [\phi_{j,A}^*]^T \{F_j\} \quad (156)$$

$$\begin{bmatrix} [0] & [M_B] \\ [M_B] & [C_B] \end{bmatrix} \begin{Bmatrix} \{\ddot{u}_B\} \\ \{\dot{u}_B\} \end{Bmatrix} + \begin{bmatrix} -[M_B] & [0] \\ [0] & [K_B] \end{bmatrix} \begin{Bmatrix} \{\dot{u}_B\} \\ \{u_B\} \end{Bmatrix} = \begin{Bmatrix} \{0\} \\ \{F_k\} \end{Bmatrix} \quad (157)$$

$$\begin{aligned} & \begin{bmatrix} [I] & [0] \\ [0] & \begin{bmatrix} [0] & [M_B] \\ [M_B] & [C_B] \end{bmatrix} \end{bmatrix} \begin{Bmatrix} \{\dot{\eta}_A\} \\ \{\dot{y}_B\} \end{Bmatrix} + \begin{bmatrix} -[\lambda_A^*] & [0] \\ [0] & \begin{bmatrix} -[M_B] & [0] \\ [0] & [K_B] \end{bmatrix} \end{bmatrix} \begin{Bmatrix} \{\eta_A\} \\ \{y_B\} \end{Bmatrix} \\ & = \begin{bmatrix} \phi_{j,A}^T & 0 \\ 0 & I \end{bmatrix} \begin{Bmatrix} \{F_j\} \\ \{F_k\} \end{Bmatrix} \end{aligned} \quad (158)$$

Note that for the case with only viscous damping is present, the mass and stiffness matrices,  $[M_B]$  and  $[K_B]$ , are zero.

The coupling equations are:

$$\{u_A\} = \{u_B\} \quad (159)$$

$$[\phi_{j,A} \quad -I] \begin{Bmatrix} \{\eta_A\} \\ \{y_B\} \end{Bmatrix} = \{0\} \quad (160)$$

Here, the size of the identity matrix is equal to the number of coordinates in  $\{y_B\}$ .

The constraint equation can also be written as:

$$\{y_B\} = [\phi_{j,A}]\{\eta_A\} \quad (161)$$

Comparing this formation with the previous constraint equation:

$$[T] = \begin{bmatrix} \phi_{j,A} \\ I \end{bmatrix} \quad (162)$$

Constraint matrices can be written as:

$$[M_p] = [T]^T \begin{bmatrix} [I] & [0] \\ [0] & \begin{bmatrix} [0] & [0] \\ [0] & [C_B] \end{bmatrix} \end{bmatrix} [T] \quad (163)$$

$$[K_p] = [T]^T \begin{bmatrix} -[\lambda_A^*] & 0 \\ 0 & 0 \end{bmatrix} [T] \quad (164)$$

Solution of the eigenvalue problem gives the modal parameters for the system with local viscous boundary condition applied.

### 3.10 Selection of degrees of freedom for modal coupling

The number of constraint equations for modal coupling depends on the number of degrees of freedom in the contact surface of two layers. In the calculations performed in this study, numerical stability problems are observed for the cases with large number of constraint equations. A new set of degrees of freedom are selected on the contact surface, so that modal coupling is applied practically without numerical problems. The values of displacements on this new set are calculated by interpolation on the original degrees of freedom set. Fourth-order interpolations are performed by following the procedure given in [48].

In the applications of fixed boundary and local boundary damping by modal coupling, a similar interpolation scheme is followed. For the local damping boundary, the damping coefficients on the local boundary are calculated considering the total number of damping elements.

### 3.11 Modal parameters for proportional material properties

Finite difference modeling of soil layers will be presented in Chapter 4. Inputs of the model are the geometry of the model and the material properties. The geometry of the model is dimensions of the layer and mesh distribution. The

material properties of the soil layer are Young's modulus, Poisson's ratio, density and damping coefficient. Modal parameters are obtained as the outcome of the model.

It may be practical to modify the results of a model, if only one input parameter is varied. The stiffness matrix is directly proportional to the Young's modulus and the mass matrix is directly proportional with the density.

It can be shown that for the same geometry, density and Poisson's ratio; if the Young's modulus is changed from  $E_1$  to  $E_2 = aE_1$ , the stiffness matrices will also be proportional as  $[K_2] = a[K_1]$ . Then, the undamped eigenvalues, therefore the natural frequencies, will also be proportional as:

$$\lambda_{r,2} = a\lambda_{r,1} \quad (165)$$

$$\omega_{r,2} = \sqrt{a}\omega_{r,1} \quad (166)$$

As the change in Young's modulus does not change the mass matrix, the undamped eigenvectors will be the same.

For the case of a proportional change in density,  $\rho_2 = b\rho_1$ , *ceteris paribus*; the mass matrices will be proportional as  $[M_2] = b[M_1]$ , while the stiffness matrix does not change. Then, the undamped eigenvalues and the natural frequencies can be written as:

$$\lambda_{r,2} = \frac{1}{b}\lambda_{r,1} \quad (167)$$

$$\omega_{r,2} = \frac{1}{\sqrt{b}}\omega_{r,1} \quad (168)$$

Revisiting equations (21) to (23), the undamped eigenvectors can be related as:

$$\{\phi_{r,2}\} = \frac{1}{\sqrt{b}}\{\phi_{r,1}\} \quad (169)$$

If both Young's modulus and density are changed as  $E_2 = aE_1$  and  $\rho_2 = b\rho_1$ , then the undamped eigenvalues are given as:

$$\lambda_{r,2} = \frac{a}{b}\lambda_{r,1} \quad (170)$$

$$\omega_{r,2} = \sqrt{\frac{a}{b}}\omega_{r,1} \quad (171)$$

while, Equation (169) is still valid for the undamped eigenvectors.

For the damped models, if the damping coefficient remains the same, the damped modal parameters can also be related. For two different subsystems, if the geometry, Poisson's ratio and damping coefficient are the same, and Young's modulus and density change as  $E_2 = aE_1$  and  $\rho_2 = b\rho_1$ ; the damped eigenvalues can be written as:

$$\lambda_{r,2}^* = \sqrt{\frac{a}{b}}\lambda_{r,1}^* \quad (172)$$

Similarly the eigenvectors can be written as:

$$\{\phi_{r,2}^*\} = \frac{1}{\sqrt{b}}\{\phi_{r,1}^*\} \quad (173)$$

It should be note that, equations (172) and (173) are valid for the systems after the application of the local boundary damping, since the damping coefficients for local boundary are also proportional to the material properties.



## CHAPTER 4

### FINITE DIFFERENCE FORMULATION

In this chapter, finite difference formulation for modeling of elastic wave motion in layered ground is presented. Governing equations and boundary conditions are discussed in detail. These equations are implemented to obtain modal parameters of soil layers.

#### 4.1 Governing equations

For three-dimensional soil motion, equations of motion can be written as:

$$\rho \frac{\partial^2 u}{\partial t^2} = \frac{\partial \sigma_{xx}}{\partial x} + \frac{\partial \sigma_{xy}}{\partial y} + \frac{\partial \sigma_{xz}}{\partial z} \quad (174)$$

$$\rho \frac{\partial^2 v}{\partial t^2} = \frac{\partial \sigma_{xy}}{\partial x} + \frac{\partial \sigma_{yy}}{\partial y} + \frac{\partial \sigma_{yz}}{\partial z} \quad (175)$$

$$\rho \frac{\partial^2 w}{\partial t^2} = \frac{\partial \sigma_{xz}}{\partial x} + \frac{\partial \sigma_{yz}}{\partial y} + \frac{\partial \sigma_{zz}}{\partial z} \quad (176)$$

Here,  $u$ ,  $v$  and  $w$  represent the displacements in  $x$ ,  $y$  and  $z$  directions, respectively.  $\sigma_{xx}$ ,  $\sigma_{yy}$  and  $\sigma_{zz}$  are the normal stress components, while  $\sigma_{xy}$ ,  $\sigma_{xz}$  and  $\sigma_{yz}$  are the shear components. Hooke's law can be written for these displacement and stress components as:

$$\sigma_{xx} = (\lambda + 2\mu) \frac{\partial u}{\partial x} + \lambda \frac{\partial v}{\partial y} + \lambda \frac{\partial w}{\partial z} \quad (177)$$

$$\sigma_{yy} = \lambda \frac{\partial u}{\partial x} + (\lambda + 2\mu) \frac{\partial v}{\partial y} + \lambda \frac{\partial w}{\partial z} \quad (178)$$

$$\sigma_{zz} = \lambda \frac{\partial u}{\partial x} + \lambda \frac{\partial v}{\partial y} + (\lambda + 2\mu) \frac{\partial w}{\partial z} \quad (179)$$

$$\sigma_{xy} = \mu \left( \frac{\partial u}{\partial y} + \frac{\partial v}{\partial x} \right) \quad (180)$$

$$\sigma_{xz} = \mu \left( \frac{\partial u}{\partial z} + \frac{\partial w}{\partial x} \right) \quad (181)$$

$$\sigma_{yz} = \mu \left( \frac{\partial v}{\partial z} + \frac{\partial w}{\partial y} \right) \quad (182)$$

Assuming harmonic motion of the ground, the equations of motion can be transformed from time domain to frequency domain.

$$-\rho\omega^2 \hat{u} = \frac{\partial \hat{\sigma}_{xx}}{\partial x} + \frac{\partial \hat{\sigma}_{xy}}{\partial y} + \frac{\partial \hat{\sigma}_{xz}}{\partial z} \quad (183)$$

$$-\rho\omega^2 \hat{v} = \frac{\partial \hat{\sigma}_{xy}}{\partial x} + \frac{\partial \hat{\sigma}_{yy}}{\partial y} + \frac{\partial \hat{\sigma}_{yz}}{\partial z} \quad (184)$$

$$-\rho\omega^2 \hat{w} = \frac{\partial \hat{\sigma}_{xz}}{\partial x} + \frac{\partial \hat{\sigma}_{yz}}{\partial y} + \frac{\partial \hat{\sigma}_{zz}}{\partial z} \quad (185)$$

Here,  $\omega$  is the frequency term and the hat symbol represents the transformed version of the corresponding component. As the solution is to be obtained in modal domain, one can write these equations without the hat symbol for further simplicity.

$$-\rho\omega^2 u = \frac{\partial \sigma_{xx}}{\partial x} + \frac{\partial \sigma_{xy}}{\partial y} + \frac{\partial \sigma_{xz}}{\partial z} \quad (186)$$

$$-\rho\omega^2 v = \frac{\partial \sigma_{xy}}{\partial x} + \frac{\partial \sigma_{yy}}{\partial y} + \frac{\partial \sigma_{yz}}{\partial z} \quad (187)$$

$$-\rho\omega^2 w = \frac{\partial \sigma_{xz}}{\partial x} + \frac{\partial \sigma_{yz}}{\partial y} + \frac{\partial \sigma_{zz}}{\partial z} \quad (188)$$

Equations (177) to (182) and (186) to (188) are the governing equations for the wave motion within the soil. These equations are to be used for all the points or nodes in the domain, except the nodes on the boundaries.

## 4.2 Staggered grid modeling

Staggered grid is used in the finite difference model. In each direction, a displacement and a stress component is placed in successive grid locations. As seen in Figure 4-1, the nodes for displacement component  $u$  and the nodes for the stress component  $\sigma_{xx}$  are aligned in  $x$  direction. Similarly, the nodes for  $u$  and for  $\sigma_{xy}$  are aligned in  $y$  direction. The same observation can be performed between other displacement and stress components.

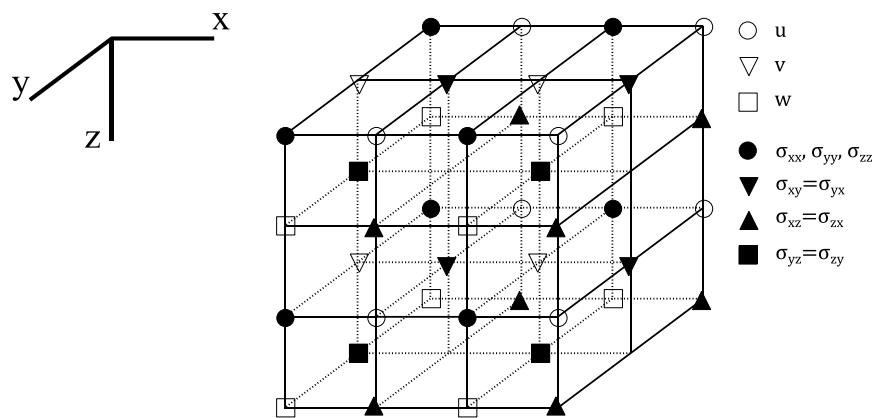


**Figure 4-1.** Three-dimensional staggered grid

### 4.3 Finite difference formulation for general equations

Central difference formulations are used for the derivatives in the governing equations, as long as they are applicable. Consider the Hooke's law for the stress component  $\sigma_{xx}$  at node  $(i, j, k)$  in Figure 4-2. For the application of the Hooke's law for  $\sigma_{xx}$  given in Equation (177), one needs the derivatives  $\frac{\partial u}{\partial x}$ ,  $\frac{\partial v}{\partial y}$  and  $\frac{\partial w}{\partial z}$ . The fourth-order finite difference approximations for these derivatives can be written as:

$$\frac{\partial u}{\partial x} = \frac{1}{h_x} \left( -\frac{1}{24} \left( u|_{i+\frac{3}{2},j,k} - u|_{i-\frac{3}{2},j,k} \right) + \frac{9}{8} \left( u|_{i+\frac{1}{2},j,k} - u|_{i-\frac{1}{2},j,k} \right) \right) \quad (189)$$

$$\frac{\partial v}{\partial y} = \frac{1}{h_y} \left( -\frac{1}{24} \left( v|_{i,j+\frac{3}{2},k} - v|_{i,j-\frac{3}{2},k} \right) + \frac{9}{8} \left( v|_{i,j+\frac{1}{2},k} - v|_{i,j-\frac{1}{2},k} \right) \right) \quad (190)$$

$$\frac{\partial w}{\partial z} = \frac{1}{h_z} \left( -\frac{1}{24} \left( w|_{i,j,k+\frac{3}{2}} - w|_{i,j,k-\frac{3}{2}} \right) + \frac{9}{8} \left( w|_{i,j,k+\frac{1}{2}} - w|_{i,j,k-\frac{1}{2}} \right) \right) \quad (191)$$

Here  $h_x$ ,  $h_y$  and  $h_z$  are the distances between neighboring nodes in  $x$ ,  $y$  and  $z$  directions, respectively. For the Hooke's law formulation of stress components other than  $\sigma_{xx}$ , similar derivatives can be expressed by finite differences.

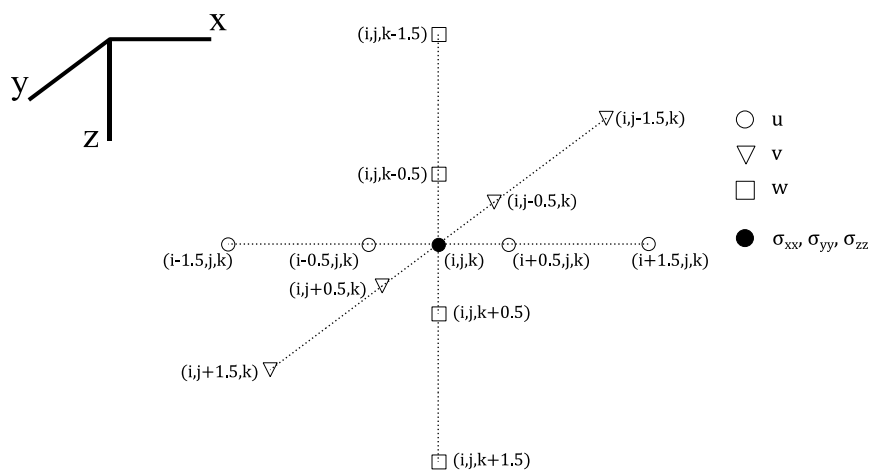


**Figure 4-2.** Finite difference nodes for normal stress components

In the equations of motion, Equations (186) to (188), first degree derivatives as  $\frac{\partial \sigma_{xx}}{\partial x}$  are present. For the derivative terms in Equation (186), the fourth-order finite difference approximations are given in the following equations:

$$\begin{aligned} \frac{\partial \sigma_{xx}}{\partial x} = \frac{1}{h_x} & \left( -\frac{1}{24} \left( \sigma_{xx}|_{i+\frac{3}{2},j,k} - \sigma_{xx}|_{i-\frac{3}{2},j,k} \right) \right. \\ & \left. + \frac{9}{8} \left( \sigma_{xx}|_{i+\frac{1}{2},j,k} - \sigma_{xx}|_{i-\frac{1}{2},j,k} \right) \right) \end{aligned} \quad (192)$$

$$\begin{aligned} \frac{\partial \sigma_{xy}}{\partial y} = \frac{1}{h_y} & \left( -\frac{1}{24} \left( \sigma_{xy}|_{i,j+\frac{3}{2},k} - \sigma_{xy}|_{i,j-\frac{3}{2},k} \right) \right. \\ & \left. + \frac{9}{8} \left( \sigma_{xy}|_{i,j+\frac{1}{2},k} - \sigma_{xy}|_{i,j-\frac{1}{2},k} \right) \right) \end{aligned} \quad (193)$$

$$\begin{aligned} \frac{\partial \sigma_{xz}}{\partial z} = \frac{1}{h_z} & \left( -\frac{1}{24} \left( \sigma_{xz}|_{i,j,k+\frac{3}{2}} - \sigma_{xz}|_{i,j,k-\frac{3}{2}} \right) \right. \\ & \left. + \frac{9}{8} \left( \sigma_{xz}|_{i,j,k+\frac{1}{2}} - \sigma_{xz}|_{i,j,k-\frac{1}{2}} \right) \right) \end{aligned} \quad (194)$$

Similar finite difference approximations can be written for the derivatives in Equations (187) and (188).

#### 4.4 Boundary conditions

For a soil layer surface, different boundary conditions are possible: free surface boundary where the traction components are zero, fixed surface boundary where the displacements are zero, material discontinuity where the displacement and traction components are compatible with the neighboring layer, and local viscous boundary where viscous dampers are present to model the truncation of the domain. In this section, free boundary formulation is presented. The remaining possible boundary conditions can be implemented by following the formulations given in Chapter 3.

For the nodes on a boundary or near a boundary, central difference approximations may not be applicable. This is due to the absence of the nodes beyond the free surface. Therefore, for the calculation of the components near the free surface, adjusted finite difference approximations are applied. In the adjusted finite difference approximations, the present nodes near the boundary are used to approximate the derivatives.

Kristek et al. presented two different adjusted finite difference formulations for free surfaces in 3D [49]. These two formulations are H-AFDA formulation and W-AFDA formulation. In the W-AFDA formulation, the nodes for displacement component in normal direction are on the surface of the grid. In the H-AFDA formulation, the nodes for displacement components other than normal direction are on the surface of the grid. In this study, the W-AFDA formulation is applied. The details of this formulation are given below.

Consider the free surface  $z = 0$  shown in Figure 4-3. For the displacement and stress components at  $0 \leq z \leq h_z$ , central difference differentiation is not applicable.

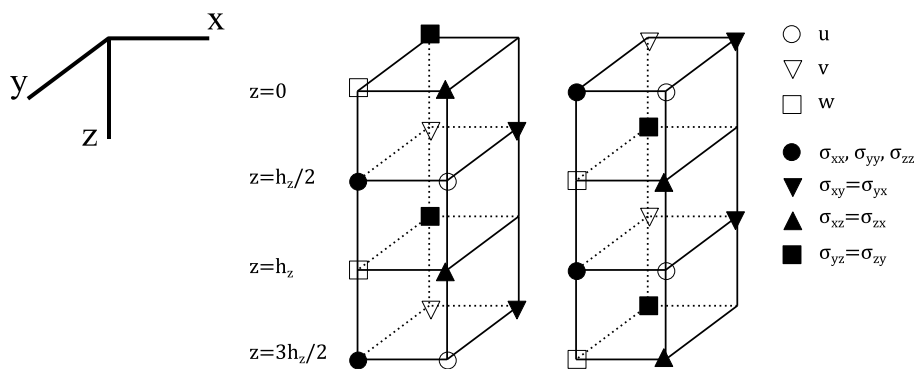


**Figure 4-3.** Nodes for W-AFDA (left) and H-AFDA (right) formulations

In the W-AFDA configuration; on the free surface ( $z = 0$ ), there are nodes for two stress components:  $\sigma_{xz}$  and  $\sigma_{yz}$ . This surface is traction free, therefore these stress components are zero:

$$\sigma_{xz}(0) = 0 \quad (195)$$

$$\sigma_{yz}(0) = 0 \quad (196)$$

As shear stress components are zero on free surface, from Equations (181) and (182), one can relate displacement derivatives:

$$\frac{\partial u}{\partial z} = -\frac{\partial w}{\partial x} \text{ at } z = 0 \quad (197)$$

$$\frac{\partial v}{\partial z} = -\frac{\partial w}{\partial y} \text{ at } z = 0 \quad (198)$$

On the layer  $z = h_z/2$  are three normal stress components:  $\sigma_{xx}$ ,  $\sigma_{yy}$  and  $\sigma_{zz}$  and shear component  $\sigma_{xy}$ . For the normal stress components, the approximation given in Equation (199) can be used for the derivative  $\frac{\partial w}{\partial z}$ . The displacement values at  $z = 0$  to  $z = 4h_z$  are used with  $z_0 = h_z/2$ .

$$f'(z_0) = \frac{1}{h_z} \left[ -\frac{11}{12} f\left(z_0 - \frac{h_z}{2}\right) + \frac{17}{24} f\left(z_0 + \frac{h_z}{2}\right) + \frac{3}{8} f\left(z_0 + \frac{3}{2}h_z\right) - \frac{5}{24} f\left(z_0 + \frac{5}{2}h_z\right) + \frac{1}{24} f\left(z_0 + \frac{7}{2}h_z\right) \right] + O(h^4) \quad (199)$$

Note that for the shear stress component  $\sigma_{xy}(h_z/2)$ , there is no derivative in  $z$  direction, therefore central difference is applicable.

On the layer  $z = h_z$ , there are two stress components:  $\sigma_{xz}$  and  $\sigma_{yz}$ . The approximation given in Equation (200) can be used for the derivatives  $\frac{\partial u}{\partial z}$  and  $\frac{\partial v}{\partial z}$ . The displacement values at  $z = h_z/2$  to  $z = 7h_z/2$  are used with  $z_0 = h_z$ . For the

derivatives  $\frac{\partial u}{\partial z}$  and  $\frac{\partial v}{\partial z}$  at  $z = 0$ , the derivatives  $\frac{\partial w}{\partial x}$  and  $\frac{\partial w}{\partial y}$  can be used following Equations (197) and (198), respectively.

$$f'(z_0) = \frac{1}{h_z} \left[ -\frac{h_z}{22} f'(z_0 - h_z) - \frac{577}{528} f\left(z_0 - \frac{h_z}{2}\right) + \frac{201}{176} f\left(z_0 + \frac{h_z}{2}\right) - \frac{9}{176} f\left(z_0 + \frac{3}{2}h_z\right) + \frac{1}{528} f\left(z_0 + \frac{5}{2}h_z\right) \right] + O(h^4) \quad (200)$$

Displacement component  $w$  are present on the free surface at  $z = 0$ . In the equation of motion for these displacement components, Equation (188), there is the derivative  $\frac{\partial \sigma_{zz}}{\partial z}$  in  $z$  direction. To approximate this derivative, Equation (201) can be used for stress components at  $z = h_z/2$  to  $z = 7h_z/2$  with  $z_0 = 0$ . Note that as the free surface is traction free, normal stress component is zero on the surface:  $\sigma_{zz}(0) = 0$ .

$$f'(z_0) = \frac{1}{h_z} \left[ -\frac{352}{105} f(z_0) + \frac{35}{8} f\left(z_0 + \frac{h_z}{2}\right) - \frac{35}{24} f\left(z_0 + \frac{3}{2}h_z\right) + \frac{21}{40} f\left(z_0 + \frac{5}{2}h_z\right) - \frac{5}{56} f\left(z_0 + \frac{7}{2}h_z\right) \right] + O(h^4) \quad (201)$$

Displacement components  $u$  and  $v$  are on the layer  $z = h_z/2$ . As seen in Equations (186) and (187), the necessary derivatives in  $z$  direction are  $\frac{\partial \sigma_{xz}}{\partial z}$  and  $\frac{\partial \sigma_{yz}}{\partial z}$ . Approximation given in Equation (199) can be used for these derivatives by using stress components at  $z = 0$  to  $z = 4h_z$  with  $z_0 = h_z/2$ .

On the layer  $z = h_z$ , there are displacement components  $w$ . The approximation given in Equation (202) can be used for the derivative  $\frac{\partial \sigma_{zz}}{\partial z}$ . The stress values at  $z = h_z/2$  to  $z = 7h_z/2$  are used with  $z_0 = h_z$ . Note that normal stress component is zero on the surface:  $\sigma_{zz}(0) = 0$ .

$$f'(z_0) = \frac{1}{h_z} \left[ \frac{16}{105} f(z_0 - h_z) - \frac{31}{24} f\left(z_0 - \frac{h_z}{2}\right) + \frac{29}{24} f\left(z_0 + \frac{h_z}{2}\right) - \frac{3}{40} f\left(z_0 + \frac{3}{2} h_z\right) + \frac{1}{168} f\left(z_0 + \frac{5}{2} h_z\right) \right] + O(h^4) \quad (202)$$

#### 4.5 Implementation of equations

The finite difference equations presented in previous sections are implemented in MATLAB. The governing equations are implemented first, and then the terms for the boundary conditions are introduced. All the equations are written in a matrix form as:

$$[A]\{u\sigma\} = \{b\} \quad (203)$$

Here  $\{u\sigma\}$  is the vector with displacement and stress components.

$$\{u\sigma\} = \begin{Bmatrix} u \\ v \\ w \\ \sigma_{xx} \\ \sigma_{yy} \\ \sigma_{zz} \\ \sigma_{xy} \\ \sigma_{xz} \\ \sigma_{yz} \end{Bmatrix} \quad (204)$$

Equation (203) can also be shown as:

$$\begin{bmatrix} A_{11} & A_{12} \\ A_{21} & A_{22} \end{bmatrix} \{u\sigma\} = \{b\} \quad (205)$$

The equations in upper rows of Equation (205) represent the equations of motion for displacement components, with the inclusion of boundary conditions. The equations in the lower part of the same equation represent the equations for

Hooke's law for stress components, again with the inclusion of boundary conditions.

The submatrix  $[A_{11}]$  is a diagonal matrix with elements of  $-\rho\omega^2$ . Similarly, the submatrix  $[A_{22}]$  is also a diagonal matrix with elements of 1. As free boundary problem is assumed, the vector  $\{b\}$  is a zero vector with length equal to  $\{u\sigma\}$ .

Modal analysis can be performed to Equation (205). This equation should be modified to obtain a form as:

$$[[K] - \omega^2[M]]\{x\} = \{0\} \quad (206)$$

Consider the two parts of Equation (205):

$$[A_{11}]\{u\} + [A_{12}]\{\sigma\} = \{0\} \quad (207)$$

$$[A_{21}]\{u\} + [A_{22}]\{\sigma\} = \{0\} \quad (208)$$

One can express the  $\sigma$  term, in terms of  $\{u\}$ , in Equation (207), with the manipulation in Equation (208):

$$\{\sigma\} = -[A_{22}]^{-1}[A_{21}]\{u\} \quad (209)$$

$$[A_{11}]\{u\} - [A_{12}][A_{22}]^{-1}[A_{21}]\{u\} = \{0\} \quad (210)$$

$$[[A_{11}] - [A_{12}][A_{22}]^{-1}[A_{21}]]\{u\} = \{0\} \quad (211)$$

In Equation (211), the terms with  $\omega^2$  appear only in the component  $[A_{11}]$ . Therefore, one can obtain stiffness and mass matrices for the modal analysis as follows:

$$[K] = -[A_{12}][A_{22}]^{-1}[A_{21}] \quad (212)$$

$$[M] = -\frac{1}{\omega^2} [A_{11}] \quad (213)$$

Note that the  $[K]$  matrix includes a matrix inversion of the identity matrix  $[A_{22}]$ . This inversion does not cause any computational effort. Also, note that, a minus sign is included in Equations (212) and (213) in order to have positive elements in the mass matrix.

As a result of modal analysis for  $[K]$  and  $[M]$  matrices, eigenvalues,  $\lambda_r$ , and eigenvectors,  $\{\phi_r\}$ , are obtained. In eigenvectors, displacement variables for the whole domain are listed. Generally, it is enough to keep the displacement variables on the surfaces of the domain. As W-AFDA formulation is applied, on each surface, only the displacement components in the normal direction,  $w$ , are present. Remaining displacement components,  $u$  and  $v$ , can be approximated using the displacement of neighboring nodes.

Equation (201) can be modified as:

$$f(z_0) \cong \frac{105}{352} \left[ -h_z f'(z_0) + \frac{35}{8} f\left(z_0 + \frac{h_z}{2}\right) - \frac{35}{24} f\left(z_0 + \frac{3}{2} h_z\right) + \frac{21}{40} f\left(z_0 + \frac{5}{2} h_z\right) - \frac{5}{56} f\left(z_0 + \frac{7}{2} h_z\right) \right] \quad (214)$$

The first term in this equation can be obtained using the results in Equations (197) for  $u$  and (198) for  $v$ .

#### 4.6 Mesh size comparison and convergence considerations

In this section, results for sample calculation of a single ground layer are analyzed for different mesh sizes. Here, mesh size refers to node spacing in staggered grid formulation presented above. In the analyses, the dimensions of the ground layer is taken as 25.0 m, 50.05 m and 2.0 m in  $x$ ,  $y$  and  $z$  directions, respectively. Young modulus of the layer is 200 MPa, Poisson's ratio is 0.30 and density is  $2000 \text{ kg/m}^3$ . A simple ground layer model is shown in Figure 4-4.

The varied parameter in the analyses is the mesh size which is the distance between nodes in  $x$  and  $y$  directions. This mesh size value is varied between 0.5 m and 2.0 m. The number of nodes in  $z$  direction is eight for all cases. This is due to the application of finite difference equations.

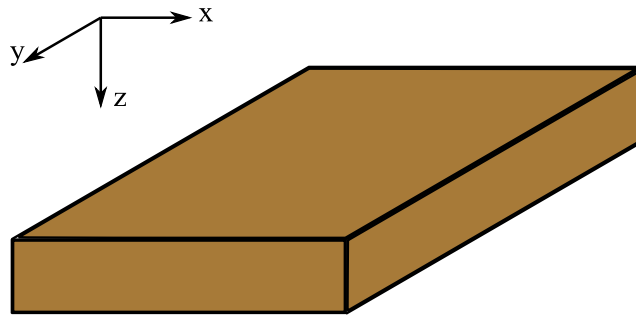


**Figure 4-4.** Ground model

In Figure 4-5 and Figure 4-6, natural frequencies obtained from modal analyses are shown for different mesh sizes. As seen in Figure 4-5, the range of frequencies accurately modeled by finite difference solution depends on mesh size. For mesh sizes higher than 1.1 m, a clear diversion before 100 Hz is observed on modal results. From comparison of results in Figure 4-6, it can be concluded that smaller mesh size improves convergence of results and gives lower number of modes for a specified higher frequency limit. A tradeoff is needed between long processing

times and accuracy. For this reason, with the given data, an optimal value of mesh size is experimented as 0.8 m, for the specified range of frequency.

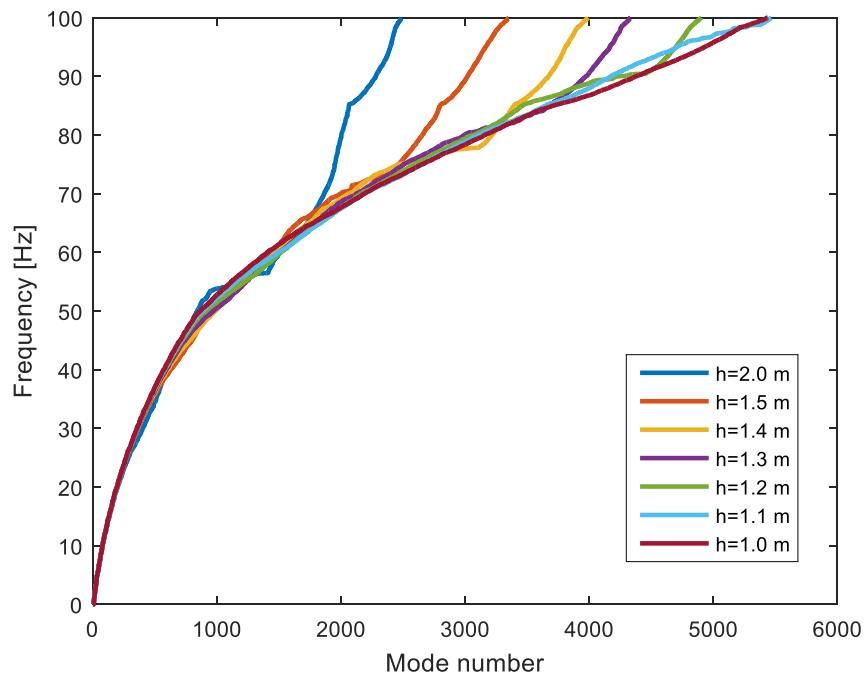


**Figure 4-5.** Modal analysis results for different mesh sizes

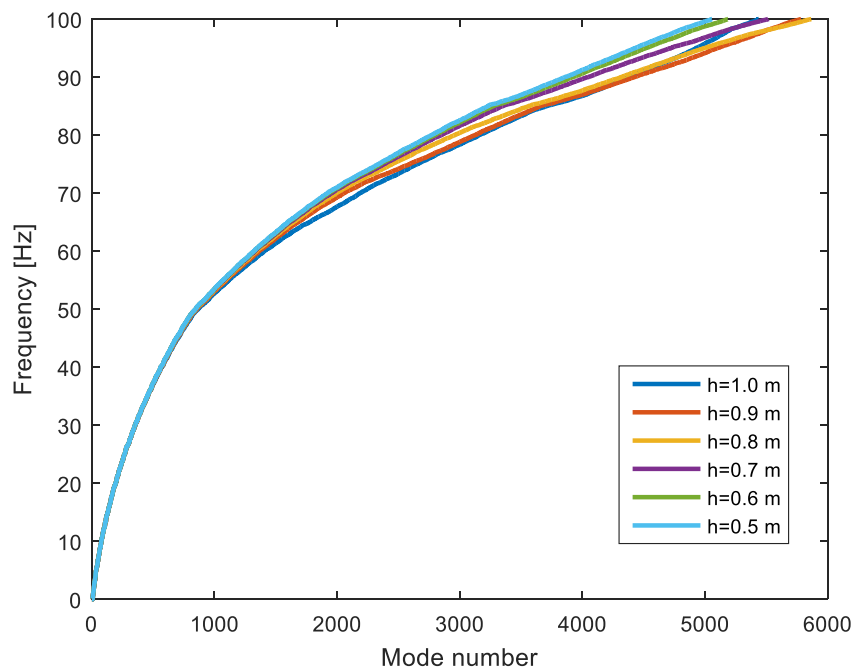


**Figure 4-6.** Modal analysis results for different mesh sizes

#### **4.7 Concluding remarks**

Equations (189) to (194) are central finite difference approximations and Equations (199) to (202) are adjusted finite difference approximations with fourth-order of accuracy [49]. Higher order approximations can be written using more terms in formulations. Fornberg presented formulations for finite difference approximations of arbitrarily spaced nodes [48]. These formulations could be applied for better approximations in finite difference formulations.

## CHAPTER 5

### NUMERICAL MODELING

#### 5.1 Multibody vehicle modeling

A typical three degree of freedom multibody model used in railway vehicle modeling is shown in Figure 5-1. Three lumped masses represent car body mass,  $m_c$ , bogie mass,  $m_b$ , and wheel mass,  $m_w$ . Two suspension levels are present in the model: the primary suspension,  $k_1$  and  $c_1$ , between wheel and bogie masses, and the secondary suspension,  $k_2$  and  $c_2$ , between bogie and car body masses.

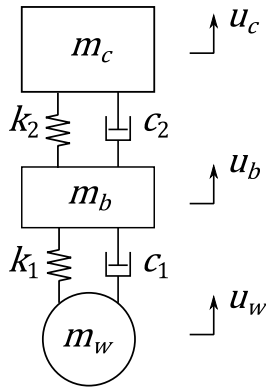


**Figure 5-1.** Typical three degree of freedom vehicle model

Two different types of loadings are applied on the vehicle model: weights of the lumped masses and the rail wheel contact force. The equation of motion can be written for the vehicle as:

$$\begin{aligned}
& \begin{bmatrix} m_c & 0 & 0 \\ 0 & m_b & 0 \\ 0 & 0 & m_w \end{bmatrix} \begin{bmatrix} \ddot{u}_c \\ \ddot{u}_b \\ \ddot{u}_w \end{bmatrix} + \begin{bmatrix} c_2 & -c_2 & 0 \\ -c_2 & c_1 + c_2 & -c_1 \\ 0 & -c_1 & c_1 \end{bmatrix} \begin{bmatrix} \dot{u}_c \\ \dot{u}_b \\ \dot{u}_w \end{bmatrix} + \\
& \begin{bmatrix} k_2 & -k_2 & 0 \\ -k_2 & k_1 + k_2 & -k_1 \\ 0 & -k_1 & k_1 \end{bmatrix} \begin{bmatrix} u_c \\ u_b \\ u_w \end{bmatrix} = \begin{bmatrix} -m_c g \\ -m_b g \\ -m_w g + F_{rwc} \end{bmatrix}
\end{aligned} \tag{215}$$

The weights present static loads on each of three degrees of freedom. The weights of the car body and the bogie are transmitted to the wheel through the two suspensions. Therefore, these loadings can be directly applied to the wheel degree of freedom. The wheel-rail contact force will be introduced in Section 5.2.

$$\begin{aligned}
& \begin{bmatrix} m_c & 0 & 0 \\ 0 & m_b & 0 \\ 0 & 0 & m_w \end{bmatrix} \begin{bmatrix} \ddot{u}_c \\ \ddot{u}_b \\ \ddot{u}_w \end{bmatrix} + \begin{bmatrix} c_2 & -c_2 & 0 \\ -c_2 & c_1 + c_2 & -c_1 \\ 0 & -c_1 & c_1 \end{bmatrix} \begin{bmatrix} \dot{u}_c \\ \dot{u}_b \\ \dot{u}_w \end{bmatrix} + \\
& \begin{bmatrix} k_2 & -k_2 & 0 \\ -k_2 & k_1 + k_2 & -k_1 \\ 0 & -k_1 & k_1 \end{bmatrix} \begin{bmatrix} u_c \\ u_b \\ u_w \end{bmatrix} = \begin{bmatrix} 0 \\ 0 \\ -(m_w + m_b + m_c)g + F_{rwc} \end{bmatrix}
\end{aligned} \tag{216}$$

It should be noted that displacement terms  $u_c$  and  $u_b$  in Equation (215) are different from those in Equation (216). There are static differences between these terms. As it will be introduced, only wheel degree of freedom is considered in analyses. Therefore, these differences do not affect further steps of modeling.

The dynamic response of the vehicle can be calculated by the impulse response functions. The vehicle is a damped system, therefore impulse response functions are obtained by implementing the formulations given in Sections 3.4 and 3.6.

$$\begin{aligned}
& \begin{bmatrix} m_c & 0 & 0 \\ 0 & m_b & 0 \\ 0 & 0 & m_w \end{bmatrix} \begin{bmatrix} \ddot{u}_c \\ \ddot{u}_b \\ \ddot{u}_w \end{bmatrix} + \begin{bmatrix} c_2 & -c_2 & 0 \\ -c_2 & c_1 + c_2 & -c_1 \\ 0 & -c_1 & c_1 \end{bmatrix} \begin{bmatrix} \dot{u}_c \\ \dot{u}_b \\ \dot{u}_w \end{bmatrix} + \\
& \begin{bmatrix} k_2 & -k_2 & 0 \\ -k_2 & k_1 + k_2 & -k_1 \\ 0 & -k_1 & k_1 \end{bmatrix} \begin{bmatrix} u_c \\ u_b \\ u_w \end{bmatrix} = \begin{bmatrix} 0 \\ 0 \\ 0 \end{bmatrix} \tag{217}
\end{aligned}$$

It should be noted that one of the three modes of this system is a rigid body mode. The contribution of this mode must be included in the response function. Undamped modal parameters are calculated from mass and stiffness matrix as in Section 3.2, and impulse response function contribution is calculated as in Section 3.3.

As the weights and the rail-wheel contact force are applied on the wheel, the response of the wheel can be calculated using the direct impulse response function for the wheel. It is not necessary to calculate the response of the bogie and car body masses, in contrast to conventional multibody approaches applied in literature. Therefore, the application of impulse response function decreases the computational effort.

## 5.2 Rail wheel contact modeling

The contact between rail and wheel is modeled as a nonlinear Hertzian contact spring as shown in Figure 5-2.

$$F_{rwc} = \begin{cases} k_H(u_r + r - u_w - \Delta_{st})^{1.5} + W & u_r + r > u_w + \Delta_{st} \\ -k_H(-u_r - r + u_w + \Delta_{st})^{1.5} + W & u_w < u_r + r < u_w + \Delta_{st} \\ 0 & u_r + r < u_w \end{cases} \tag{218}$$

Here,  $u_r$  and  $r$  represent the rail displacement and the rail surface irregularity. The nonlinear spring constant is represented by  $k_H$ . The weight load,  $W$ , and the static deflection in the spring,  $\Delta_{st}$ , are given as:

$$W = (m_w + m_b + m_c)g \quad (219)$$

$$\Delta_{st} = \left(\frac{W}{k_H}\right)^{2/3} \quad (220)$$

The forces acting on the rail and the wheel can be written as:

$$F_{rail} = -F_{rwc} \quad (221)$$

$$F_{wheel} = F_{rwc} - W \quad (222)$$

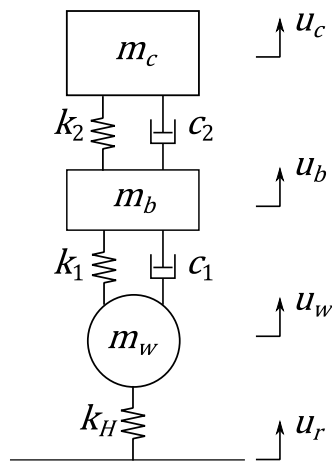


**Figure 5-2.** Rail wheel contact model

### 5.3 Finite element modeling of track

The track is composed of components such as rail, rail pad, sleeper, ballast, subballast and subgrade. A finite element model including all of these layers is built in finite element software ANSYS. Modal analysis is performed in ANSYS to obtain the modal parameters for the track model.

The length of the track in the y-direction along the track is taken as 50.05 m; this distance covers 77 sleepers with spacing of 0.65 m. The front and back surfaces of the model,  $y = 0$  and  $y = 50.05$  m, are modeled as fixed surfaces.

Rail is modeled by three-dimensional two-node Beam188 elements. User defined section is used to define section properties. Rail pads are modeled by spring damper element, combin14 element. They are placed between the nodes on sleepers and rail. Spring constant value is inserted by dividing the rail pad stiffness by the number of combin14 elements. Sleepers, ballast, subballast and subgrade layers are modeled by three-dimensional eight-node Solid185 elements. For under sleeper pad and under ballast mat applications, linear actuator link11 elements are used. Element mesh size taken 0.10 m for all solid and beam elements.

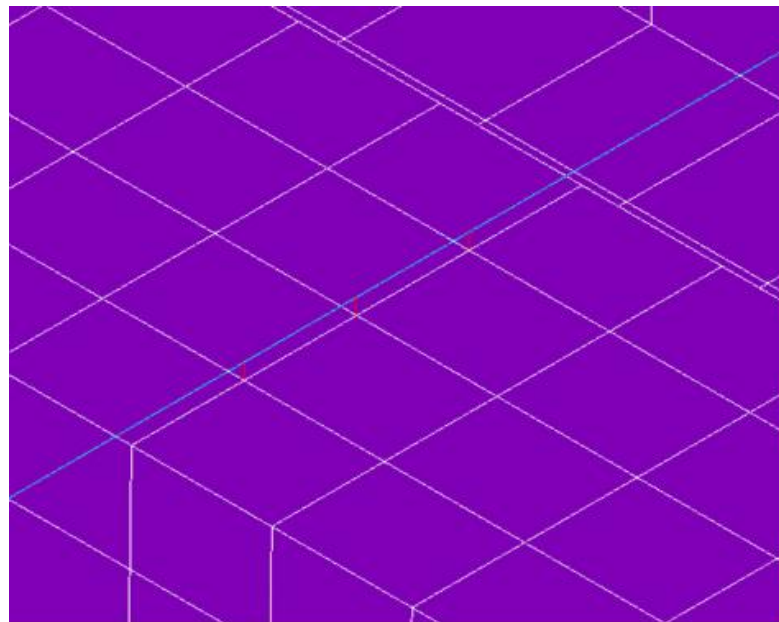


**Figure 5-3.** Rail pad model

Undamped modal analysis is performed in ANSYS and damping is introduced to modal parameters later in MATLAB. Rail pad damping value is not inserted in finite element model and the effect of rail pad damping is modeled by modifying the damped system following modal coupling formulations presented in Chapter 3. The damping of the track model is applied as proportional Rayleigh damping.

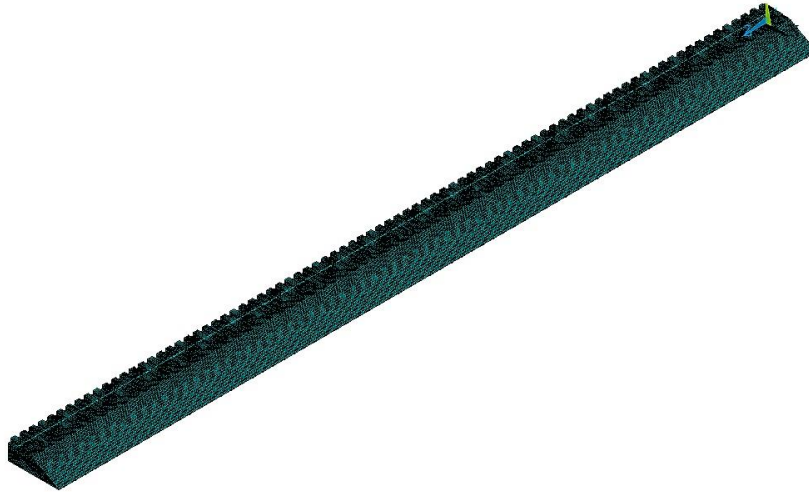


**Figure 5-4.** Finite element model for track

In Figure 5-5, calculation step of undamped modal analysis of track model in ANSYS is shown with input and output parameters.

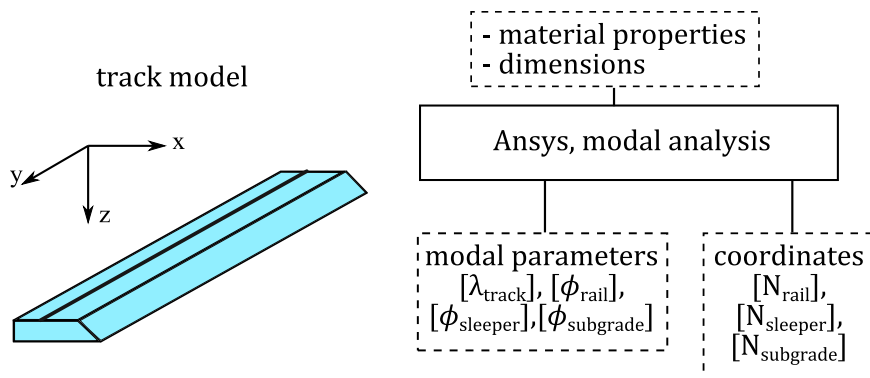


**Figure 5-5.** Undamped modal analysis of track model in ANSYS

Calculation step of damping modification of undamped track modal parameters are shown in Figure 5-6. As already described, proportional damping and rail pad damping are introduced to undamped modal parameters, and damped modal parameters are obtained.

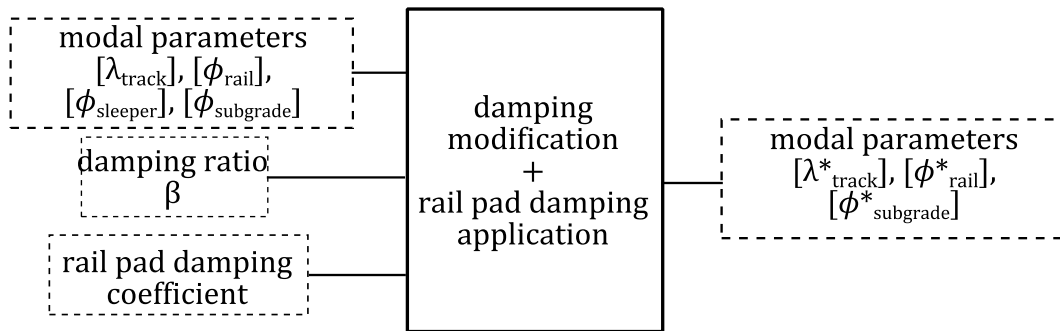


**Figure 5-6.** Modification of track modal parameters for material damping and rail pad damping application

#### 5.4 Finite difference modeling of ground layers

Finite difference modeling described in Chapter 4 is used in the numerical modeling of ground layers. Ground layers are modeled as rectangular prisms as shown in Figure 5-7.

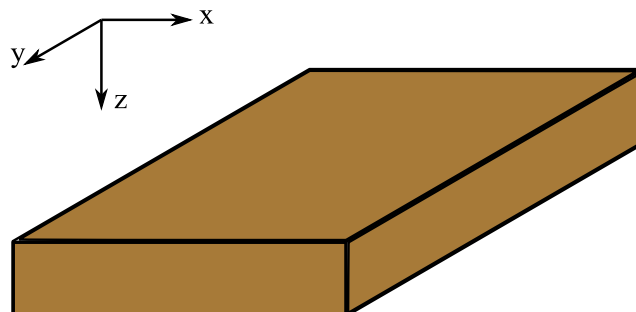


**Figure 5-7.** Ground model

Initially, all surfaces of the ground layers are modelled as free boundary. Finite difference modeling presents the system matrices for free boundary ground layer. Modal parameters for this layer are obtained from eigenvalue analysis on these system matrices. Also, coordinate matrix,  $[N_1]$ , is saved at this step in order to be used in coming coupling steps. In Figure 5-8, calculation steps for soil layer 1 is shown.

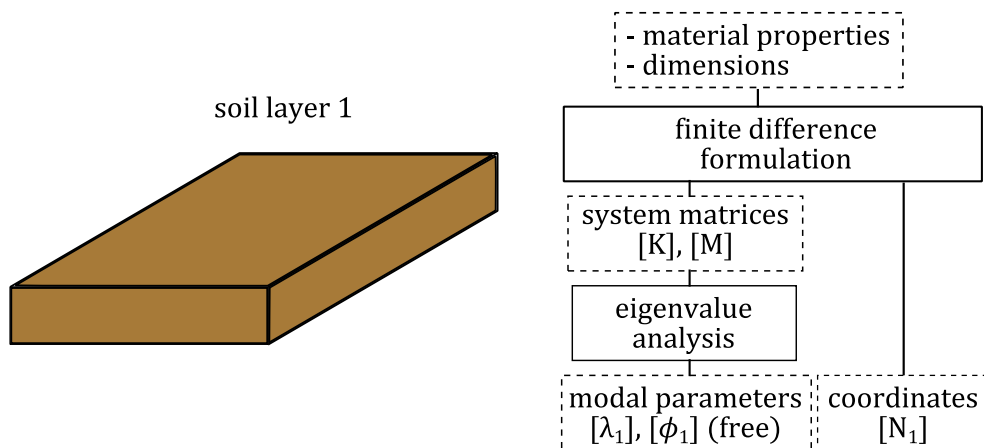


**Figure 5-8.** Calculation steps for soil layer 1

The dimension of ground model in the direction along the train motion, y direction in Figure 5-7, is taken as 50.05 m. In the lateral direction, x-direction in Figure 5-7, the dimension of the model is taken as 25 m. In the left surface of the model,  $x = 0$  surface, a symmetrical boundary condition is applied. This condition is employed by setting  $u_x = 0$  on this surface. By the application of this symmetrical boundary condition, the proposed model is capable of predicting the vibrations in a 50 m length range in lateral direction. The length of ground model in z-direction is dependent on the number and thicknesses of ground layers in analysis. Typical models in studies available in literature include dimension ranges between 10 m and 20 m, for either homogeneous or layered ground models.

Modal parameter calculation for other soil layers is performed following the same procedure. Coupling of soil layers is applied by modal coupling procedure as shown in Figure 5-9. Soil layers are coupled with modal coupling and modal parameters for coupled ground model are calculated.

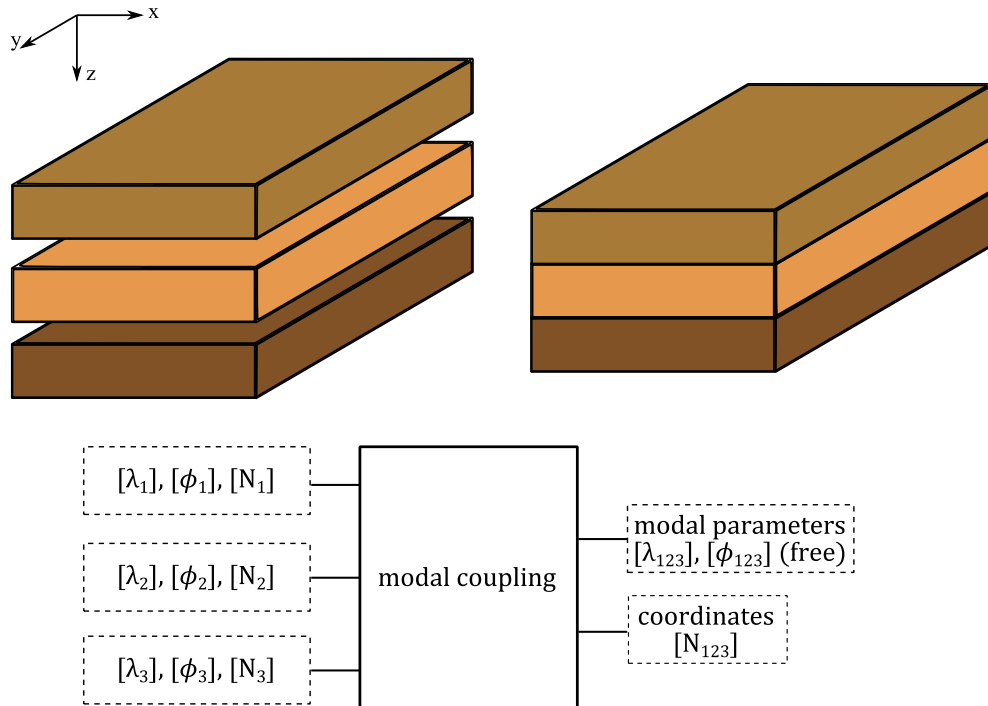


**Figure 5-9.** Coupling of ground layers

As boundary conditions for all coupled ground layers are free before coupling, coupled ground model is also free boundary model yet. Boundary condition application is performed at this step by modal coupling method. In the calculations, coordinates on surfaces  $y = 0$  and  $y = 50.05 \text{ m}$  of coupled ground model are fixed by modal coupling. Also, for symmetry boundary condition at surface  $x = 0$ , displacement in x-direction is fixed. Calculation step for this application is shown in Figure 5-10.

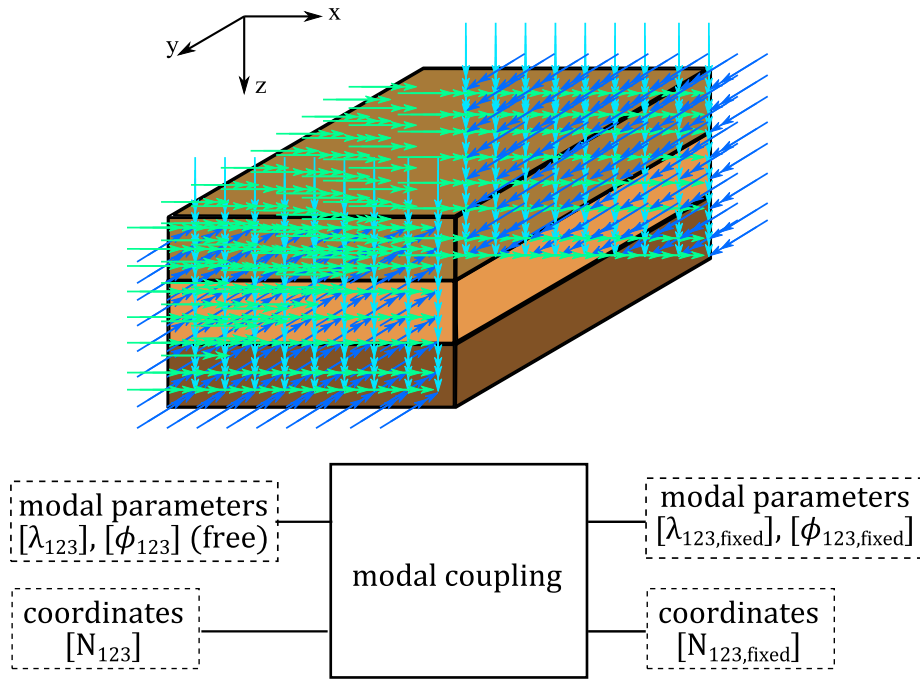


**Figure 5-10.** Fixing coordinates on coupled ground model

After fixing operation on ground model, damping modification is performed and damped modal parameters are obtained, as shown in Figure 5-11.

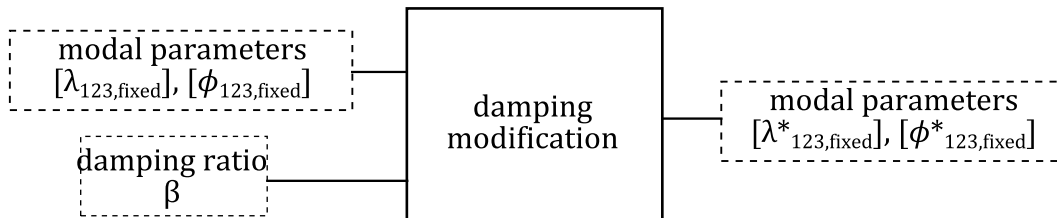


**Figure 5-11.** Modification of undamped ground modes for damping

Local boundary condition is applied in order to model absorption at boundaries of the model. The bottom and right surfaces,  $z = L_z$  and  $x = 25 \text{ m}$ , are modeled as locally damped. In the application of local damping condition, damped modal parameters are used. Modal coupling procedure is applied for local damping modification. Calculation step for local damping application is shown in Figure 5-12.

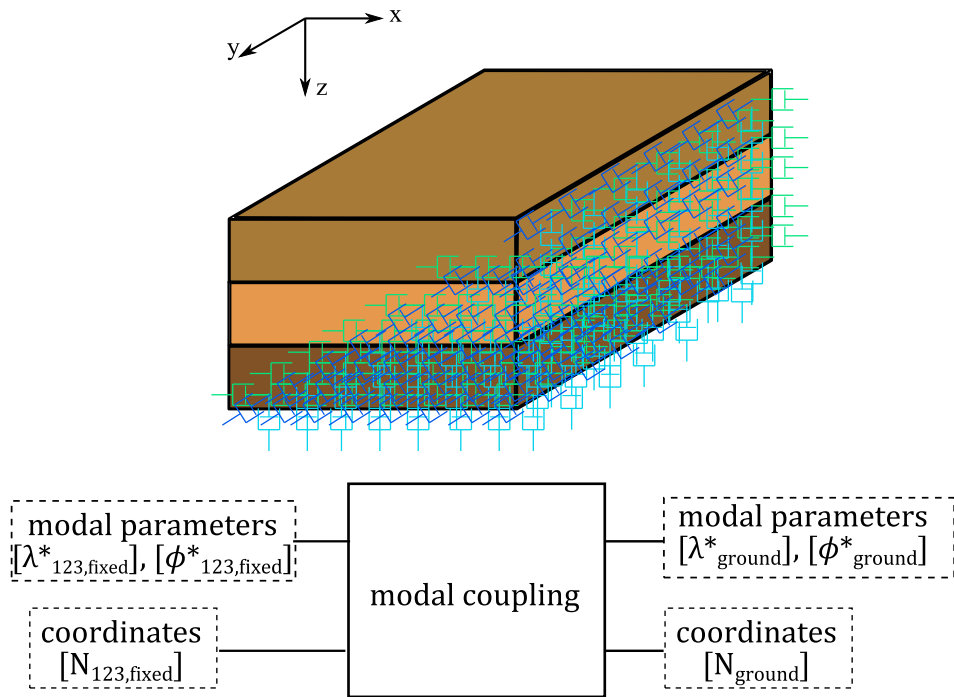


**Figure 5-12.** Local damping boundary coordinates on coupled ground model

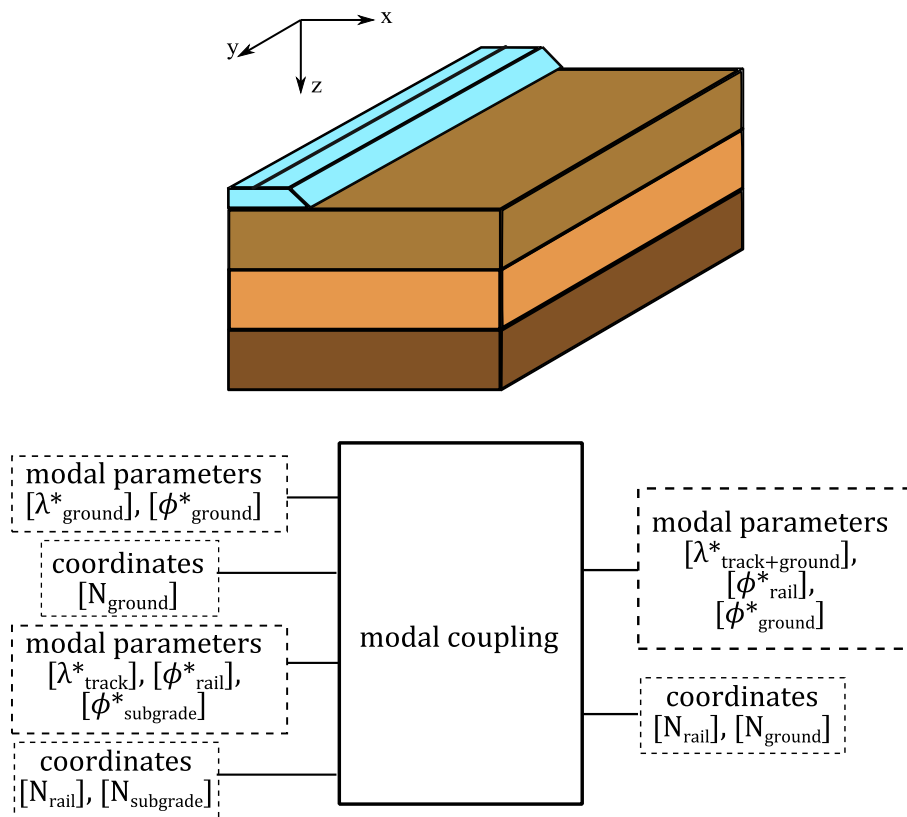


**Figure 5-13.** Coupled ground track model

Ground model and track model are coupled by modal coupling as shown in Figure 5-13, and the modal parameters for the coupled ground track model are obtained.

### 5.5 Impulse response function calculations

Impulse response functions are determined by using the modal parameters of the coupled ground track model. As shown in Figure 5-14, there are  $N$  nodes on the rail and  $M$  nodes on the ground.  $N$  nodes on the rail represent the nodes where rail wheel contact forces are applied.  $M$  nodes on the ground represent the nodes where the ground motion is predicted. Impulse response function matrix is a matrix of  $3 \cdot M + N$  by  $N$  elements. The first index is for the response coordinates and the second index is for loading coordinates. As the rail wheel contact force is assumed to be only in the vertical direction,  $z$  direction, the loading coordinates include only the ones in  $z$  direction. As the response is predicted in all three directions, response coordinates on the ground include  $3 \cdot M$  coordinates.

Impulse response function of the vehicle model can be obtained from the modal parameters of the vehicle.  $V$  number of nodes will be present in the calculations as shown in Figure 5-15, and this number is the number of wheel sets of railway vehicle in the analysis.

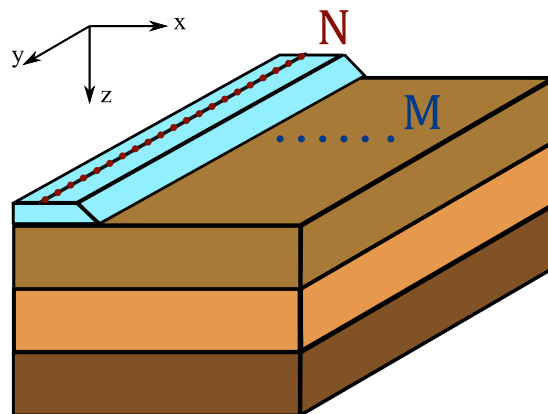


**Figure 5-14.** Response coordinates on coupled ground track model

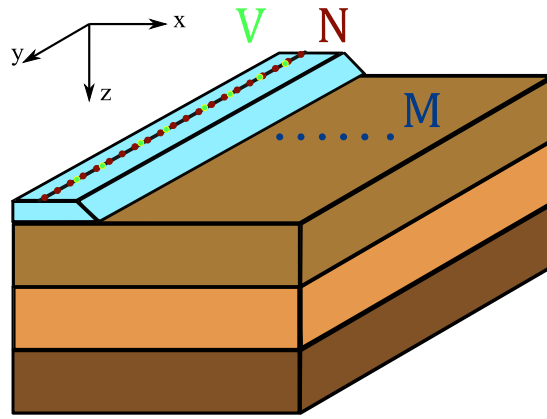


**Figure 5-15.** Coupled ground and track model with vehicle response nodes

At each time step in the analyses, responses of  $3 \cdot M + N + V$  degrees of freedom are calculated.

### 5.6 Response calculations

Response calculations are performed for a time array with  $t_{final} = 9$  seconds and time increment of  $\Delta t = 0.5$  ms. At each time step; first, wheel rail contact forces are calculated and then, responses of wheel and rail nodes are computed for this loading. After rail forces are calculated for the whole time interval, response of ground is calculated. Note that, depending on the train speed a larger or smaller value of  $t_{final}$  may be selected. Time step size is chosen to be two order smaller than period corresponding to the highest frequency of interest, typically 89 Hz.

In the calculation of wheel rail contact force, the first step is determining the position of each wheel on rail, at each time step. This is done by comparing the position of the wheel,  $y_w$ , with the position of nodes on rail,  $y_r$ .

$$y_w(t) = y_{w0} + v_t t \quad (223)$$

Here,  $y_{w0}$  is the initial position array of the wheels, and it depends on the train configuration. For typical high speed trains analyzed in this thesis, there are 26 wheel sets for a train length of 200 m. Initial position for the first wheel is 0 and it is -200 m for the last wheel as shown in Figure 5-16.

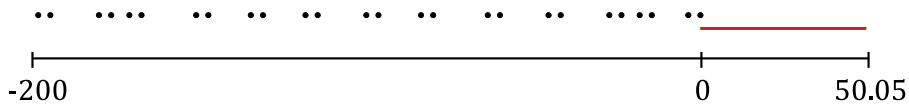


**Figure 5-16.** Initial positions of wheels

Positions of wheelsets at an arbitrary calculation step are shown in Figure 5-17.



**Figure 5-17.** Position of wheels at an arbitrary step of calculations

Positions of nodes on rail,  $y_r$ , comes from the finite element mesh. For a 50 m length of rail analyzed, there are approximately 500 to 600 rail nodes with a mesh size of 0.10 m. As train goes over the rail nodes analyzed; if  $y_w$  is between 0 and 50 m, then the closest rail node position  $y_r$  is determined as wheel position at this step.

After determining the wheel positions for each step, the response analysis for rail and wheels begins. At each time step, the displacement of each wheel on rail is compared with the displacement of the corresponding rail position. Wheel rail contact force is calculated by Equation (218), depending on this comparison. For this time step, the forces acting on wheel and rail are obtained as in Equations (221) and (222).

As the forces on the wheel and rail for this step are calculated, the responses of the wheel and rail nodes due to these loading are calculated by multiplying these force values with unit impulse response functions already calculated. Responses of wheel and rail nodes for the forces at this time step are added to wheel and rail response histories. This addition maintains the convolution of responses due to forcing history.

For the whole calculation time array, similar calculations are performed and responses of all wheels and rail nodes are obtained. As a result of this procedure, rail force histories are determined. Responses of nodes on ground surface are calculated by the convolution of these force histories and the corresponding impulse response functions. After vibration velocity response is calculated in time domain, frequency content of velocity response and vibration metrics, such as peak particle velocity, filtered weighted severity and root-mean-square velocity level can be also obtained. In filtered weighted severity and maximum filtered weighted severity calculations, a fourth order low pass digital Butterworth filter is applied in MATLAB.

## **5.7 Computational details**

The most time consuming operations in proposed calculation procedure are eigenvalue calculations. Computation times are directly dependent on matrix sizes. As matrix sizes increase, computation times increase. Increasing matrix size also requires large memory on computer, which may pose a limit on problem solution.

Computations are performed on a workstation with Intel Xeon E5-2687W 3.10 GHz processor and 64 GB ram. MATLAB and ANSYS are used as computation software.

Table 5-1 lists calculation procedure steps and computation times for these steps, for reference study presented in Chapter 7.

**Table 5-1.** Computation times for steps in reference study

Step	Time (hours)
Layer 1 eigenvalue analysis	8.6
Layer 3 eigenvalue analysis	1.9
Ground coupling	2.8
Ground fixing	1.1
ANSYS modal analysis	0.2
ANSYS results writing	0.5
Track ground coupling	4.7
Rail impulse response function calculation	0.7
Response calculations	0.3

First step of computations is the eigenvalue analysis for first ground layer and this is the step with most computation time consumed. Matrix size for this layer is 74070 by 74070, as finite difference mesh size of 0.65 m is applied. For this layer modal parameters up to 100 Hz are obtained. In reference analysis, second ground layer has the same height with first ground layer, thus these two layers have exactly the same geometry. These two layers have similar material properties except Young's modulus. As introduced in Section 3.11, modal parameters of second layer can be obtained from the modal parameters of first layer. As third ground layer has different height, a new eigenvalue analysis is performed for this layer. Young's modulus for this layer is much higher than first layer; therefore it has much higher eigenvalues. For the second and third ground layers, modal parameters are calculated for frequencies up to 110 Hz. Mesh sizes for the second and third layers are 0.65 m, similar to the first layer. Considering the specified frequency range, a shorter computation time is required to obtain corresponding modal parameters of third layer. In ground coupling step and ground fixing steps, modal parameters are calculated for frequencies up to 90 Hz and 89 Hz, respectively.

For track modal parameter calculation, undamped modal analysis is performed in ANSYS. Time required for saving results of this analysis is much higher than time elapsed during analysis.

In parametric analysis, for the cases without any modification on ground and track models, only response calculation time step is followed. These cases are vehicle type, vehicle speed and rail unevenness cases.

For parametric analysis cases where there is modification on track but no modification on ground model, calculation steps starting with ANSYS modal analysis are performed. Depending on modified track model, there may be change in time required for each step.

In the cases with modification on ground model, if possible, modal parameter calculation procedure for proportional material properties is implemented. If this procedure is not applicable, eigenvalue analysis from finite difference formulation is performed with possible change in time requirement. As ground modal parameters are obtained, calculation steps starting from track ground coupling are followed.



## CHAPTER 6

### VALIDATION OF PREDICTION MODEL

In this chapter, the numerical model presented in previous chapters is validated on different high speed lines with measurements available in literature. Predicted vibration levels are compared with measured levels to validate that the outputs of the numerical model. In the comparisons; vibration levels are compared in time and frequency domains, and results of vibration level descriptors such as *PPV*, *KB<sub>F,max</sub>* and *VdB* are also analyzed. It should be noted that in the numerical model validation, comparison of levels and descriptors is used by previous researchers [26], [50], [51].

#### 6.1 Thalys high speed train at Leuze-en-Hainaut, 2012

##### 6.1.1 Ground, track and vehicle parameters

Connolly and Kouroussis performed vibration measurements on high speed line between Brussels and Paris [52]. The measurement location is Leuze-en-Hainaut and three different sites are selected: at grade, embankment and cutting. Sample records of these measurements were made available online. In this section, vibration predictions are compared with the record of Thalys high speed train running on at grade railway track.

Soil properties for Leuze-en-Hainaut are given with wave speeds in [51]. These wave speed values and a three layer approximation for soil properties are presented in Table 6-1. Ballasted track properties are listed in Table 6-2 and Table 6-3. Rayleigh damping is applied in both ground and track modeling. Proportional

damping ratio is taken as 0.0004 s for the track model. The vehicle configuration for Thalys high speed train is given Figure 6-1. The vehicle speed is 299 km/h. There are three types of cars on the train: two traction cars, two side cars and six central cars. Parameters for these car types are given in Table 6-4.

**Table 6-1.** Soil properties for Leuze-en-Hainaut 2012 [51]

	Original soil profile			Three layer approximation				
	Thickness (m)	S-wave speed (m/s)	P-wave speed (m/s)	Thickness (m)	Young's modulus (MPa)	Poisson's ratio	Density (kg/m <sup>3</sup> )	Damping ratio (s)
Layer 1	1.3	142	280	3.8	115	0.3	2000	0.0004
	1.3	162	280					
	1.2	157	280					
Layer 2	1.8	280	520	5.2	450	0.3	2000	0.0004
	3.4	330	520					
Layer 3	half space	598	940	6.0	1200	0.3	2000	0.0004

**Table 6-2.** Ballasted track parameters [33]

Rail	Area	76.70 cm <sup>2</sup>
	Inertia	3038.3 cm <sup>4</sup>
Rail pad	Stiffness	120·10 <sup>6</sup> N/m
	Damping	4·10 <sup>3</sup> Ns/m
	Thickness	10 mm
Sleeper	Height	0.205 m
	Width	2.500 m
	Length	0.285 m
	Spacing	0.600 m
Ballast	Height	0.300 m
	Top width	3.120 m
	Bottom width	4.120 m
Subballast	Height	0.200 m
	Top width	4.120 m
	Bottom width	4.920 m
Subgrade	Height	0.500 m
	Top width	4.920 m
	Bottom width	6.620 m

**Table 6-3.** Ballasted track mechanical properties [33]

	Young's modulus (MPa)	Poisson's ratio	Density (kg/m <sup>3</sup> )
Rail	210000	0.25	7900
Sleepers	30000	0.40	2054
Ballast	100	0.35	1800
Subballast	300	0.35	2200
Subgrade	127	0.35	2100

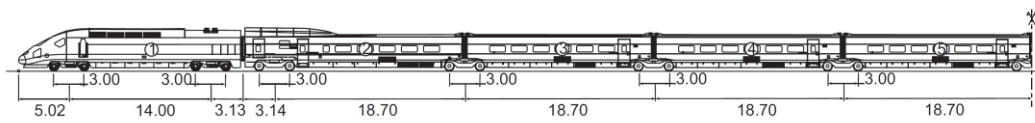


**Figure 6-1.** Thalys HST configuration [26]

**Table 6-4.** Vehicle parameters for Thalys HST [45]

	$m_c$ (kg)	$m_b$ (kg)	$m_w$ (kg)	$k_1$ (MN/m)	$c_1$ (kNs/m)	$k_2$ (MN/m)	$c_2$ (kNs/m)
Traction cars	53442	3261	2009	2.09	40	2.45	40
Side cars	34676	8156	2009	2.09	40	2.45	40
Central cars	28500	1400	2050	1.63	40	0.93	40

### 6.1.2 Prediction model validation

Figure 6-2 and Figure 6-3 show the vertical vibration time histories for measurements and predictions by developed model. For both vibration response at 9 m and 11 m, timing and shape are simulated accurately. Predicted levels show the bogie passage more clearly. For the response at 11 m from the track, velocity levels for central cars are slightly underestimated. There are overestimations for the response after the passage of the end traction car for both histories.

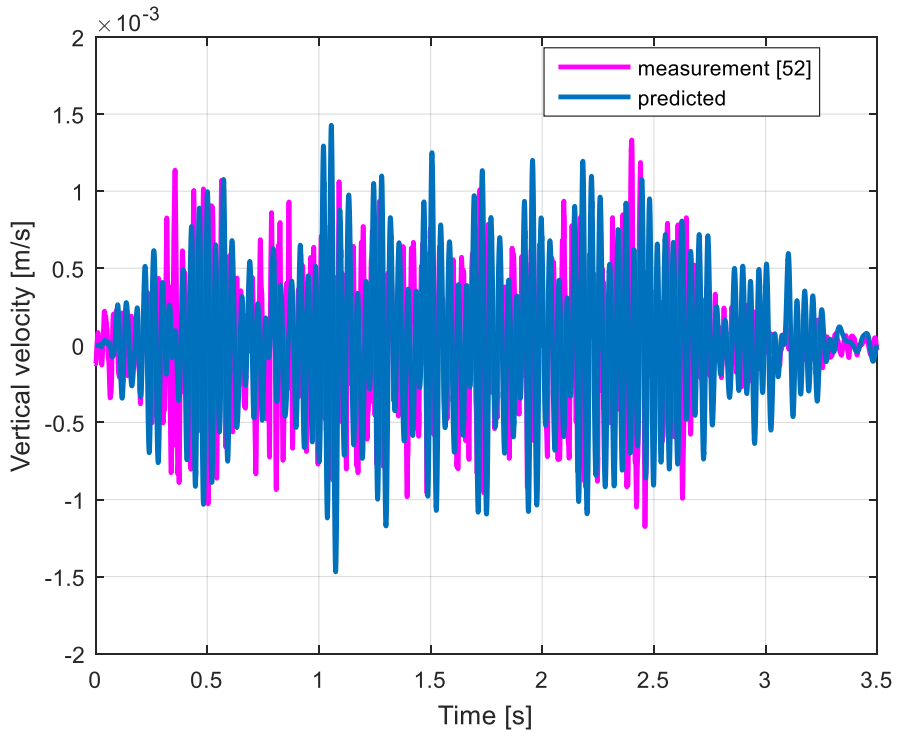


**Figure 6-2.** Vertical velocity time history 9 m from track center

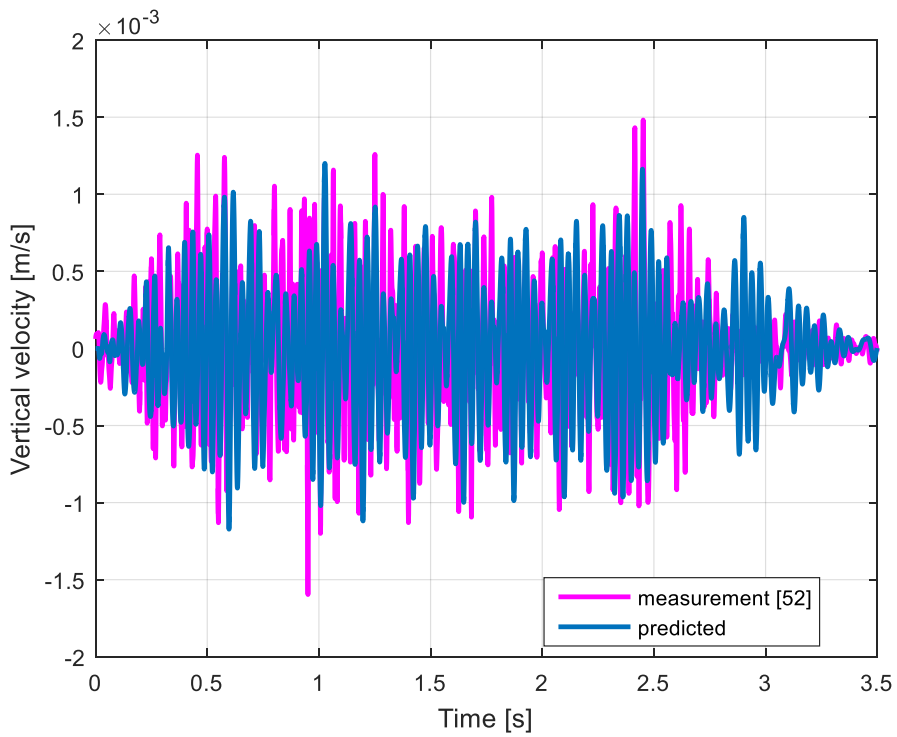


**Figure 6-3.** Vertical velocity time history 11 m from track center

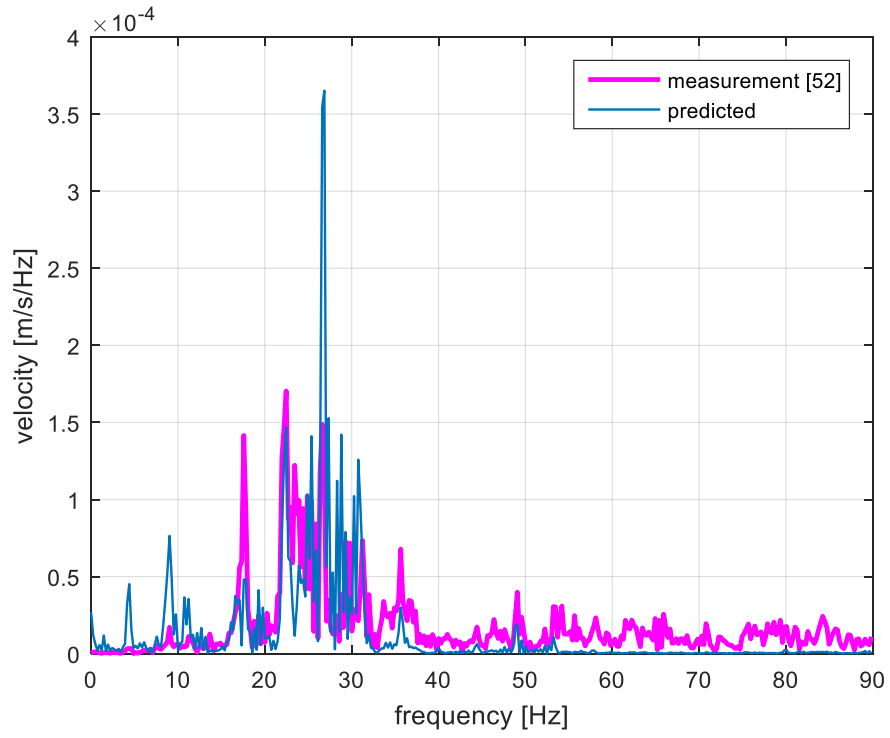


**Figure 6-4.** Vertical velocity frequency content at 9 m from track center

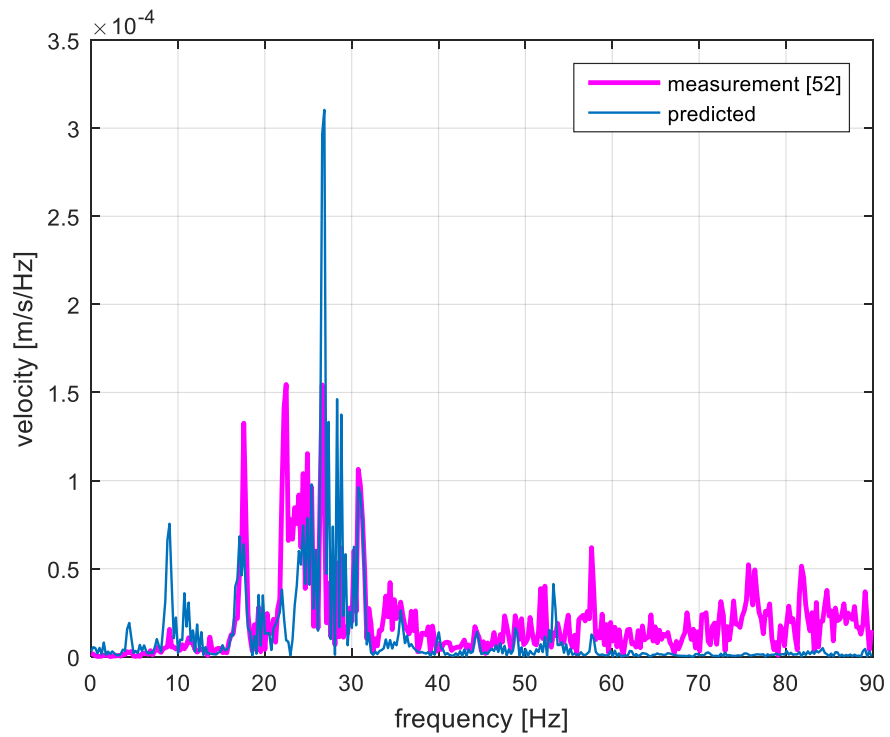


**Figure 6-5.** Vertical frequency content at 11 m from track center

Comparisons for frequency content of the response are shown in Figure 6-4 and Figure 6-5. It can be concluded that for the two comparison locations, the presented numerical model predicted the frequency contents accurately. For both measurements and predictions, response is higher in the frequency range between 15 and 35 Hz. Predictions also identified several peaks outside this range.

In Figure 6-6, vertical velocity  $VdB$  levels are compared for different positions where measurements are available. It is seen that the numerical model predicted  $VdB$  levels accurately. The predictions are in a range of 2.5  $dB$  of the measured levels. Figure 6-7 and Figure 6-8 show the  $VdB$  level comparisons for longitudinal and horizontal directions, respectively. For both directions, velocity levels are predicted with a maximum difference of 4.0  $dB$ . Root-mean-square vibration velocity distributions are shown in Figure 6-9, Figure 6-10 and Figure 6-11.

It is shown that, time domain and frequency domain responses as well as the  $VdB$  levels are simulated accurately by the numerical prediction model.

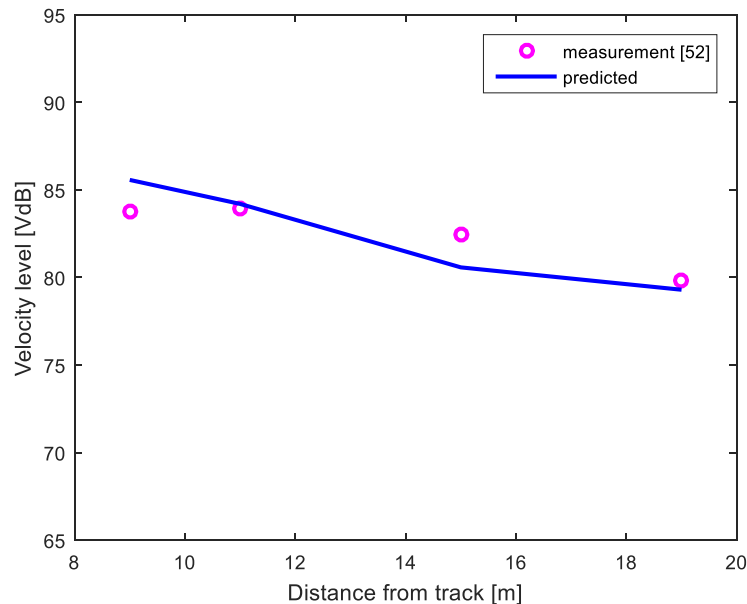


**Figure 6-6.** Vertical velocity  $VdB$  variation with distance from track center

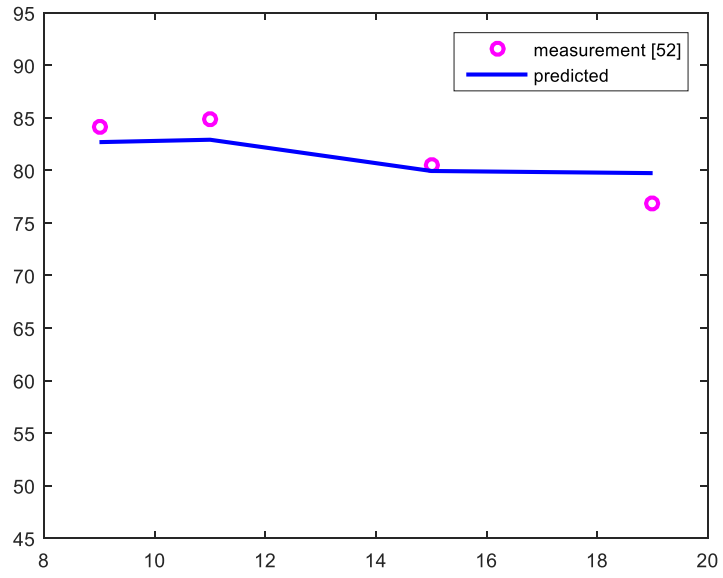


**Figure 6-7.** Longitudinal velocity VdB variation with distance from track center

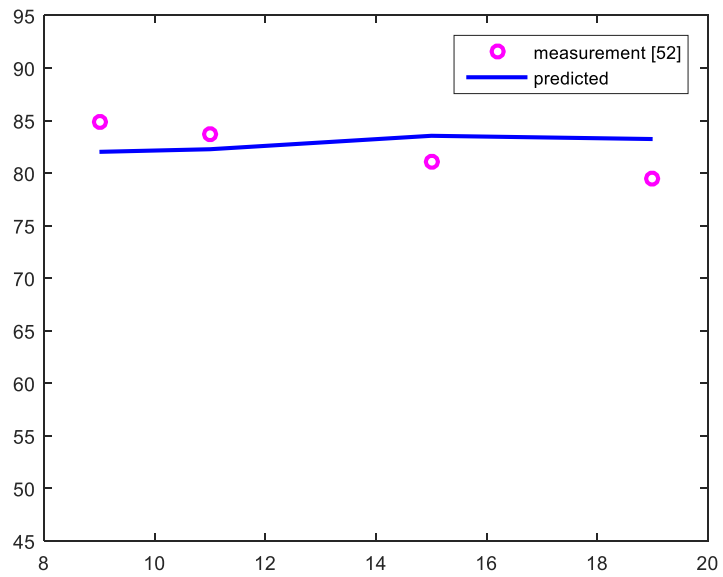


**Figure 6-8.** Horizontal velocity VdB variation with distance from track center

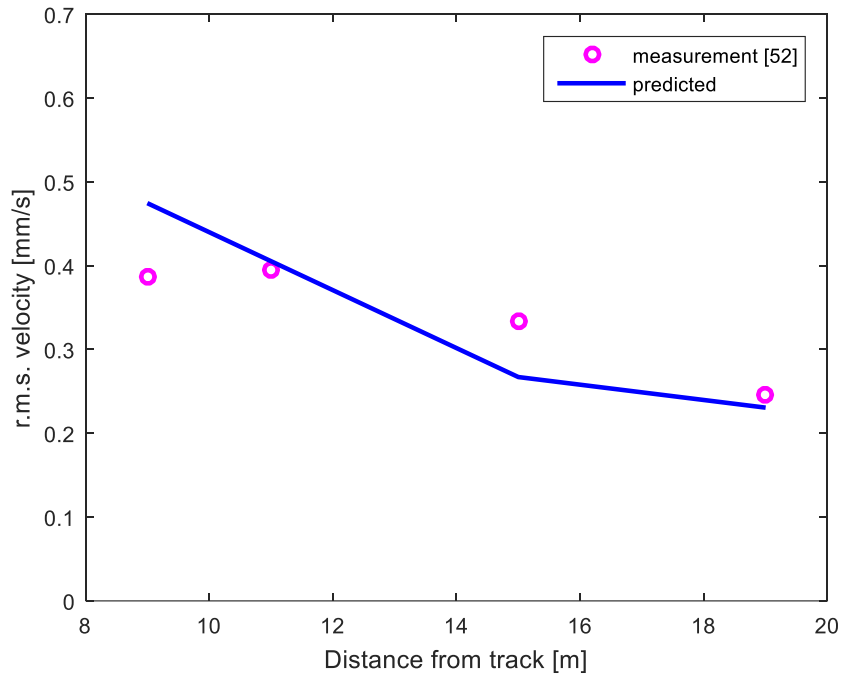


**Figure 6-9.** Vertical velocity (r.m.s.) variation with distance from track center

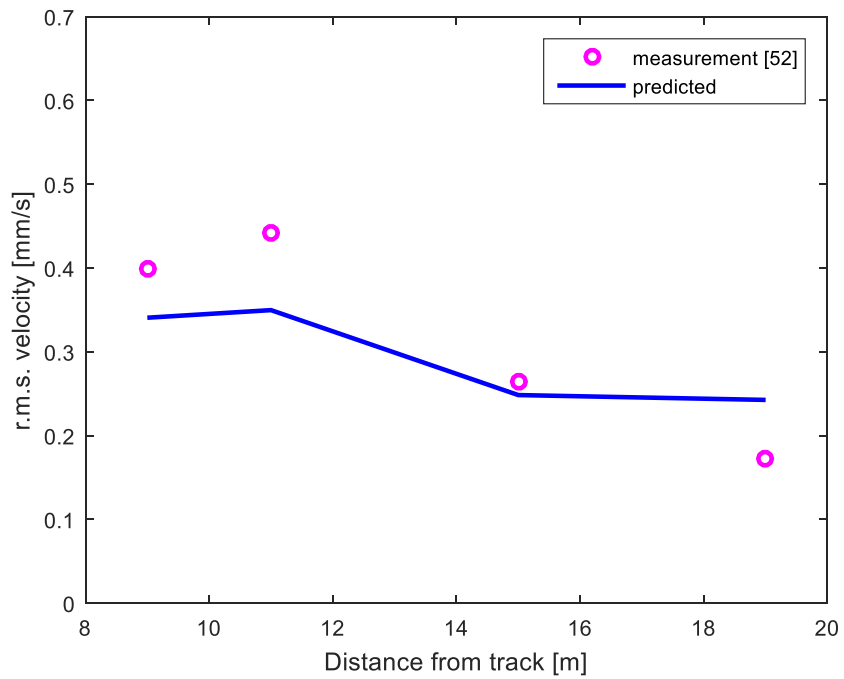


**Figure 6-10.** Longitudinal velocity (r.m.s.) variation with distance from track center

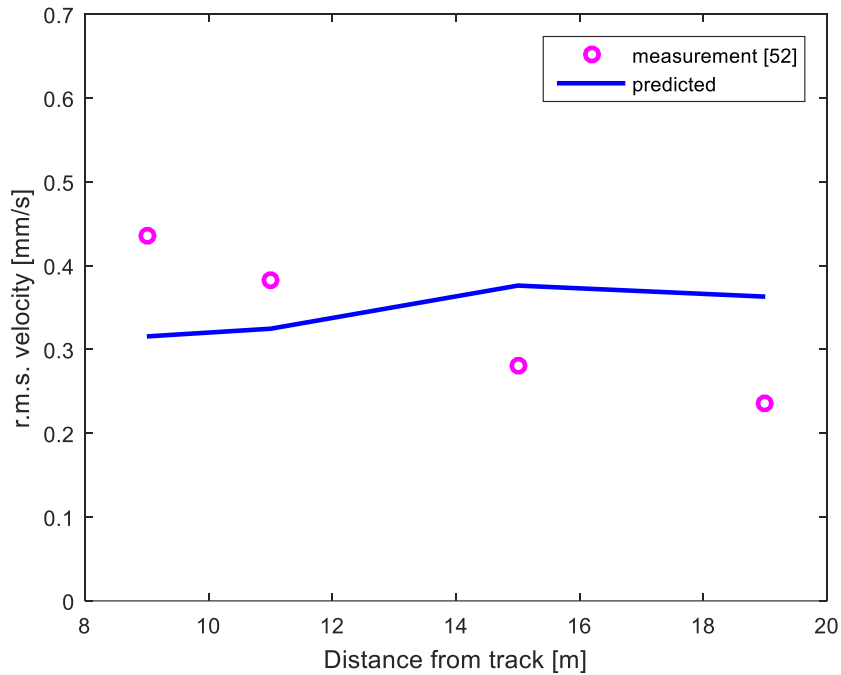


**Figure 6-11.** Horizontal velocity (r.m.s.) variation with distance from track center

## 6.2 Thalys high speed train at Mévergnies, 2005

### 6.2.1 Ground, track and vehicle parameters

Kouroussis reported ground vibration records near high speed line between Brussels and Paris at Mévergnies in 2005 [53]. A detailed analysis of these measurements and comparison with a numerical prediction model is presented in [26]. In this section, vibration predictions are compared with the presented results in [26].

Material properties for ground layers at Mévergnies are given in [26]. There are two ground layers on a half space and therefore a three layer approximation is modeled in this study. In Table 6-5, material properties of three layer ground are presented. Ballasted track properties are the same as in Table 6-2 and Table 6-3.

Rayleigh damping is applied in both ground and track modeling. Rayleigh damping ratio is taken as 0.0004 s for the track model. The vehicle configuration and parameters for Thalys high speed train was already given Figure 6-1 and Table 6-4. A very good track unevenness profile, class 6 [3], is used in the analyses.

**Table 6-5.** Soil properties for Mévergnies 2005 [26]

	Original soil profile			Three layer approximation				
	Thickness (m)	S-wave speed (m/s)	P-wave speed (m/s)	Thickness (m)	Young's modulus (MPa)	Poisson's ratio	Density (kg/m <sup>3</sup> )	Damping ratio (s)
Layer 1	2.7	177	330	2.7	129	0.3	1600	0.0004
Layer 2	3.9	209	391	3.9	227	0.3	2000	0.0004
Layer 3	half space	356	666	8.4	659	0.3	2000	0.0004

## 6.2.2 Prediction model validation

In Figure 6-12 to Figure 6-19, predicted vibration velocity levels are compared with measurement results presented in [26]. The speed of the Thalys high speed train is 300 km/h for all presented results, except comparisons in Figure 6-18 and Figure 6-19, for which the speed is 285 km/h.

In Figure 6-12 and Figure 6-13, time history of vertical velocity at 7 m and 15 m from the track are compared with measurements. The timing and shape predicted level is similar to measurement at 7 m. For prediction at 15 m, although the timing of response is observed, amplitude is relatively underestimated. The responses for traction cars are observed much clear for 7 m response.

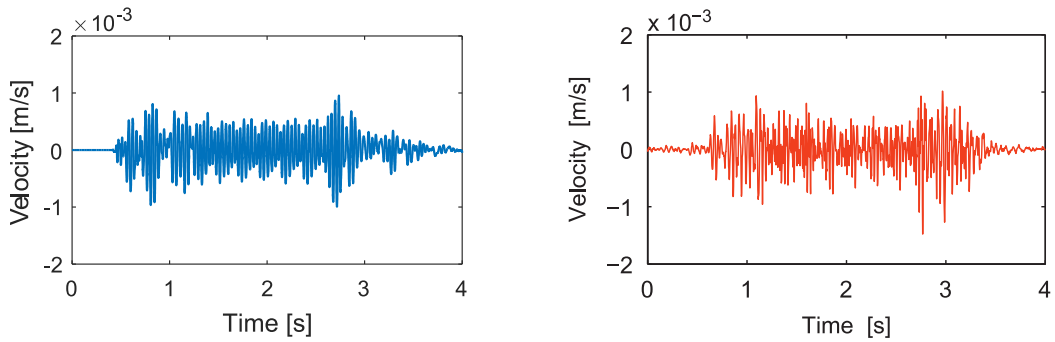


**Figure 6-12.** Vertical velocity time history 7 m from track center, left: predicted, right: measurement [26]

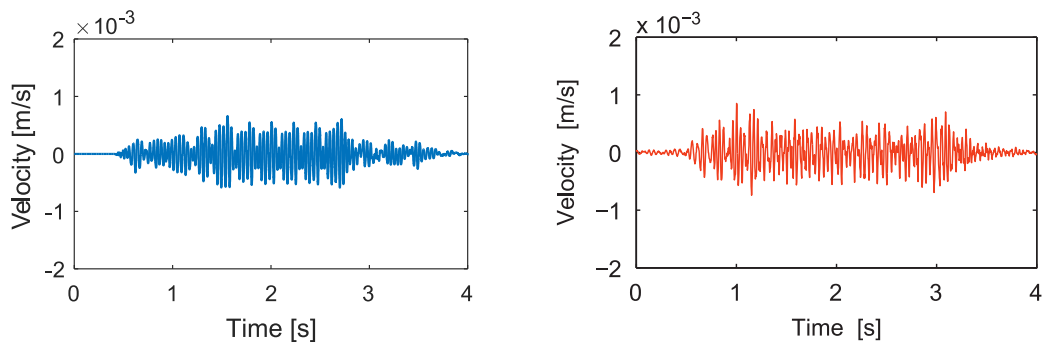


**Figure 6-13.** Vertical velocity time history 15 m from track center, left: predicted, right: measurement [26]

Comparison for vibration velocity weighted severity ( $KB_F$ ) is shown in Figure 6-14 and Figure 6-15. For both 7 m and 15 m response, the level and timing of the weighted severities are identified by predictions, except the responses at 15 m caused by the traction cars.

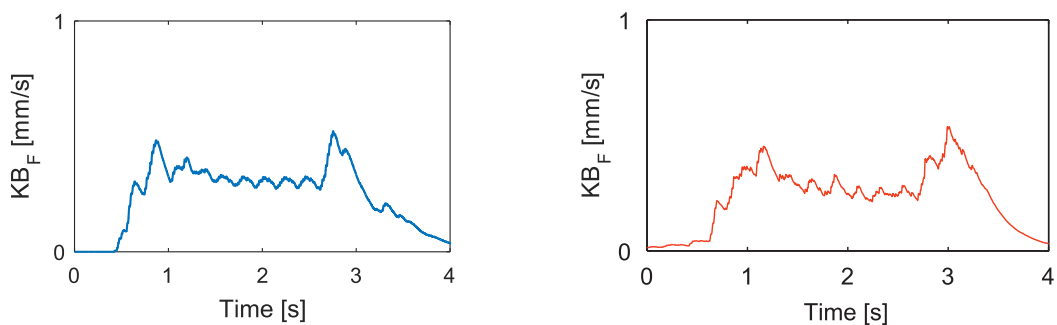


**Figure 6-14.** Weighted severity ( $KB_F$ ) of vertical ground vibration 7 m from track center, left: predicted, right: measurement [26]

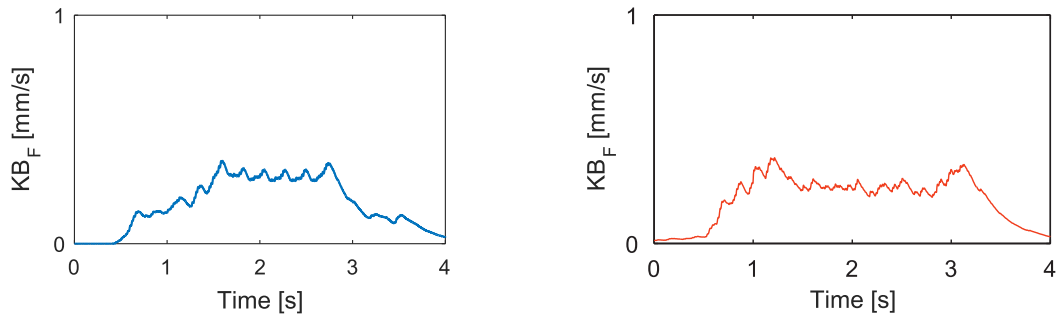


**Figure 6-15.** Weighted severity ( $KB_F$ ) of vertical ground vibration 15 m from track center, left: predicted, right: measurement [26]

Frequency content of vibration velocity prediction is compared in Figure 6-16 and Figure 6-17. As frequency range of prediction model is set as 0 to 89 Hz, vibration contents higher than 89 Hz are already expected to vanish. The dominant frequency range in the predicted vibration levels is between 16 to 32 Hz. This range is dominant in the measurement results as well. For measurement at 7 m, there is a second range observed range between 50 to 65 Hz, and in the predicted frequency content, vibration levels in this range are also identified.

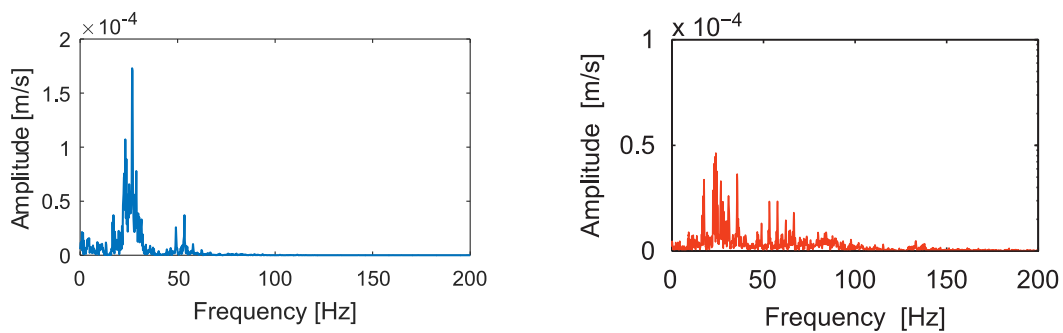


**Figure 6-16.** Vertical velocity frequency content at 7 m from track center, left: predicted, right: measurement [26]

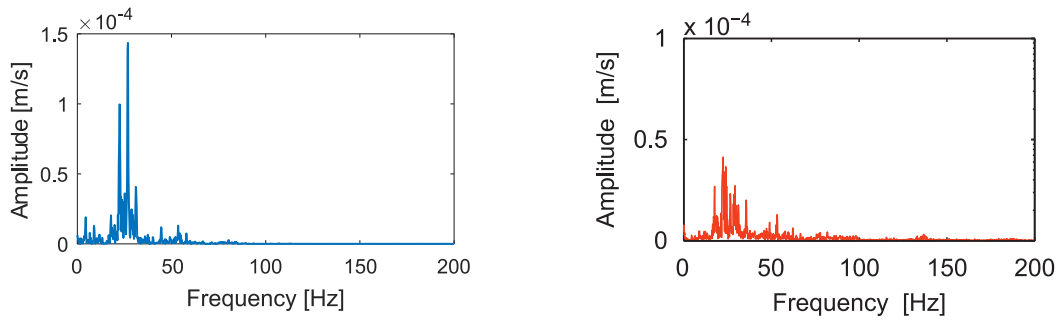


**Figure 6-17.** Vertical velocity frequency content at 15 m from track center, left: predicted, right: measurement [26]

The distribution of peak particle velocity and maximum weighted severity with distance from track are compared in Figure 6-18 and Figure 6-19. For peak particle velocity, the decreasing behavior with distance is observed in predicted levels; a good agreement is obtained in the far field and a slight underestimation is present for near field. In predicted levels of maximum weighted severity; the decreasing behavior with distance is observed similarly, however the values are slightly overestimated.

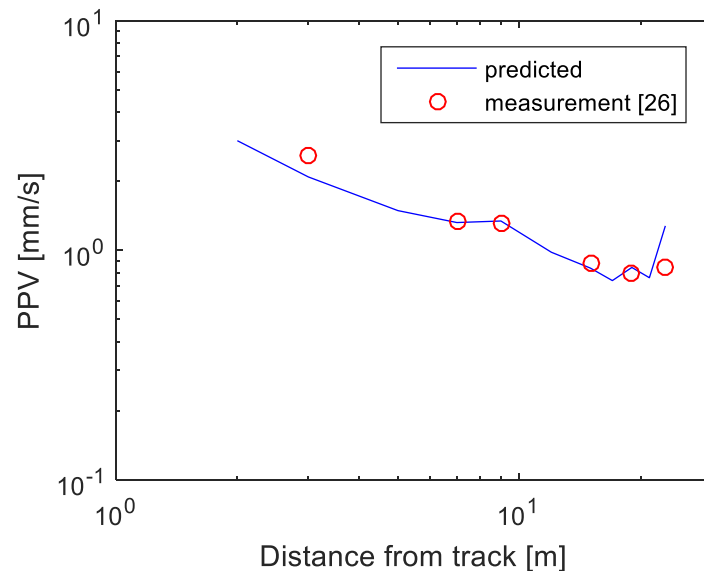


**Figure 6-18.** Peak particle velocity (PPV) variation with distance from track center

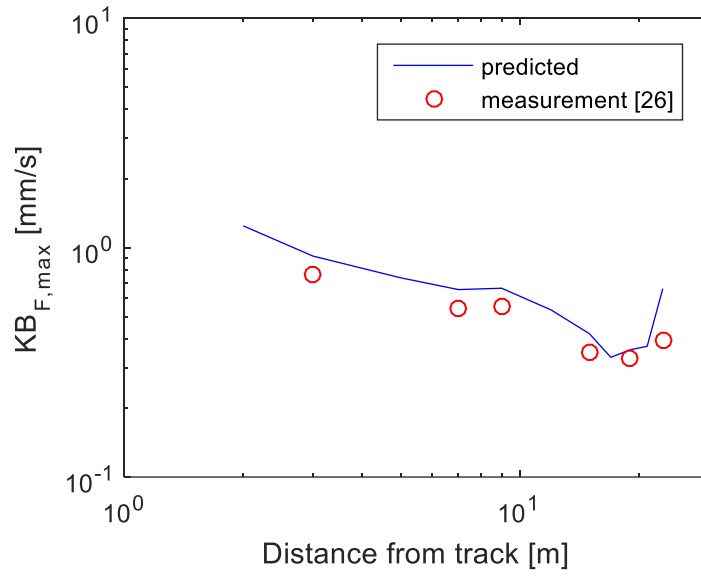


**Figure 6-19.** Maximum weighted severity ( $KB_{F,max}$ ) variation with distance from track center

## CHAPTER 7

### PARAMETRIC STUDY FOR GROUND VIBRATION

In this chapter, a detailed parametric study for the effects of vehicle, track and ground parameters on ground vibration is presented. A reference set of parameters is first selected and listed. To study the effect of a parameter, only that parameter is varied while the remaining is set unchanged. Peak particle velocity ( $PPV$ ) and maximum weighted severity level ( $KB_{F,max}$ ) will be used as vibration indicators in the analyses. The distributions of  $PPV$  and  $KB_{F,max}$  values at distances between 5 to 21 m from track center are calculated, in order to analyze ground vibration levels at near, mid and far fields.

#### 7.1 Reference parameters

The vehicle selected as reference vehicle for this parametric study is Thalys high speed train. Configuration and parameters for this train are already given in Figure 6-1 and in Table 6-4. Reference vehicle speed is set as 100 km/h.

A ballasted railway track is used in the reference study. Properties of reference track are given in Table 7-1 and Table 7-2. An average track unevenness profile, class 3 [3], is used in the analyses.

A three layer ground model is taken for reference study. Parameters for this ground model are given in Table 7-3. Proportional Rayleigh damping is used as ground damping model.

**Table 7-1.** Reference ballasted railway track mechanical properties

	Young's modulus (MPa)	Poisson's ratio	Density (kg/m <sup>3</sup> )
Rail	210000	0.25	7900
Sleepers	30000	0.4	2600
Ballast	80	0.35	2000
Subballast	200	0.35	2000
Subgrade	120	0.35	2000

**Table 7-2.** Reference ballasted railway track properties

Rail	Area	76.70 cm <sup>2</sup>
	Inertia	3038.3 cm <sup>4</sup>
Rail pad	Stiffness	90 · 10 <sup>6</sup> N/m
	Damping	30 · 10 <sup>3</sup> Ns/m
	Thickness	10 mm
Sleeper	Height	0.200 m
	Width	2.400 m
	Length	0.240 m
	Spacing	0.650 m
Ballast	Height	0.300 m
	Top width	3.000 m
	Bottom width	3.960 m
Subballast	Height	0.300 m
	Top width	3.960 m
	Bottom width	4.920 m
Subgrade	Height	0.400 m
	Top width	4.920 m
	Bottom width	6.200 m

**Table 7-3.** Soil properties for reference study

	Thickness (m)	Young's modulus (MPa)	Poisson's ratio	Density (kg/m <sup>3</sup> )	Damping ratio (s)
Layer 1	3.0	150	0.3	2000	0.0004
Layer 2	3.0	300	0.3	2000	0.0004
Layer 3	4.0	1000	0.3	2000	0.0004

The distribution of  $PPV$  and  $KB_{F,max}$  values with distance from track center for the reference case are shown in Figure 7-1 and Figure 7-2.

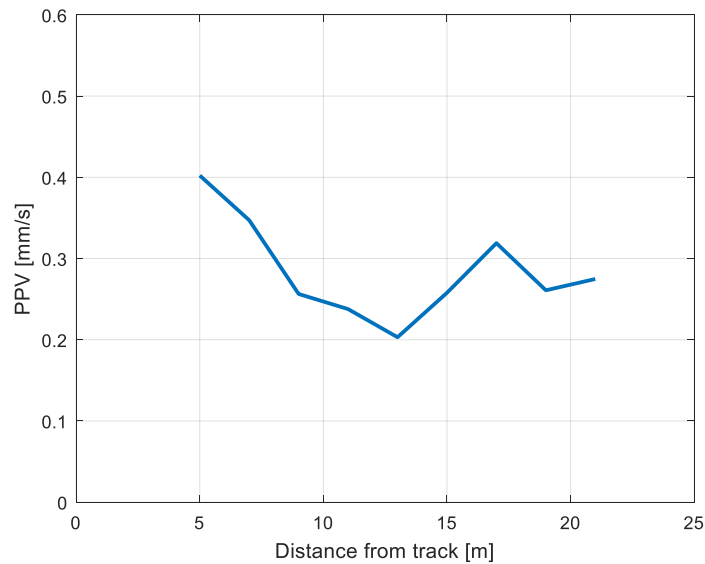


**Figure 7-1.** Vertical peak particle velocity (PPV) variation with distance from track center

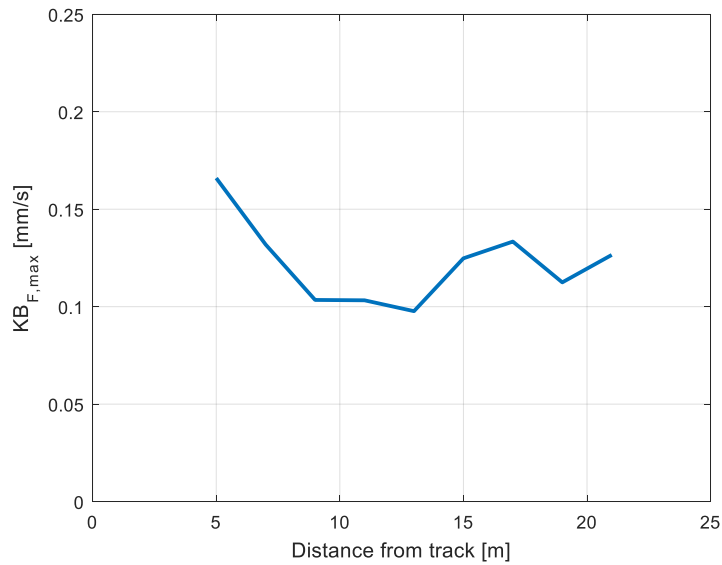


**Figure 7-2.** Maximum weighted severity ( $KB_{F,max}$ ) variation for vertical velocity with distance from track center

## 7.2 Effects of vehicle parameters on ground vibration

In this section, effects of two parameters are analyzed: train type and train speed. First, vibrations caused by the traffic of different train types are compared. Then, trains running with different speeds are analyzed for vibration levels.

### 7.2.1 Train type

There are several types of railway vehicles depending on their functions and applications. Most common function is to carry passengers. Trams are used in urban areas to transport people. Similarly, there are intercity trains to transport people between nearby cities. Recently developed, high speed trains are carrying people between highly populated metropolitans. There are also underground trains for the use of urban transport. Another function of railway vehicles is to move heavy loads and the type of trains with this function is called freight trains.

In this section, four different train types will be compared with Thalys high speed train type which is selected as reference train type. As it can be seen in following figures and tables, train types analyzed are: tram, intercity train, longer high speed train and freight train, while the reference train type is a high speed train [45], [54].

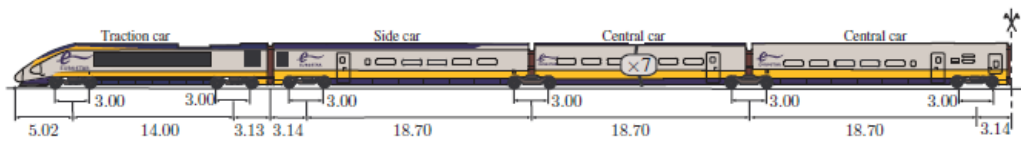


**Figure 7-3.** Configuration for Eurostar high speed train [45]

**Table 7-4.** Parameters for Eurostar high speed train [45]

	$m_c$ (kg)	$m_b$ (kg)	$m_w$ (kg)	$k_1$ (MN/m)	$c_1$ (kNs/m)	$k_2$ (MN/m)	$c_2$ (kNs/m)
Traction cars	54166	3075	2046	2.63	12	3.26	90
Side cars	33854	9440	2046	2.2	12	0.91	2
Central cars	27083	2360	2046	2.07	12	0.61	4

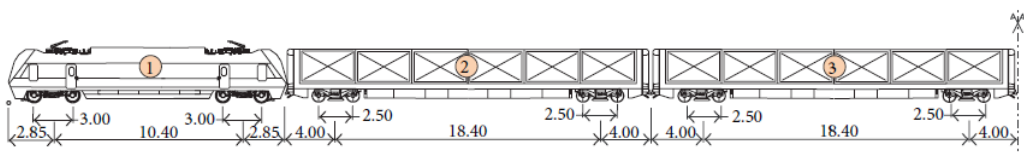


**Figure 7-4.** Configuration for freight train [54]

**Table 7-5.** Parameters for freight train [54]

$m_c$ (kg)	$m_b$ (kg)	$m_w$ (kg)	$k_1$ (MN/m)	$c_1$ (kNs/m)	$k_2$ (MN/m)	$c_2$ (kNs/m)
70000	1600	1400	22.8	2.33	4	60



higher than the applicable range of velocity for some train types analyzed such as tram and freight train.

$KB_{F,max}$  and  $PPV$  variations with distance from track center are given for five different train types in Figure 7-7 and Figure 7-8. It is observed that ground vibration levels are higher at near field than mid and far field locations, except an increase at 17 m, for all train types. Largest response magnitudes are obtained for freight train traffic. For reference high speed train (Thalys) and longer high speed train (Eurostar) traffic, ground vibration levels are almost the same. Response levels for intercity train traffic are predicted to be lower than for high speed traffic and higher than tram traffic.

An observation can be made that ground vibration levels are higher for heavier trains. Vibration metrics can be defined for comparison of different train types by dividing  $KB_{F,max}$  and  $PPV$  values by the axle load value. Total weight, number of axles and average axle loads of train types analyzed are listed in Table 7-8 [45], [54].

**Table 7-8.** Axle loads for train types [45], [54]

	Weight (kN)	Number of axles	Average axle load (kN)
Freight	4638	24	193.3
Thalys	4309	26	165.7
Eurostar	7664	48	159.7
ICE	4115	32	128.6
Tram	271	6	45.1

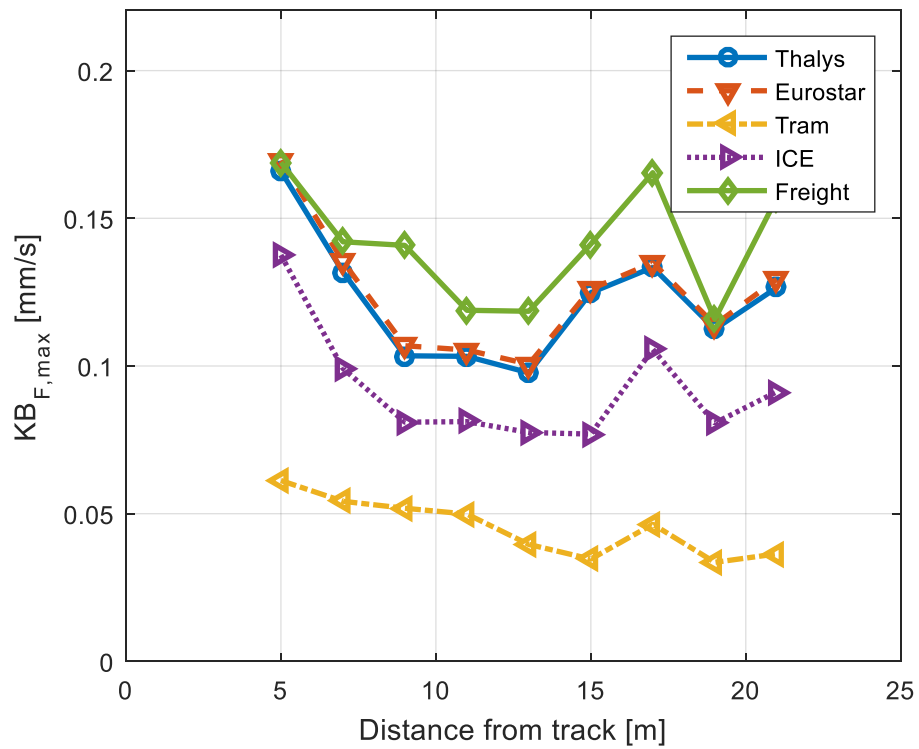


**Figure 7-7.**  $KB_{F,max}$  variation with distance for different train types

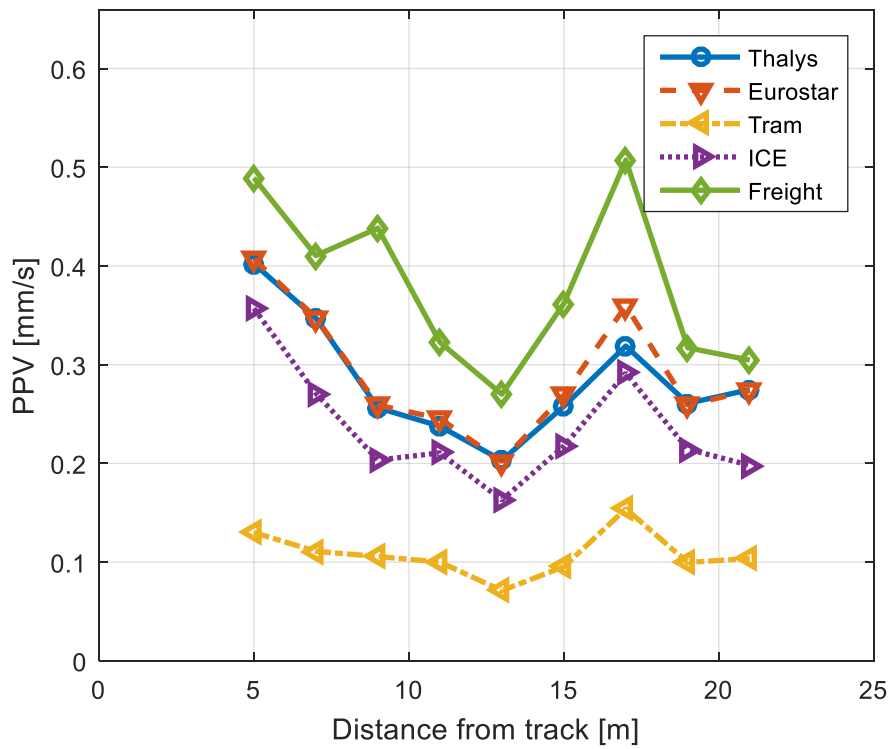


**Figure 7-8.** PPV variation with distance for different train types

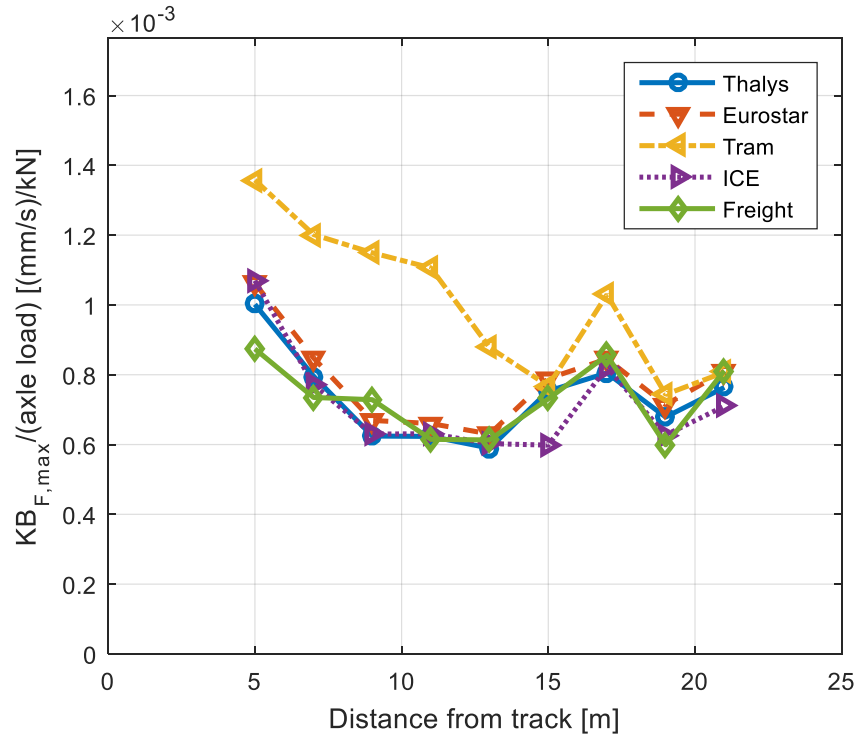


**Figure 7-9.**  $KB_{F,max}$  variation with distance for different train types considering axle loads

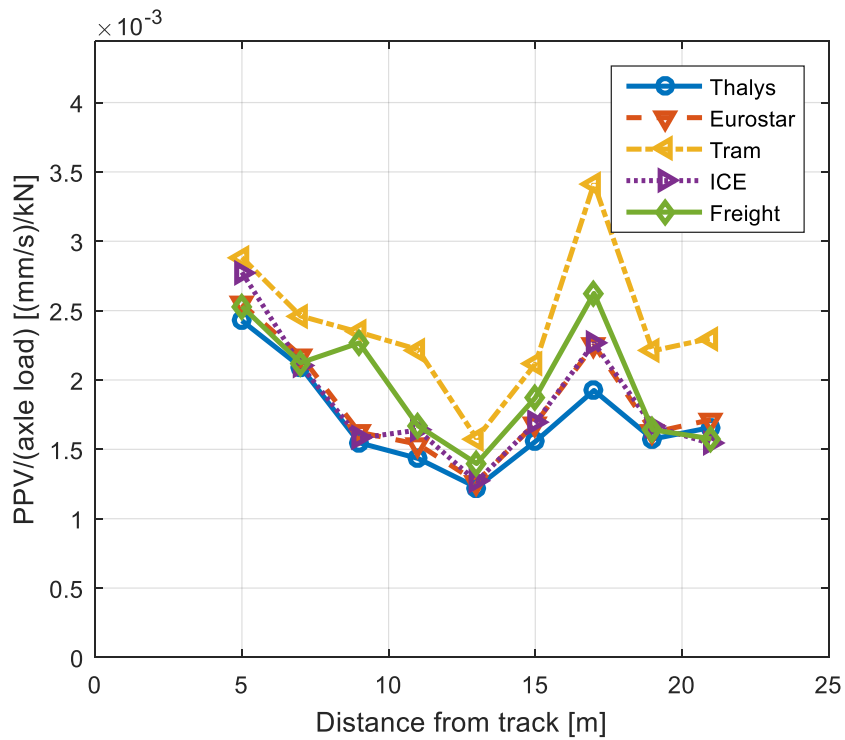


**Figure 7-10.** PPV variation with distance for different train types considering axle loads

Ground vibration levels when average axle loads are considered are given in Figure 7-9 and Figure 7-10. It is seen that magnitudes for  $PPV$  variation are similar for all train types. For  $KB_{F,max}$  variation, a similar conclusion can be made although a diversion is observed for near and mid field points on tram results.

### 7.2.2 Train speed

In this section, ground vibration levels will be compared for different train speeds. The range of train speed is selected in between 50-250 km/h in the analyses, while the reference speed is selected as 100 km/h. Figure 7-11 and Figure 7-12 shows ground vibration levels for five different train speeds. As it can be observed from these figures, ground velocity levels increase with increasing train speed. Generally, near field response is higher than far field response; however, for the 200 km/h case, far field responses are comparable with or higher than near field responses.

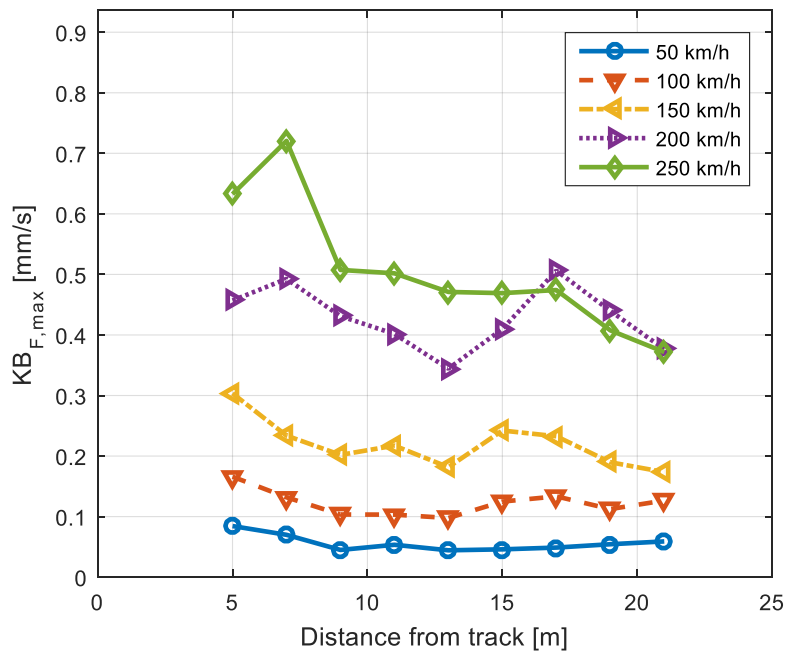
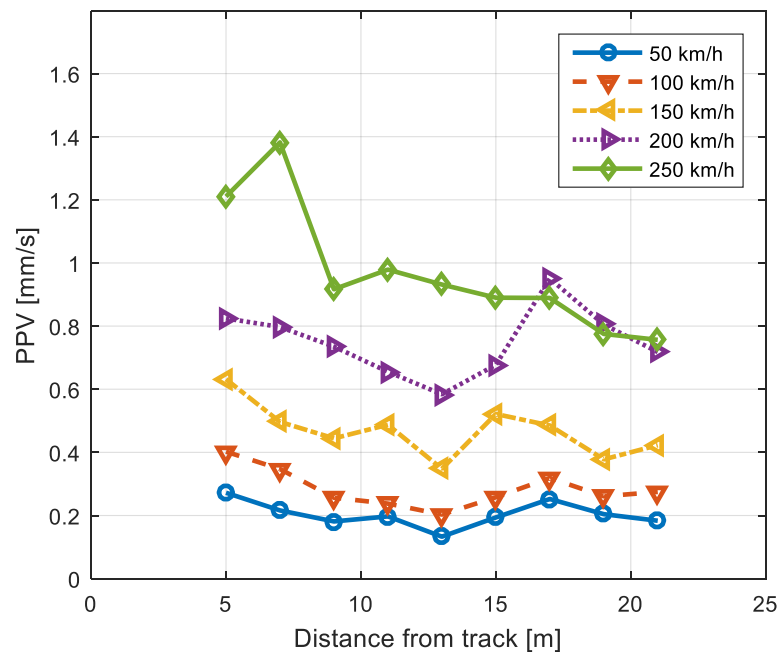


Figure 7-11.  $KB_{F,max}$  variation with distance for different train speeds



**Figure 7-12.** PPV variation with distance for different train speeds

### 7.3 Effects of track parameters on ground vibration

In this section; first, five elements of railway track are analyzed for their effect on ground vibrations. Studied track elements are rail unevenness, rail profile, rail pad stiffness, sleeper spacing and stiffness of ballast, subballast and subgrade materials. Finally, application of embankment layer is introduced and embankment material stiffness is analyzed for its effect on ground velocity levels.

#### 7.3.1 Rail unevenness

The effect of three different classes of rail unevenness on ground vibration response is compared in this section [3]. Average rail unevenness class (class 3) is the class used in reference study. Other classes used in the analyses are the poorest unevenness class (class 1) and the best unevenness class (class 6). Random rail profiles are obtained corresponding to these classes are shown in Figure 7-13.

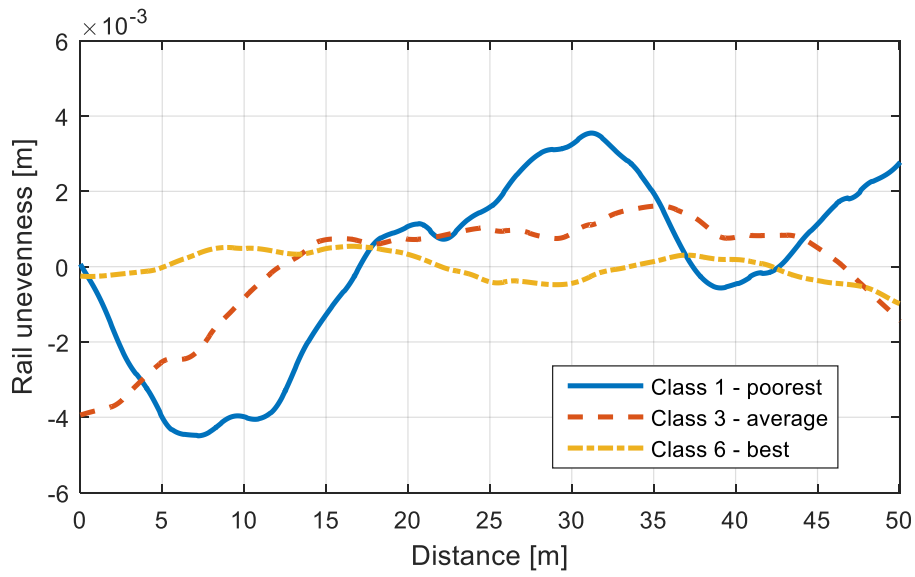


**Figure 7-13.** Rail profiles for different unevenness classes

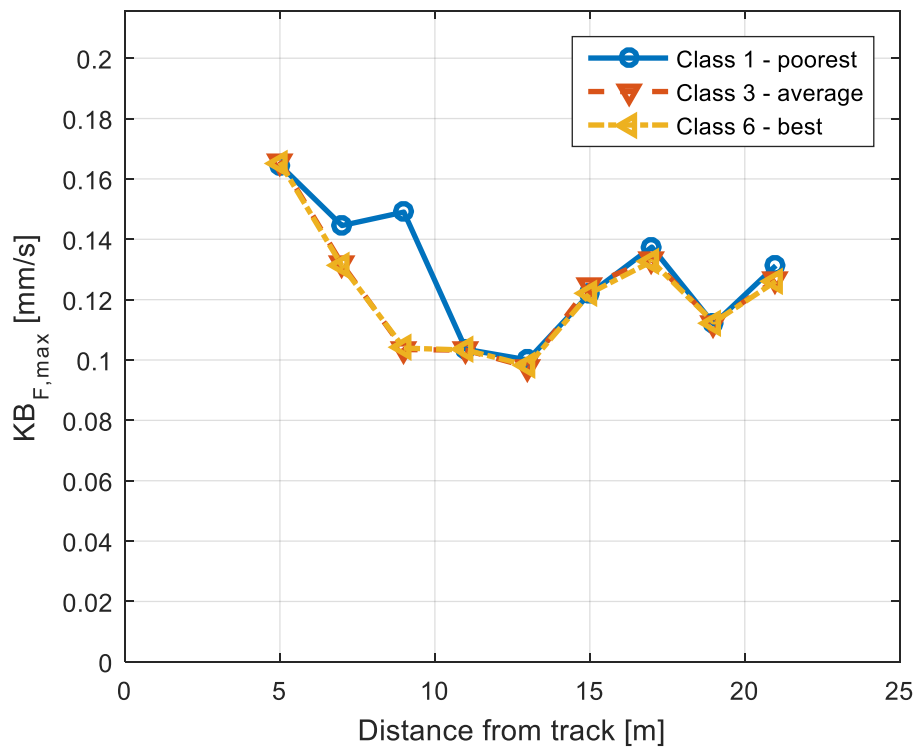


**Figure 7-14.**  $KB_{F,max}$  variation with distance for different unevenness classes

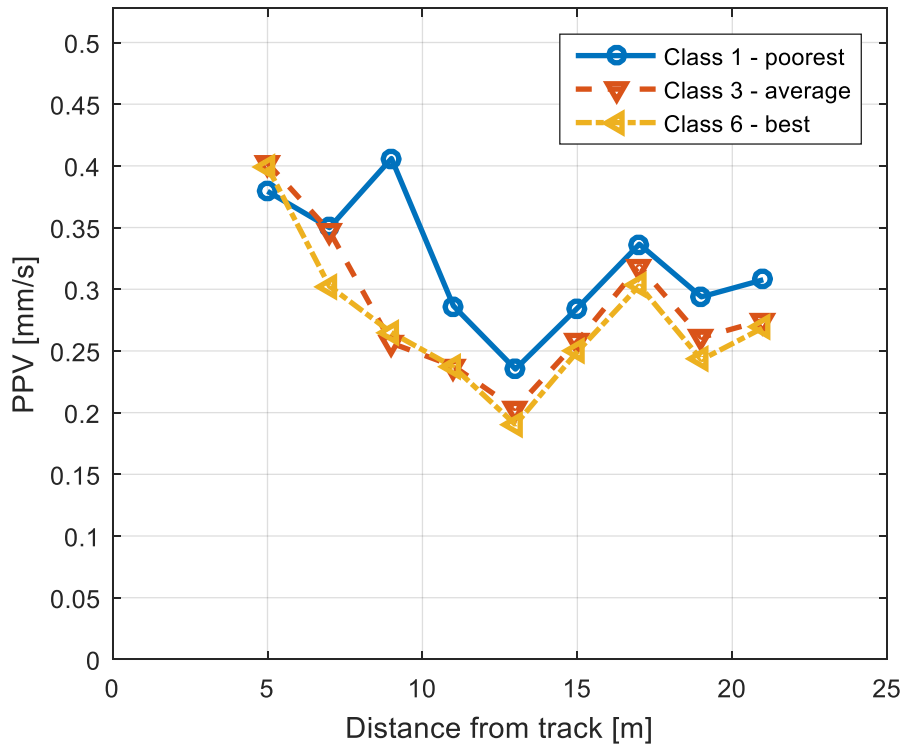


**Figure 7-15.** PPV variation with distance for different unevenness classes

Vibration velocity predictions are shown in Figure 7-14 and Figure 7-15 for different unevenness classes. As it can be anticipated, a higher level of response is obtained for the poorest unevenness class for all locations in *PPV* comparison and for near field in  $KB_{F,max}$  comparison. Response level for average unevenness class is slightly higher than response for the best unevenness class.

As already introduced in Chapter 2; ground vibrations caused by quasi static loading are present only at low frequencies, whereas vibrations caused by rail unevenness are present at a wide range of frequencies. In Figure 7-16, frequency content of ground velocity response at 11 m from track is plotted for different rail unevenness classes. It is observed that up to 50 Hz, vibration contents are almost the same for all three classes. For frequencies higher than 50 Hz, response content of the poorest unevenness class has much higher magnitudes than other classes.

Similarly, response content for average unevenness class is higher than that for the best unevenness class.

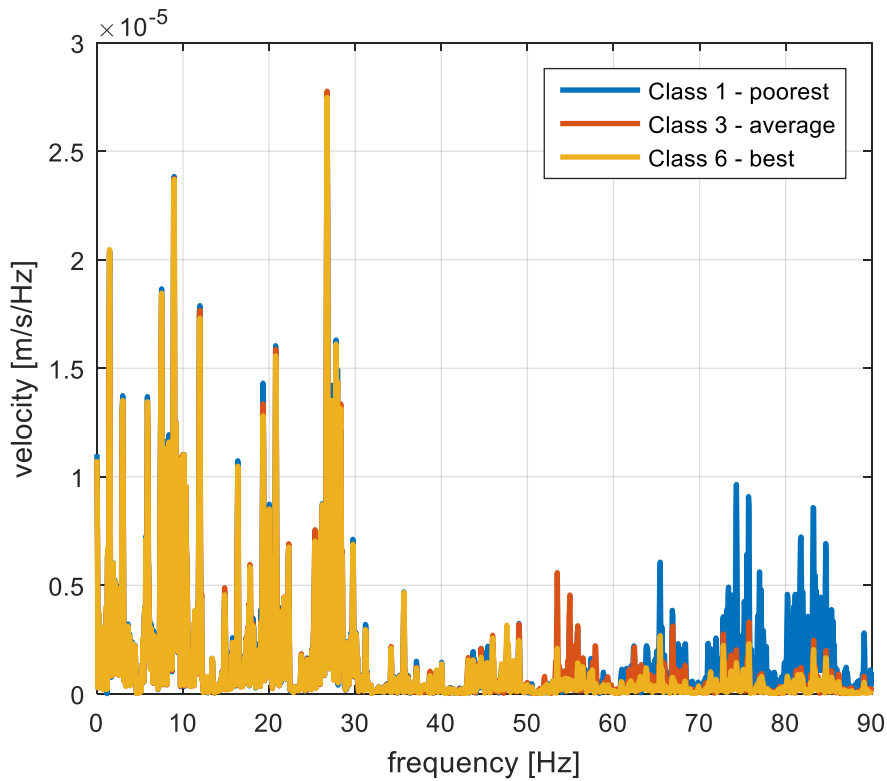


**Figure 7-16.** Frequency content of vibration response at 11 m from track, for different rail unevenness classes

### 7.3.2 Rail profile

The rail profile used in reference case is UIC 60. In this section, two different rail profiles, UIC 50 and UIC 54 are applied in the track modeling and their effect on ground vibration velocity levels is analyzed. Section parameters used in this study are given in Table 7-9 for rail profiles.

**Table 7-9.** Parameters for different rail profiles

	UIC 50	UIC 54	UIC 60
Area	63.54 cm <sup>2</sup>	68.86 cm <sup>2</sup>	76.70 cm <sup>2</sup>
Inertia	1940 cm <sup>4</sup>	2127 cm <sup>4</sup>	3038.3 cm <sup>4</sup>

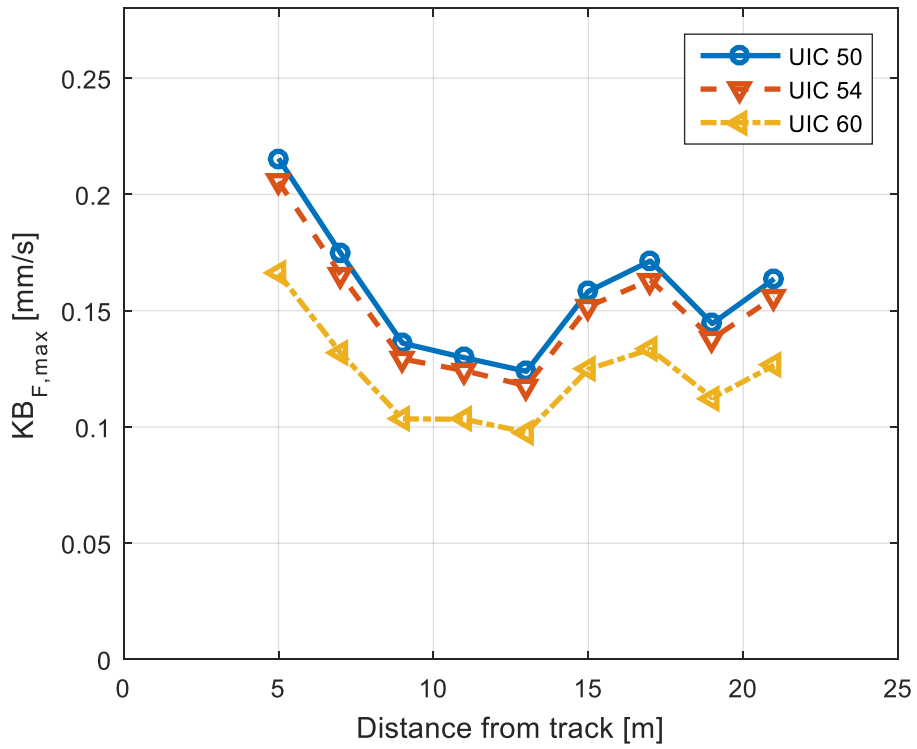


**Figure 7-17.**  $KB_{F,max}$  variation with distance for different rail profiles

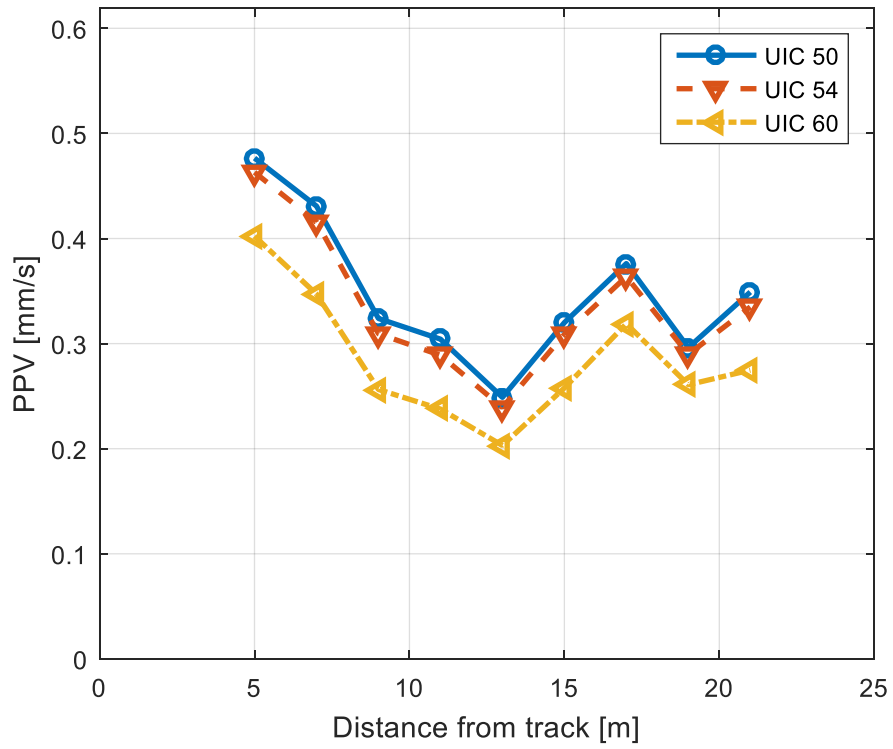


**Figure 7-18.** PPV variation with distance for different rail profiles

Ground vibration response levels are shown in Figure 7-17 and Figure 7-18 for different rail profiles. From these predictions, it is seen that lower vibration levels are observed when a rail profile with larger moment of inertia is applied in the track.

### 7.3.3 Rail pad stiffness

In this section, the effect of rail pad stiffness on ground velocity is studied. Three different rail pad stiffness values are analyzed: reference rail pad, softer rail pad and stiffer rail pad. Parameters for these rail pads are shown in Table 7-10 [44].

**Table 7-10.** Parameters for different rail pads

	Softer rail pad	Reference rail pad	Stiffer rail pad
Stiffness	$60 \cdot 10^6$ N/m	$90 \cdot 10^6$ N/m	$180 \cdot 10^6$ N/m
Damping	$52 \cdot 10^3$ Ns/m	$30 \cdot 10^3$ Ns/m	$28 \cdot 10^3$ Ns/m
Thickness	10 mm	10 mm	10 mm

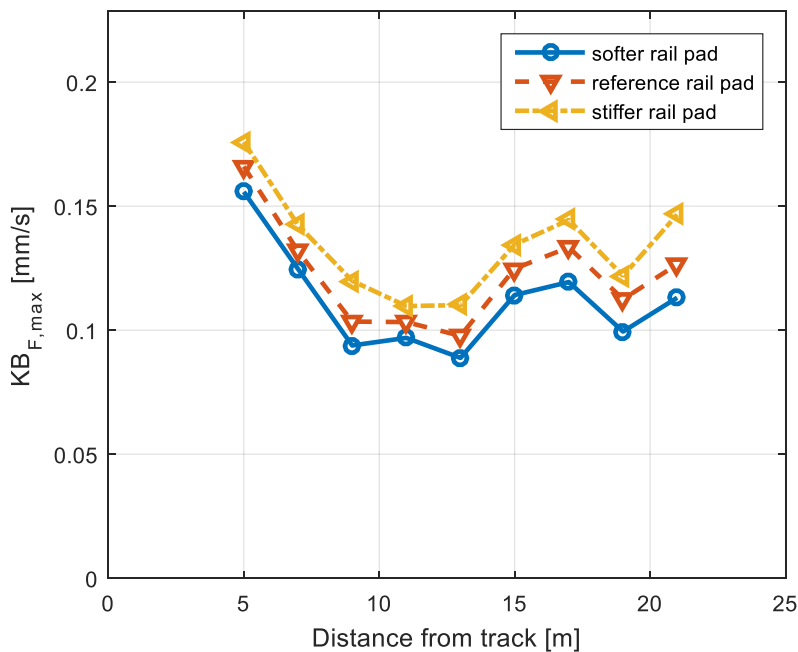


**Figure 7-19.**  $KB_{F,max}$  variation with distance for different rail pads

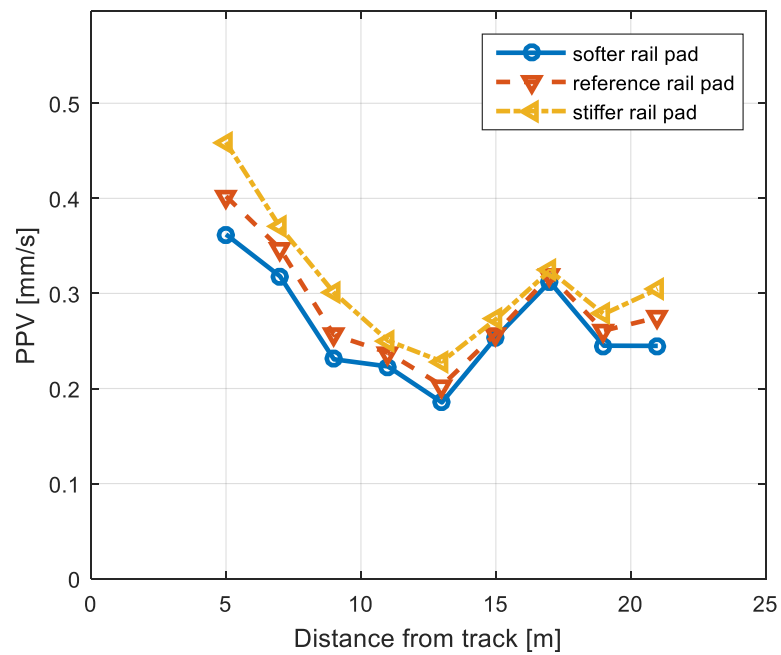


**Figure 7-20.** PPV variation with distance for different rail pads

Ground vibration levels predicted for tracks with different rail pads are shown in Figure 7-19 and Figure 7-20. It is observed that lower levels of vibration velocity are obtained as the stiffness of the rail pad applied is lower.

### 7.3.4 Sleeper spacing

A sleeper spacing value of 0.65 m is set in reference track analysis. In this part, tracks with two different sleeper spacing values, 0.60 m and 0.72 m, are analyzed to show its effect on ground vibration.

Prediction results for the effect of sleeper spacing values are shown in Figure 7-21 and Figure 7-22. It can be observed that magnitudes of ground velocity on near and far fields are only slightly influenced by the change in sleeper spacing value.

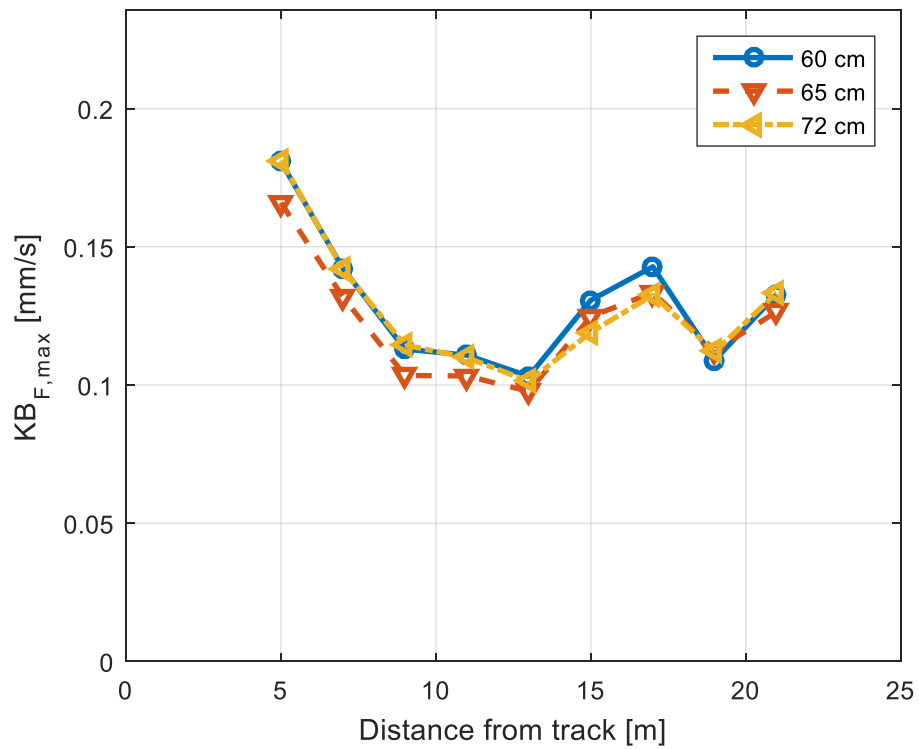


**Figure 7-21.**  $KB_{F,max}$  variation with distance for different sleeper spacing values

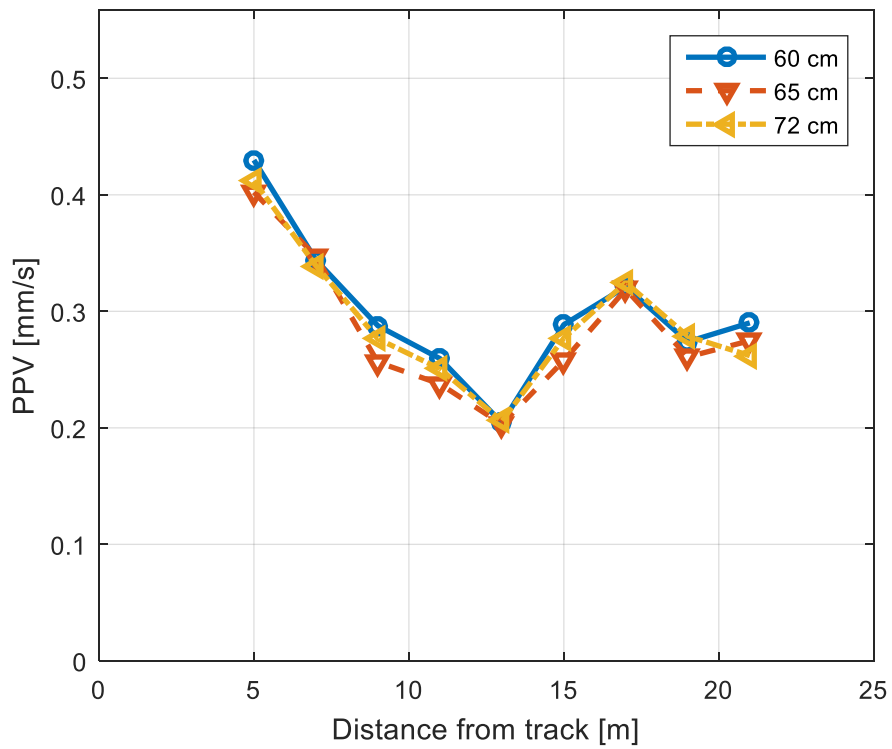


**Figure 7-22.** PPV variation with distance for different sleeper spacing values

### 7.3.5 Ballast, subballast and subgrade stiffness

In this part, three different tracks are modeled with different ballast, subballast and subgrade stiffness characteristics. One of the tracks analyzed is the reference track with parameters already given above. A softer track is modeled by setting Young's modulus values of track components half of the corresponding values in reference track. The third track model analyzed is a stiffer track that has Young's modulus values for track components twice in reference analysis. Table 7-11 lists the material properties for three tracks analyzed in this part.

**Table 7-11.** Young's modulus value for track components

	Softer track	Reference Track	Stiffer Track
Ballast	40 MPa	80 MPa	160 MPa
Subballast	100 MPa	200 MPa	400 MPa
Subgrade	60 MPa	120 MPa	240 MPa

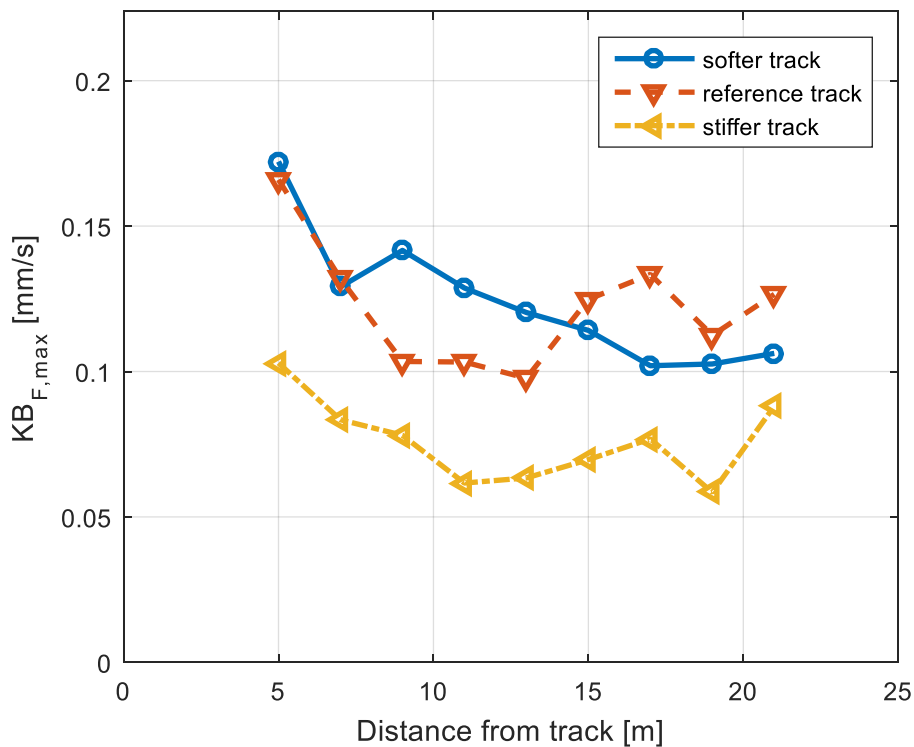


**Figure 7-23.**  $KB_{F,max}$  variation with distance for different track stiffness values

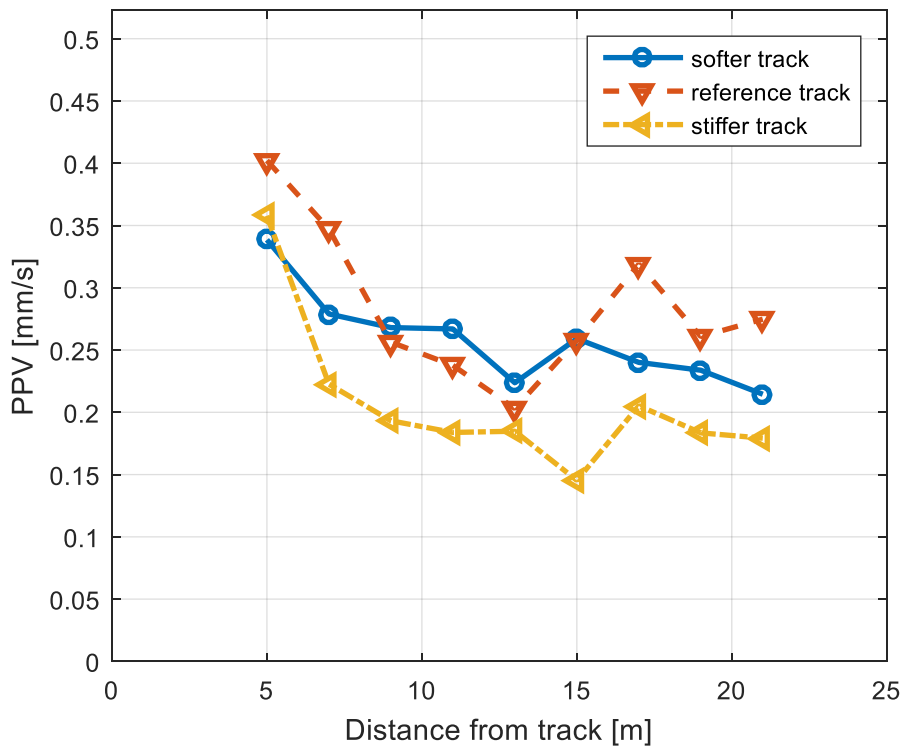


**Figure 7-24.** PPV variation with distance for different track stiffness values

Ground vibration levels are predicted for three tracks introduced and they are given in Figure 7-23 and Figure 7-24. For all three tracks, near field velocity levels are higher than far field levels. Vibration levels are predicted to be lower when stiffer track is used. As reference and softer tracks are compared; at mid field, velocity levels are higher for softer track and at near and far field locations, velocity levels are higher for reference track.

### 7.3.6 Embankment material

In this section, reference track model is modified by implying an embankment layer below subgrade layer. The effect of this embankment layer on ground vibration is analyzed by changing the stiffness of embankment material. Dimensions of embankment layer are given in Table 7-12. The angle of embankment with ground surface is 30°. Depending on the track design,

embankment material may be the same as the material of top soil layer or a different material may be used. In the analyses, three embankment cases are analyzed, with medium embankment material being the same as the material of top soil layer.

**Table 7-12.** Parameters for embankment layers analyzed

	Soft embankment	Medium embankment	Stiff embankment
Young's modulus	75 MPa	150 MPa	300 MPa
Height	3.000 m	3.000 m	3.000 m
Top width	7.000 m	7.000 m	7.000 m
Bottom width	17.400 m	17.400 m	17.400 m

It should be noted that ground response locations at 5 m and 7 m are placed on embankment surface and response predictions are calculated for these positions.

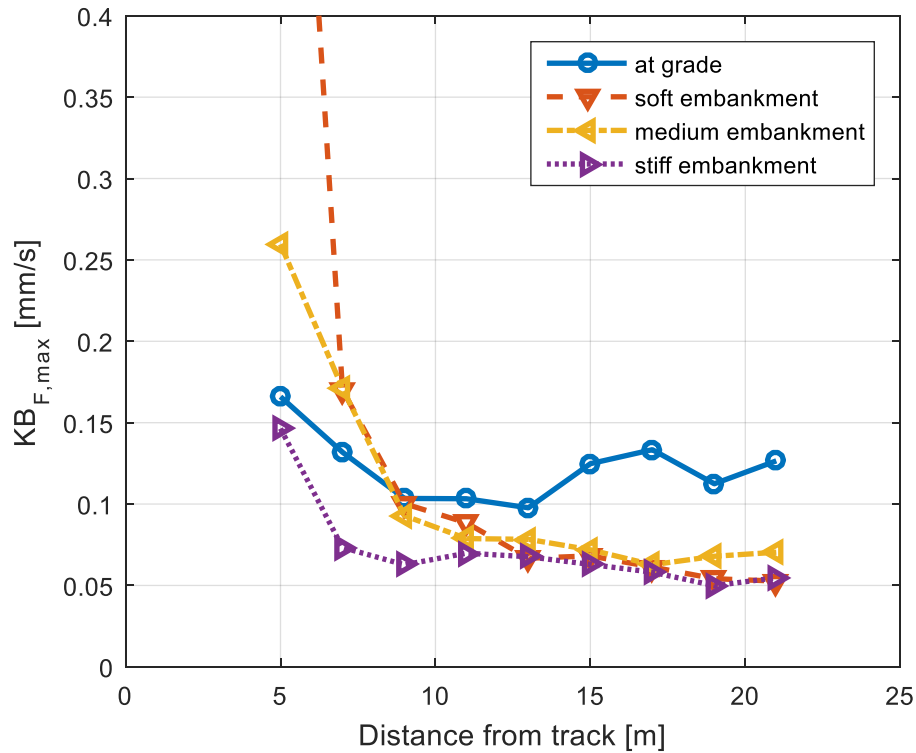


**Figure 7-25.**  $KB_{F,max}$  variation with distance for different embankment materials

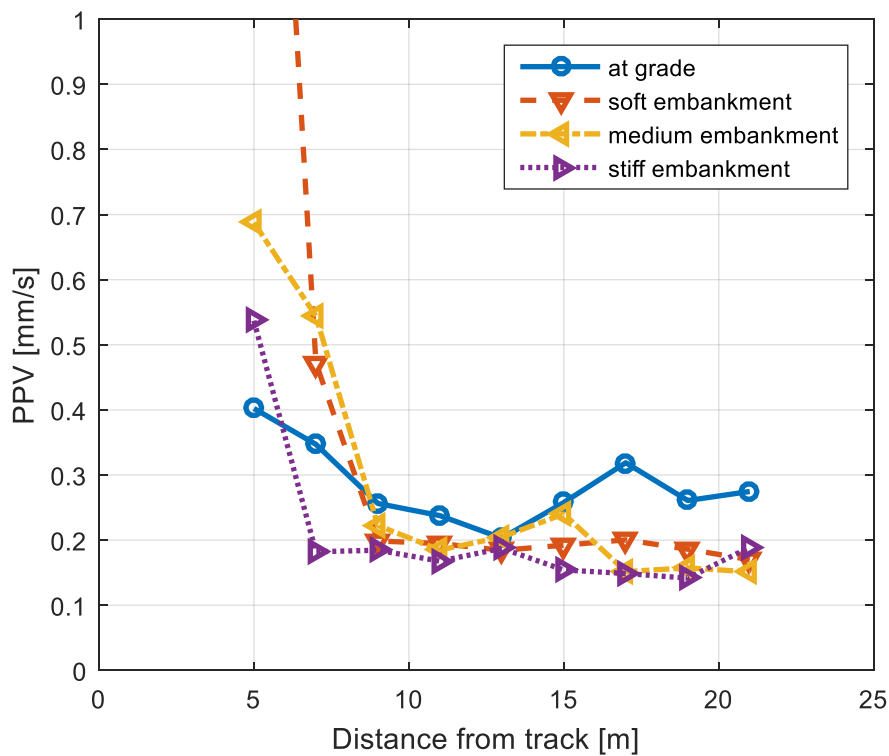


**Figure 7-26.** PPV variation with distance for different embankment materials

In Figure 7-25 and Figure 7-26, ground vibration predictions for different embankment material stiffness values are shown. At 5 m and 7 m distance from track, velocity responses for all embankment materials are higher than for grade track. For the remaining prediction locations, use of embankment material decreases ground vibration level when compared with at grade track. As embankment materials are compared, mid and far field vibrations are lower for the use of stiff embankment.

#### 7.4 Effects of ground parameters on ground vibration

In this section, material properties for ground layers are studied for their influence on ground vibration response. Material properties studied in the analyses are Young's modulus, Poisson's ratio, density and damping ratio.

### 7.4.1 Young's modulus

Young's modulus values of ground layers are varied and four different ground models are obtained. One of the ground models is the reference ground model. A softer and two stiffer models analyzed for their effects on ground vibration response. Young's modulus used in these ground models are listed in Table 7-13.

**Table 7-13.** Young's modulus values for analyzed ground layers

	Thickness (m)	Young's modulus (MPa)			
		Softer ground	Reference ground	Stiffer ground	Stiffest ground
Layer 1	3.0	120	150	180	225
Layer 2	3.0	240	300	360	450
Layer 3	4.0	800	1000	1200	1500

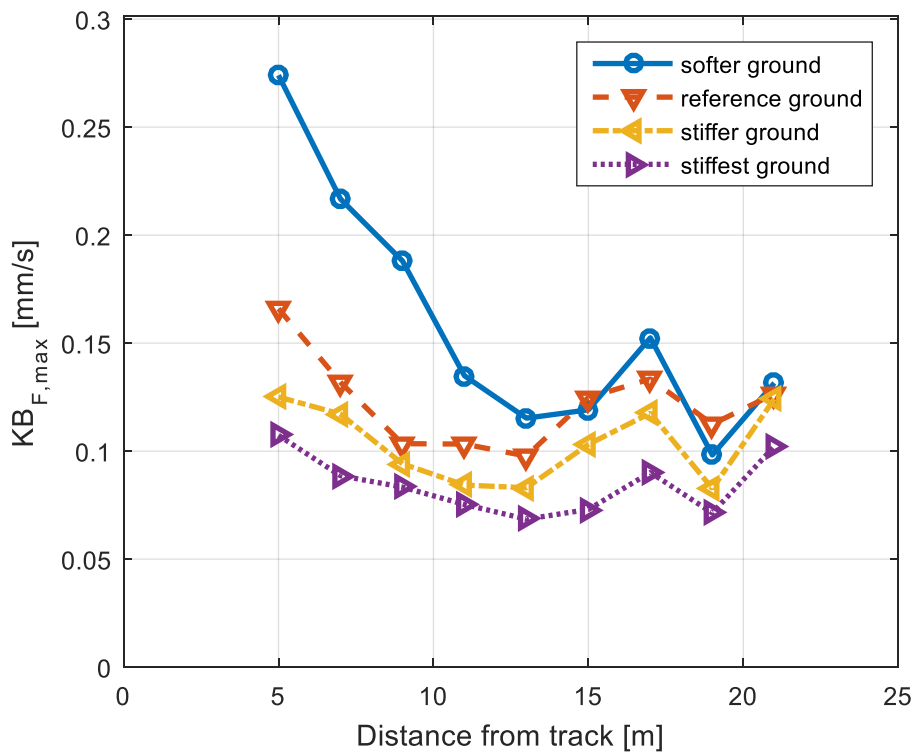


**Figure 7-27.**  $KB_{F,max}$  variation with distance for different Young's modulus values of ground model

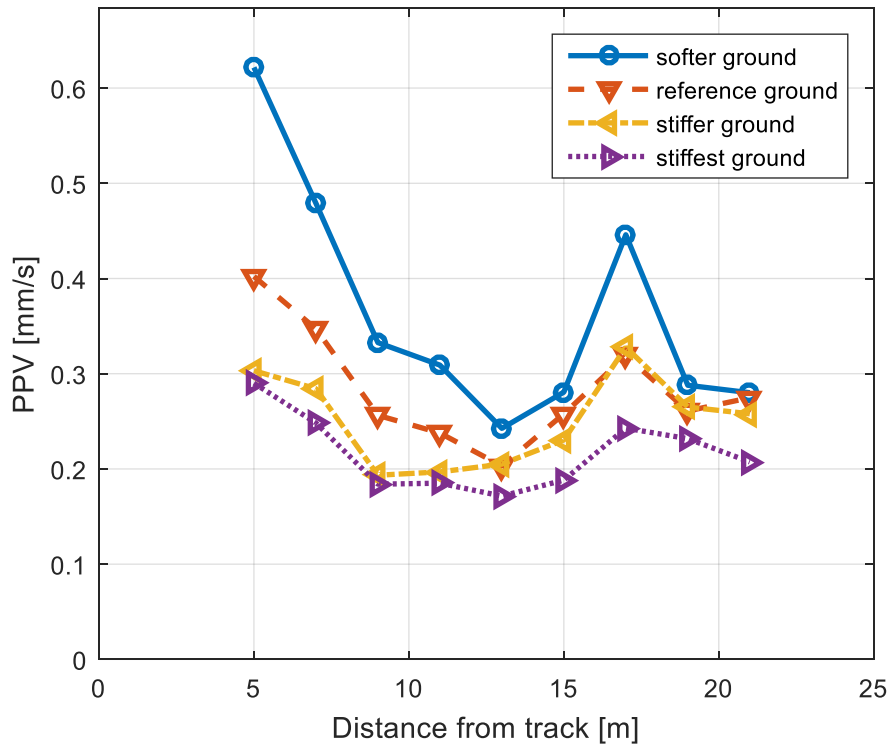


**Figure 7-28.** PPV variation with distance for different Young’s modulus values of ground model

In Figure 7-27 and Figure 7-28, predicted vibration levels are plotted for different Young’s modulus values of ground layers. Among four ground models, ground vibration levels are observed to be the highest for softer ground model, at both near and far field locations. When reference ground model is compared with stiffer ground models, vibration response magnitude is clearly higher at near field and slightly higher at mid and far fields. Stiffer ground model has higher velocity response magnitudes than stiffest ground model.

#### 7.4.2 Poisson’s ratio

In reference analysis, a Poisson’s ratio value of 0.30 is used for ground model. Ground models with Poisson’s ratio value of 0.25, 0.35 and 0.40 are analyzed in this section, in order to show the effect of Poisson’s ratio on ground vibrations.

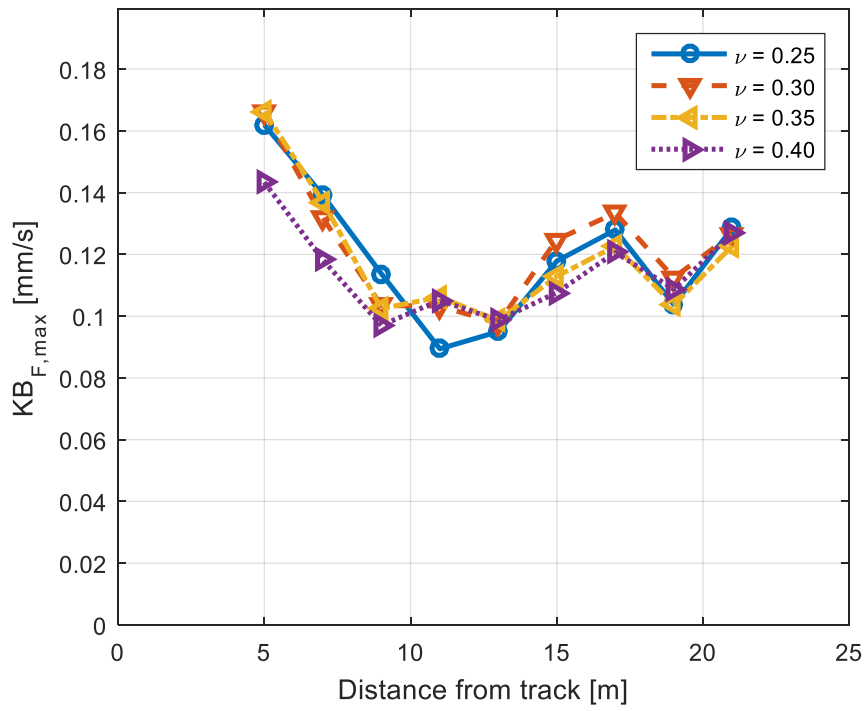


**Figure 7-29.**  $KB_{F,max}$  variation with distance for different Poisson's ratio values of ground model

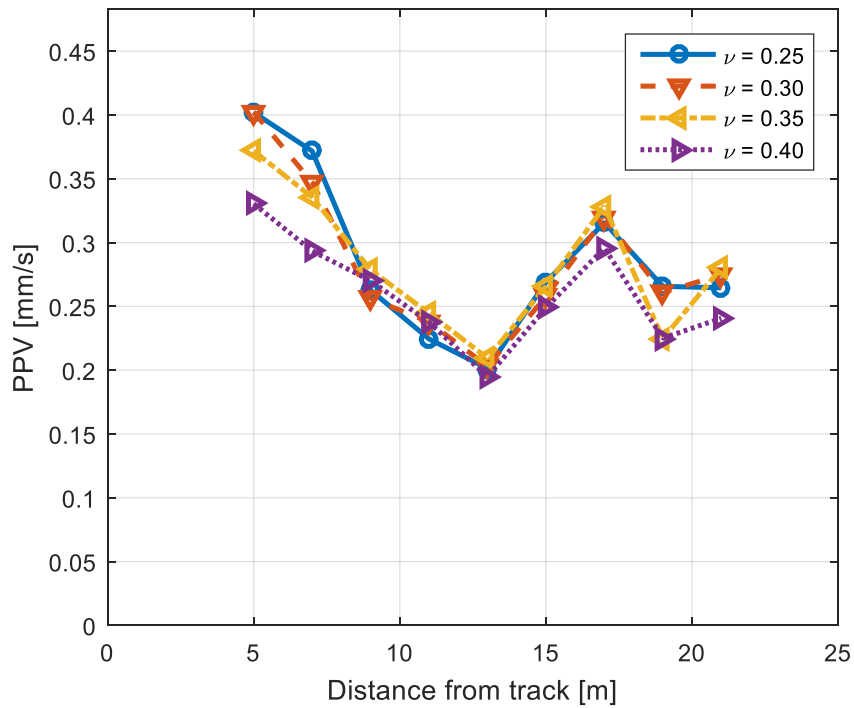


**Figure 7-30.** PPV variation with distance for different Poisson's ratio values of ground model

Vibration response prediction results are given in Figure 7-29 and Figure 7-30 for ground models with different Poisson's ratio values. For all four ground models, vibration levels are quite similar to each other. For near field *PPV* variation, a slight decrease is observed as Poisson's ratio increases.

### 7.4.3 Density

The influence of density of ground layers on ground velocity response is analyzed by calculating vibrations of four different models. Density values used in these models are 1800 kg/m<sup>3</sup>, 2000 kg/m<sup>3</sup> (reference value), 2200 kg/m<sup>3</sup> and 2400 kg/m<sup>3</sup>.

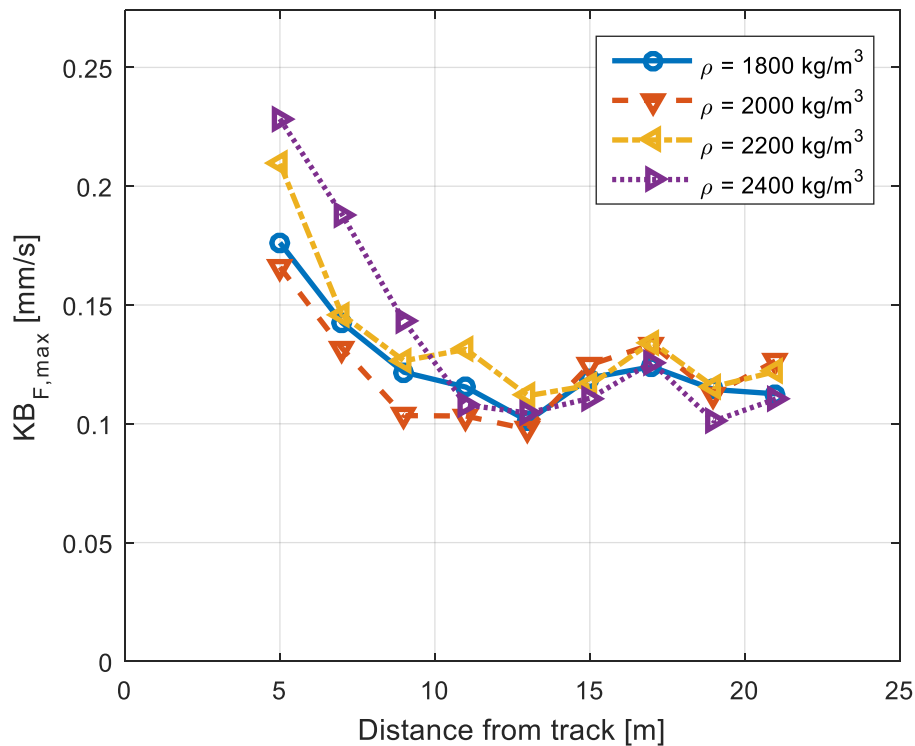


**Figure 7-31.**  $KB_{F,max}$  variation with distance for different density values of ground model

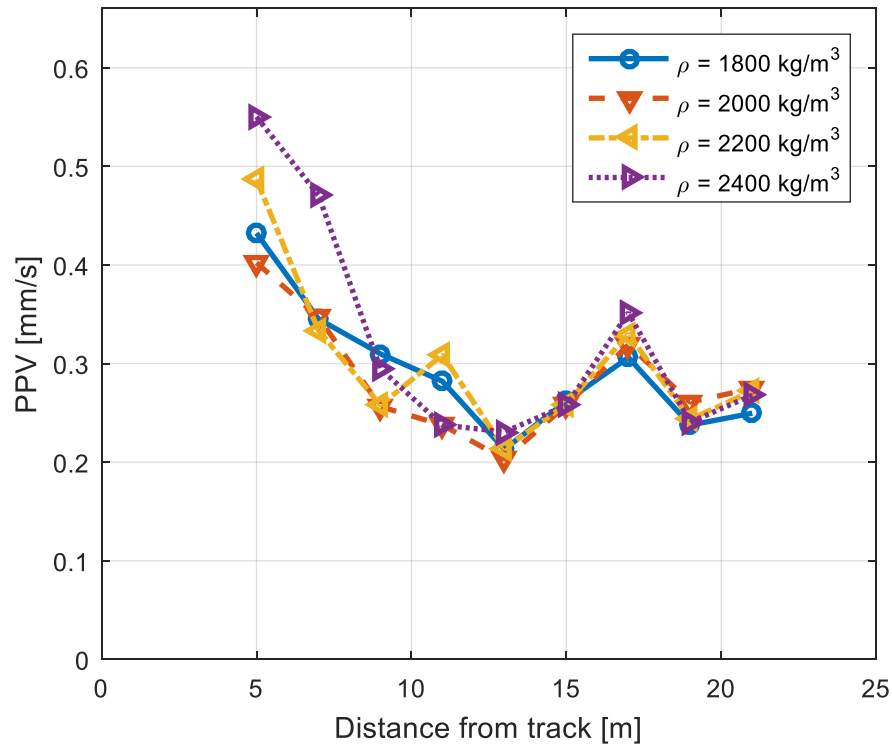


**Figure 7-32.** PPV variation with distance for different density values of ground model

Prediction results are shown in Figure 7-31 and Figure 7-32 for ground models with different density values. It is observed that at near field locations, vibration response levels are higher for models with density values higher than reference value. For mid and far field locations, response levels are close for all density values.

#### 7.4.4 Damping ratio

In reference analysis, ground damping is modeled as Rayleigh damping with a damping ratio of 0.0004 s. In this part, ground models with Rayleigh damping coefficient of 0.0002 s, 0.0003 s and 0.0005 s are to be analyzed for their effect on ground vibration levels.

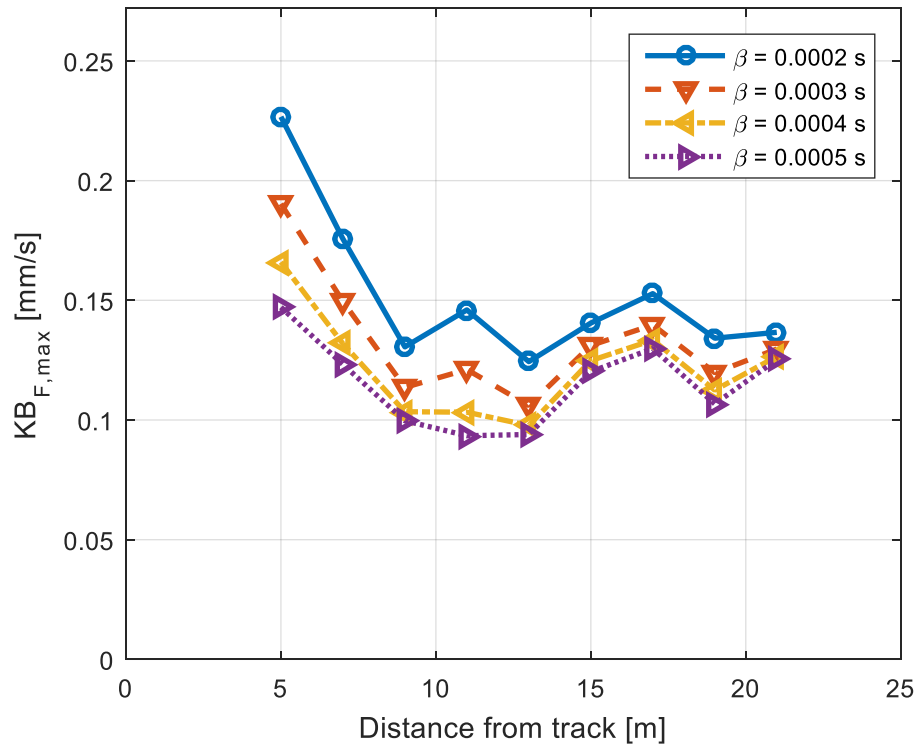


**Figure 7-33.**  $KB_{F,max}$  variation with distance for different ground damping models

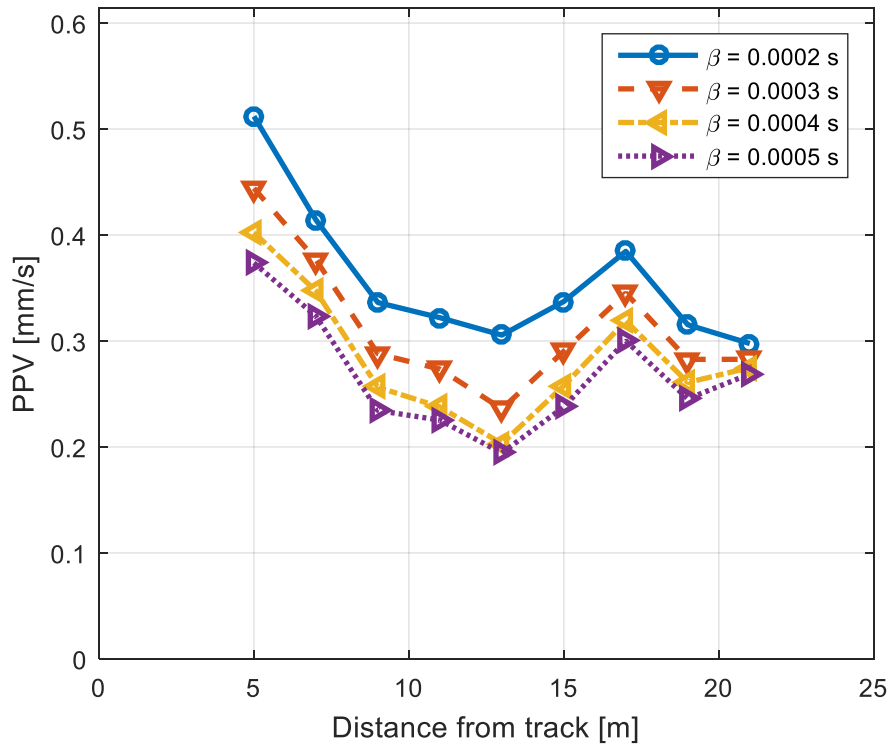


**Figure 7-34.** PPV variation with distance for different ground damping models

Ground velocity level predictions are shown in Figure 7-33 and Figure 7-34 for different ground damping models. It is clearly observed that very high levels of vibration are present in the response of ground model with a very light damping ratio,  $\beta = 0.0002$  s. Response levels are lower for larger damping ratio than levels.



## CHAPTER 8

### VIBRATION MITIGATION APPLICATIONS

In this chapter, three different types of vibration mitigations are analyzed by the proposed prediction model. Modeling details of these applications are given in each section. Predicted velocity distributions are compared with the reference case studied in the parametric analysis presented in Chapter 7.

#### 8.1 Under sleeper pad application

Under sleeper pads are placed between sleeper and ballast in order to mitigate railway traffic induced ground vibrations. Three different under sleeper pad stiffness values are compared. In Table 8-1, parameters for under sleeper pads analyzed are given.

**Table 8-1.** Parameters for under sleeper pads used in the analyses

	Soft under sleeper pad	Medium under sleeper pad	Stiff under sleeper pad
Stiffness	$28.8 \cdot 10^6$ N/m	$57.6 \cdot 10^6$ N/m	$115.2 \cdot 10^6$ N/m
Damping	$1.44 \cdot 10^6$ Ns/m	$2.88 \cdot 10^6$ Ns/m	$5.76 \cdot 10^6$ Ns/m
Thickness	10 mm	10 mm	10 mm

Under sleeper pads are modeled with link11 elements of ANSYS. For each element, the stiffness and damping coefficients are obtained by dividing the under sleeper pad stiffness and damping values by the number of elements under corresponding sleeper.

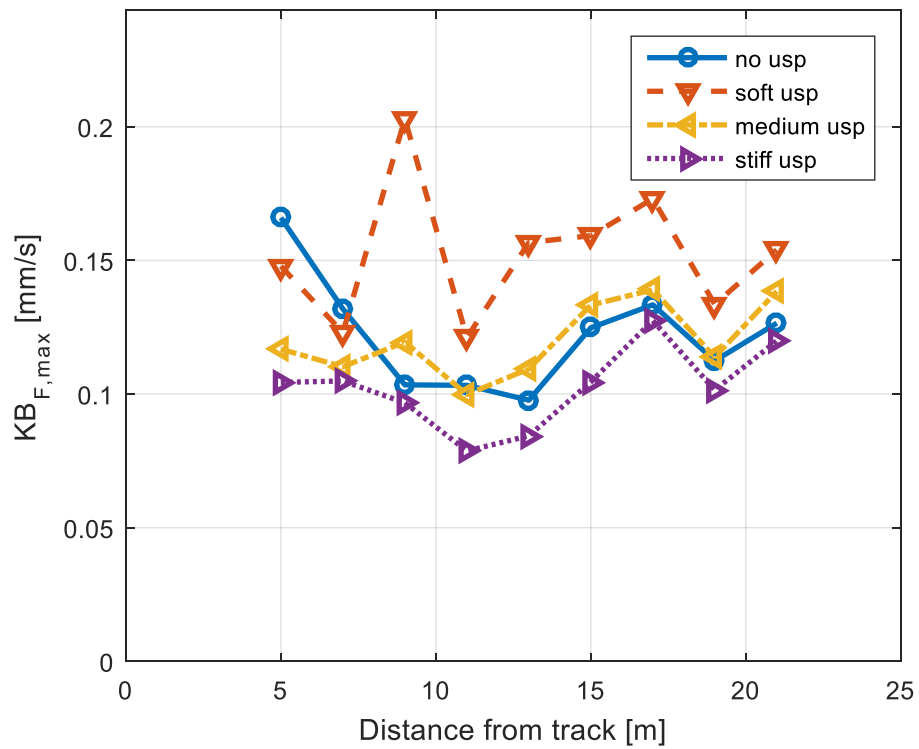


**Figure 8-1.**  $KB_{F,max}$  variation with distance for different under sleeper pad models

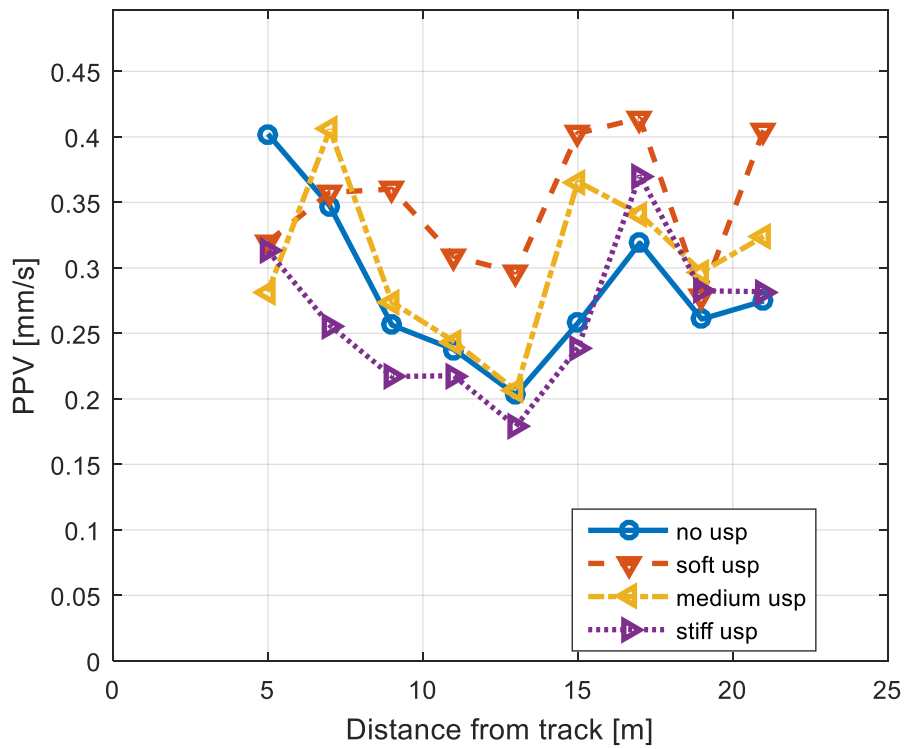


**Figure 8-2.** PPV variation with distance for different under sleeper pad models

Prediction results for ground vibration velocity levels are shown in Figure 8-1 and Figure 8-2 for under sleeper pad application in track. A level of mitigation is observed in near field  $KB_{F,max}$  levels when under sleeper pad is applied. For mid and far field locations, application of stiff under sleeper pad decreases vibration response levels. In  $PPV$  level comparison, mitigation is obtained for near and mid field locations when stiff under sleeper pad is applied to the track.

## 8.2 Under ballast mat application

Under ballast mat is applied between ballast and subballast layers to mitigate vibrations. Finite element model of the track is modified and under ballast mat is applied in ANSYS. Three different stiffness values are studied for under ballast mat and in Table 8-2, these values are listed.

**Table 8-2.** Parameters for under ballast mats used in the analyses

	Soft under ballast mat	Medium under ballast mat	Stiff under ballast mat
Stiffness	$1485 \cdot 10^6$ N/m	$2970 \cdot 10^6$ N/m	$4950 \cdot 10^6$ N/m
Damping	$7.4 \cdot 10^6$ Ns/m	$14.9 \cdot 10^6$ Ns/m	$24.8 \cdot 10^6$ Ns/m
Thickness	10 mm	10 mm	10 mm

Similar to under sleeper pad modeling, link11 elements are used in ANSYS in order to model under ballast mats in track. Stiffness and damping values given in Table 8-2 are divided by the total number of nodes on the surface between ballast and subballast, and the value of spring and damping constants for each element is calculated.

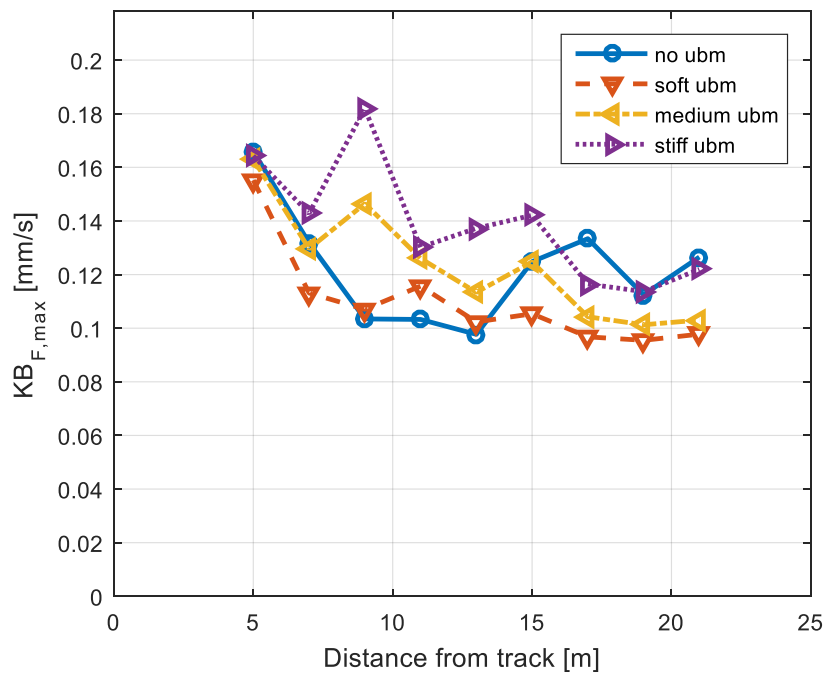


**Figure 8-3.**  $KB_{F,max}$  variation with distance for different under ballast mat models

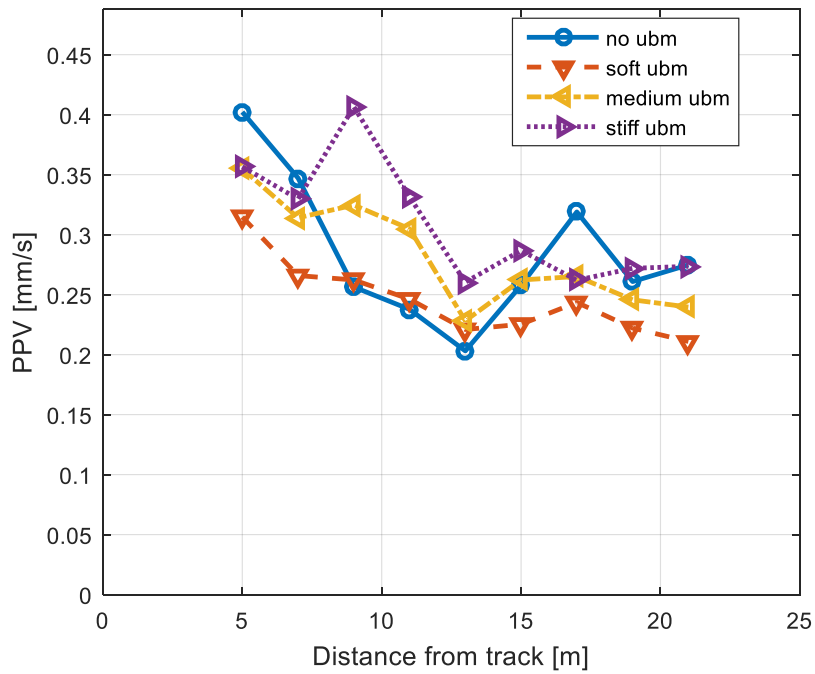


**Figure 8-4.** PPV variation with distance for different under ballast mat models

In Figure 8-3 and Figure 8-4, calculated ground velocity responses are shown for track models with different under ballast mat stiffness values. Vibration response decreases at near and far fields, but an increase is observed in mid field locations. Prediction results show that when the softer under ballast mat is applied to the track, lower values are obtained in vibration response.

### **8.3 Trench application**

Trench location is designated at 10.5 m from track center and trench depth is taken as 3.0 m. Two different trench applications are considered with widths of 1.0 m and 2.0 m. In modeling of ground with trench, first soil layer is divided into two components. For 1.0 m trench width, two soil blocks of 10 m and 14 m length in lateral direction is modeled. Similarly, for 2.0 m trench width, two blocks of 9.5 m and 13.5 m are modeled. These blocks are coupled to lower soil layers by modal coupling. Coupling of ground model with track model is similar to already described in numerical modeling part of this thesis.

Vibration response predictions are shown in Figure 8-5 and Figure 8-6, for 1.0 m and 2.0 m width trench applications. It is observed that a clear mitigation is predicted when a trench is present on the ground.

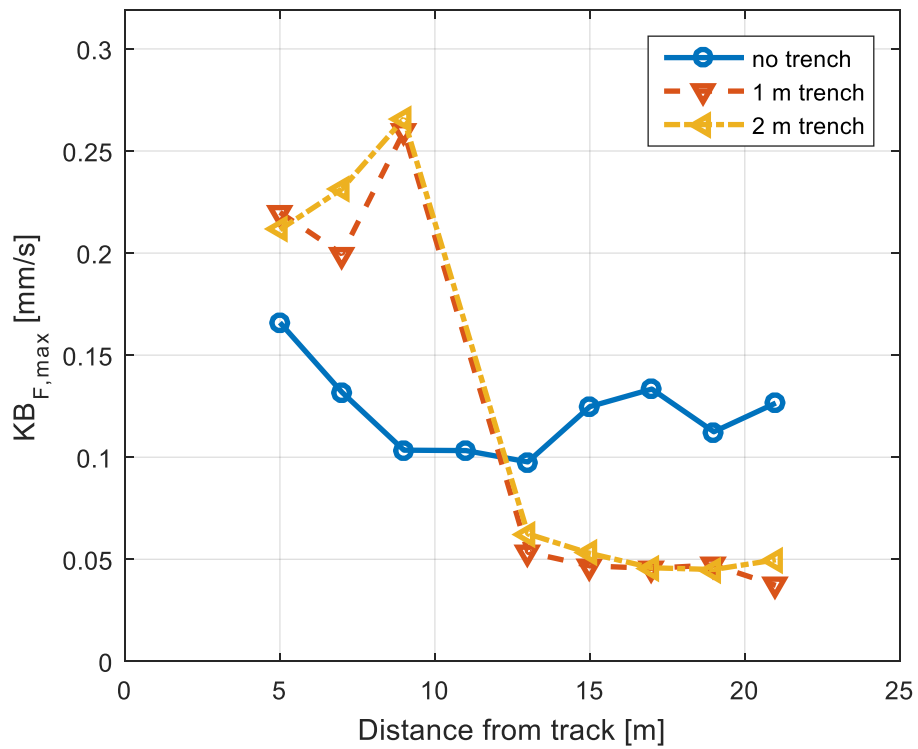


**Figure 8-5.**  $KB_{F,max}$  variation with distance for trench application

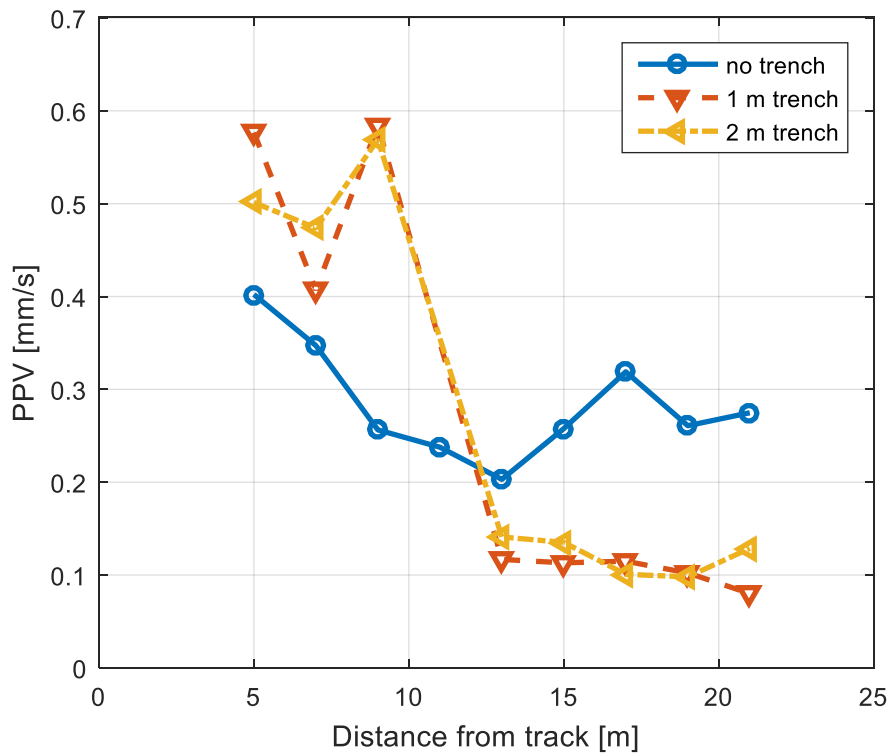


**Figure 8-6.** PPV variation with distance for trench application

## CHAPTER 9

### CONCLUSIONS

#### 9.1 Summary and conclusions

In this dissertation, a time domain three-dimensional numerical prediction model is proposed to analyze railway induced ground vibration.

In the introductory parts of this thesis, motivation for the study is presented along with some necessary definitions. Due to developments in railway construction, environmental vibrations are more likely to pose problems for buildings nearby railway and to cause annoyance on people in these buildings. Vibration generation occurs due to the dynamic loadings present in the contact between wheels and rail. Vibrations generated due to these loadings propagate along railway track and through ground. Allowable vibration limits for buildings and people are given in several standards, norms and regulations. A practical vibration prediction model should give outputs in terms of vibration metrics defined in these documents. All system components should be considered in the prediction model with restricted level of assumptions. Feasible calculation time and good accuracy are also important characteristics of a prediction model. Several analytical, numerical and empirical prediction models have been proposed in literature. Time domain three-dimensional finite element models are shown to predict vibration levels with good accuracy. However, due to calculation stability, small time increments should be applied, and therefore these models have drawback of long computational times.

Vibration is generated due to the interaction between wheel and rail. There are two types of loading in rail-wheel contact: quasi static loading due to moving weights and dynamic loading due to unevenness of wheel and rail surfaces. The contact is modeled with nonlinear Hertzian contact stiffness. Rail unevenness classes are given by power spectral density formulations. Vibrations originating from these mechanisms may cause disturbance for people inside railway vehicle; however, only the vibrations propagated in track and ground are investigated in this study. Ballasted track is the typical railway track type and it is also applied in this study. Rail, rail pad, sleeper, ballast, subballast and subgrade are typical components of ballasted track; and in the prediction model, these elements are modeled in detail. Wave propagation in ground layers is present in the form of three wave types: compressional wave, shear wave and Rayleigh wave. In modeling of ground layers, typically, four material properties are used: Young's modulus, Poisson's ratio, density and damping ratio. Assessment of environmental vibrations is performed in terms of typical vibration metrics defined in standards such as peak particle velocity, maximum weighted severity and maximum running root-mean-square velocity level.

In the proposed vibration prediction model, first modal analyses are performed for ground, track and vehicle subsystems. Modal parameters are obtained from these analyses and these parameters are used to calculate impulse response functions. Vibration response is calculated by convolution of loading history and impulse response functions.

For ground layers, finite difference modal analysis is introduced. Equations of motion and equations for Hooke's law are written by finite difference approximations. Following central difference and adjusted finite difference formulations available in literature, a set of linear equations are obtained. For free motion analysis, this set of equations is modified to obtain system matrices. From eigenvalue analysis of these matrices, modal parameters of ground layers are obtained. These modal parameters are obtained for each ground layer. Ground

layers are then coupled by implementing modal coupling technique. For coupled ground layers, boundary conditions are applied by modal coupling technique. Two types of boundary conditions are applied. On two surfaces with normal in train motion direction, all displacement components are fixed. On the symmetry surface, symmetrical boundary condition is applied by fixing only the displacement in normal direction. After fixing application, undamped modal parameters are modified with Rayleigh damping ratio and damped modal parameters are obtained. Local damping boundary condition is then applied on two surfaces: on the bottom surface of coupled ground model and on the surface opposite to the symmetry surface.

Ballast track is modeled in finite element software ANSYS. Boundary condition fixing is applied similar to the ground model. Undamped modal analysis is performed and modal parameters are saved to be loaded later in MATLAB. Modification for Rayleigh damping ratio and rail pad damping are applied and damped modal parameters are obtained. Modal parameters of ground and track models are then coupled and modal parameters for track-and-ground-coupled structure are obtained.

As modal parameters of coupled ground track model are available, impulse response functions between nodes on rail are calculated, as well as impulse response functions between nodes on rail and ground response nodes. Impulse response functions are also calculated for vehicles.

A time array for calculation is selected. Time increment in this time array is selected as 0.5 ms, and this value is one order higher than applied in three-dimensional finite element prediction models available in literature. This leads to decrease in total number of time step, and therefore decrease in computational times. End limit of time array is selected as the time when the last wheel leaves the rail nodes in consideration. Initial wheel location array is defined by wheel

configuration of railway vehicle. Wheel locations at each time step is then calculated by adding distance traveled to this initial location array. These wheel locations are compared with locations of rail nodes, and the rail node that each wheel will be in contact is found. At each calculation step, rail and wheel displacements are compared, and following the nonlinear Hertzian contact model, the rail-wheel contact force is calculated. Force on rail node and force on wheel are calculated from this force. Force on the rail node is convolved with impulse response functions between rail nodes, and responses of rail nodes due to this force are obtained and added to rail node response history. Similarly, the force on wheel is convolved with impulse response function of wheel and the response of wheel due this force is obtained and added to the wheel response history. These force and response calculations are carried for the whole time array.

After calculation of rail forces for whole the time array; responses of nodes on ground surface are calculated by convolution of rail forces with the corresponding impulse response functions between rail nodes and ground response nodes.

Proposed prediction model is validated by comparing prediction results with measurement records at two different sites, available in literature. In validation process, time and frequency domain responses are compared as well as different vibration metrics, such as peak particle velocity, maximum weighted severity and root-mean-square velocity level. Comparisons are performed on the basis of measurements on Thalys high speed train traffic.

In validation study with measurements at Leuze-en-Hainaut, time history and frequency content of vibration velocity at two locations are compared. Timing and shape of the simulations are shown to be in good agreement with measurement results. Response to central cars is slightly underestimated at 11 m from the track, and small overestimations are present after the passage of the end traction car for simulations at two locations. Dominant frequency range in measured velocity

response is between 15 and 35 Hz, and predicted velocity content is also high in this range of frequencies. Several peaks out of range are also identified by predictions. *VdB* comparisons are also shown at four locations, for vertical, longitudinal and horizontal components of vibration velocity. For vertical velocity, velocity levels are predicted with a maximum difference of 2.5 *dB*. For longitudinal and horizontal components, maximum difference in predictions is 4.0 *dB*. Root-mean-square comparisons are also plotted for these velocity components.

Time history, weighted severity and frequency content predictions are compared with measurements at Mévergnies. Timing of predictions at two different locations is similar to the measurements. At 7 m from track, amplitude of predictions is similar to the measurements; and at 15 m from track, amplitude is relatively underestimated. The response to end cars is much clear in 7 m response. Vibration velocity weighted severity predictions identified the timing and shape of measurement results, except the response to the traction cars at 15 m. Frequency content is higher at 16 to 32 Hz range in prediction results, and this range is dominant in measurement results as well. A second observed range of 50 to 65 Hz in measurement frequency content is also identified by predictions at 7 m from track. The distribution of two vibration metrics, peak particle velocity and maximum weighted severity, are compared with measurement results. For predictions of both vibration metrics, decreasing behavior with distance is observed. For peak particle velocity predictions, far field values are in good agreement with measurements, however near field values are slightly underestimated. Maximum weighted severity levels are slightly overestimated for both near and far field locations.

A parametric analysis is presented for effects of several train, track and ground parameters on ground vibration levels. Analyzed parameters in this part are: train type, train speed, rail unevenness, rail profile, sleeper spacing, ballast, subballast

and subgrade stiffness, embankment material, Young's modulus, Poisson's ratio, density and damping ratio of ground layers.

Comparison for different train types shows that train axle load has direct effect on vibration level. Similarly, train speed also has direct effect on vibration levels, and higher vibration response is obtained for higher train speed.

Poorest rail unevenness leads to high magnitudes of vibration in *PPV* comparison at all locations and in near field in  $KB_{F,max}$  comparison. It is also shown that effect of dynamic loading due to rail unevenness is observed at high frequencies; whereas at low frequencies, it is shown that quasi static loading is dominant on responses. From comparison of different rail profiles, it is concluded when a rail profile with larger second moment of area is applied in track, lower vibration levels are predicted. An increase in vibration levels is predicted for an increase in rail pad stiffness. Effect of sleeper spacing value on ground velocity levels is observed to be insignificant, from comparison of three different sleeper spacing values. From analysis with stiffer ballast, subballast and subgrade material, lower ground velocity levels are obtained. When the reference track is compared with softer track; at near and far field locations, velocity levels are higher for reference track, and at mid field locations, velocity levels are higher for softer track. A decrease in ground vibration response is experienced for tracks over an embankment layer.

High magnitudes of vibrations are obtained for softer ground in the analyses. Response levels of reference ground model are much higher than stiffer models at near field and slightly higher at mid and far fields. For stiffer ground model, higher velocity levels are predicted when compared with stiffest ground model. Effect of Poisson's ratio on vibration levels is observed to be not significant. Only a slight decrease in vibration levels is predicted for an increase in Poisson's ratio of ground layers. Similarly, effect of density of ground layers is observed only in

near field locations; as higher vibration levels are predicted for models with density value higher than reference value, in near field. For lower ground damping ratio, larger magnitudes of vibrations are predicted.

Effects of vibration mitigation applications are also studied. Finite element model of track is modified for under sleeper pad and under ballast mat applications. It is observed that depending on the stiffness value of under sleeper pads and under ballast mats, levels of vibration mitigation change. Also, trench models with two different widths are studied and a clear level of decrease in ground vibration response is obtained.

Most time consuming steps of proposed model are steps with eigenvalue analyses. These steps are modal analyses of ground layers and eigenvalue analyses for coupling and fixing operations. An important note for modal analyses of ground layers is that if thickness and Poisson's ratio of two different layers are the same, modal parameters of these layers are related with respect to ratios in Young's modulus and density values. For example, in parametric analysis, thicknesses of first and second ground layers are the same, as well as Poisson's ratio and density. Modal parameters of the second layer can be obtained from that of first layer by simple operations, and no eigenvalue reanalysis is required. Impulse response function calculation and response calculation steps require shorter computational times.

Most important characteristic of proposed prediction model is its computational efficiency. One of the reasons of this is that the response is calculated at only necessary locations. In typical finite element calculations, response is calculated for whole domain which includes large number of nodes where response calculation is not necessary. Another reason for shorter calculation times is time increment size. In typical finite element simulations used in railway modeling, 0.05 ms of time step size is applied. This small size is selected to have stability in

response calculations. In the proposed model, this step size is 0.5 ms which is one order higher than former, and no instability is observed in analyses. Larger time increment in calculations gives smaller number of calculations and therefore shorter computational time requirements.

If there is no modification in track or ground modeling, time required for response prediction is considerably shortened to make parametric analyses of different train types, different train speeds and different rail classes. For these cases only vibration response calculation step in the proposed method is followed.

Modular structure of the proposed model brings further advantage when a modification is introduced in track or ground modeling. If the track model is modified and there is no modification on ground model; modal parameters obtained for ground model remains the same and they are coupled with new modal parameters of track model. For the case when ground model is modified, track modal parameters remain the same, and modal coupling is followed for the new ground modal parameters and available track modal parameters.

## **9.2 Recommendations for future work**

Through all calculations in this thesis, MATLAB and ANSYS are used as computer software. As generally time consuming sections of calculations are eigenvalue solution of large matrices, FORTRAN codes could be developed to decrease computation times.

Proposed model is applied on surface railway traffic in this thesis. It can be modified to model underground railway traffic by including a tunnel in finite element modeling of track.

In parametric analysis part, most important elements of railway are analyzed. Further analyses are also possible for effects of different elements. Vehicle models other than three degree of freedom model used in this thesis may be applied. For example, a full track and ground model without symmetry condition can be introduced to analyze the effect of different forms of rail unevenness on each rail.

In this thesis, ground responses are calculated for ground models with no structure. Buildings and wave barrier are possible structures to be placed on ground. These structures can be modeled with finite element software, and then they can be coupled with proposed prediction model, in order to analyze their effect on ground vibration levels.



## REFERENCES

- [1] D. Thompson, *Railway noise and vibration: mechanisms, modelling and means*. 2009.
- [2] L. Auersch, "Ground vibration due to railway traffic-The calculation of the effects of moving static loads and their experimental verification," *J. Sound Vib.*, vol. 293, no. 3–5, pp. 599–610, 2006.
- [3] V. K. Garg and R. V. Dukkipati, *Dynamics of railway vehicle systems*. 1984.
- [4] C. F. Bonnett, *Practical Railway Engineering*. 2005.
- [5] R. D. Woods, "Screening of Surface Wave in Soils," *J. Soil Mech. Found. Div.*, vol. 94, no. 4, pp. 951–980, 1968.
- [6] K. F. Graff, *Wave Motion in Elastic Solids*. 1991.
- [7] Rivas, "Review of existing standards, regulations and guidelines, as well as laboratory and field studies concerning human exposure to vibration," 2011.
- [8] X. Sheng and C. Jones, "The Fourier transformed stationary and moving dynamic flexibility matrices of a layered ground," *Report, Inst. Sound Vib. Res.*, no. 837, 1999.
- [9] X. Sheng, C. J. C. Jones, and M. Petyt, "Ground vibration generated by a load moving along a railway track," *J. Sound Vib.*, vol. 228, no. 1, pp. 129–156, 1999.
- [10] C. J. C. Jones, X. Sheng, and M. Petyt, "Simulation of ground vibrations from a moving harmonic load on a railway track," vol. 231, pp. 739–751, 2000.
- [11] X. Sheng, C. J. C. Jones, and D. J. Thompson, "A comparison of a theoretical model for quasi-statically and dynamically induced environmental vibration from trains with measurements," *J. Sound Vib.*, vol. 267, no. 3, pp. 621–635, 2003.
- [12] X. Sheng, C. J. C. Jones, and D. J. Thompson, "A theoretical study on the influence of the track on train-induced ground vibration," vol. 272, pp. 909–936, 2004.
- [13] X. Sheng, C. J. C. Jones, and D. J. Thompson, "A theoretical model for ground vibration from trains generated by vertical track irregularities," vol. 272, pp. 937–965, 2004.
- [14] A. Karlström and A. Boström, "An analytical model for train-induced

- ground vibrations from railways,” *J. Sound Vib.*, vol. 292, no. 1–2, pp. 221–241, 2006.
- [15] M. Katou, T. Matsuoka, O. Yoshioka, Y. Sanada, and T. Miyoshi, “Numerical simulation study of ground vibrations using forces from wheels of a running high-speed train,” *J. Sound Vib.*, vol. 318, no. 4–5, pp. 830–849, 2008.
- [16] P. Galvín and J. Domínguez, “High-speed train-induced ground motion and interaction with structures,” *J. Sound Vib.*, vol. 307, no. 3–5, pp. 755–777, 2007.
- [17] P. Galvín and J. Domínguez, “Analysis of ground motion due to moving surface loads induced by high-speed trains,” *Eng. Anal. Bound. Elem.*, vol. 31, no. 11, pp. 931–941, 2007.
- [18] G. Kouroussis, O. Verlinden, and C. Conti, “Ground propagation of vibrations from railway vehicles using a finite/infinite-element model of the soil,” *Proc. Inst. Mech. Eng. Part F J. Rail Rapid Transit*, vol. 223, no. 4, pp. 405–413, 2009.
- [19] J. Lysmer and R. L. Kuhlemeyer, “Finite-dynamic model for infinite media,” *J. Eng. Mech. Div.*, vol. 95, no. 4, pp. 859–877, 1969.
- [20] G. Kouroussis, O. Verlinden, and C. Conti, “A two-step time simulation of ground vibrations induced by the railway traffic,” *Proc. Inst. Mech. Eng. Part C J. Mech. Eng. Sci.*, vol. 226, no. 2, pp. 454–472, 2011.
- [21] G. Kouroussis, O. Verlinden, and C. Conti, “Contribution of vehicle / track dynamics to the ground vibrations induced by the Brussels tramway,” *Isma*, pp. 3489–3502, 2010.
- [22] G. Kouroussis, O. Verlinden, and C. Conti, “On the interest of integrating vehicle dynamics for the ground propagation of vibrations: the case of urban railway traffic,” *Veh. Syst. Dyn.*, vol. 48, no. 12, pp. 1553–1571, 2010.
- [23] G. Kouroussis, O. Verlinden, and C. Conti, “Efficiency of resilient wheels on the alleviation of railway ground vibrations,” *Proc. Inst. Mech. Eng. Part F J. Rail Rapid Transit*, vol. 226, no. 4, pp. 381–396, 2012.
- [24] G. Kouroussis, L. Van Parys, C. Conti, and O. Verlinden, “Prediction of environmental vibrations induced by railway traffic using a three-dimensional dynamic finite element analysis,” in *Proceedings of the Thirteenth International Conference on Civil, Structural and Environmental Engineering Computing*, 2011.
- [25] G. Kouroussis, L. Van Parys, C. Conti, and O. Verlinden, “Using three-dimensional finite element analysis in time domain to model railway-induced ground vibrations,” *Adv. Eng. Softw.*, vol. 70, pp. 63–76, 2014.
- [26] G. Kouroussis, O. Verlinden, and C. Conti, “Free field vibrations caused by high-speed lines: Measurement and time domain simulation,” *Soil Dyn. Earthq. Eng.*, vol. 31, no. 4, pp. 692–707, 2011.
- [27] G. Kouroussis, C. Conti, and O. Verlinden, “Experimental study of ground

- vibrations induced by Brussels IC/IR trains in their neighbourhood,” *Mech. Ind.*, vol. 14, no. 2, pp. 99–105, 2013.
- [28] G. Kouroussis, G. Gazetas, I. Anastasopoulos, C. Conti, and O. Verlinden, “Discrete modelling of vertical track-soil coupling for vehicle-track dynamics,” *Soil Dyn. Earthq. Eng.*, vol. 31, no. 12, pp. 1711–1723, 2011.
- [29] G. Kouroussis and O. Verlinden, “Prediction of railway induced ground vibration through multibody and finite element modelling,” *Mech. Sci.*, vol. 4, no. 1, pp. 167–183, 2013.
- [30] G. Kouroussis, C. Conti, and O. Verlinden, “Investigating the influence of soil properties on railway traffic vibration using a numerical model,” *Veh. Syst. Dyn.*, vol. 51, no. June 2013, pp. 421–442, 2013.
- [31] G. Kouroussis, N. Pauwels, P. Brux, C. Conti, and O. Verlinden, “A numerical analysis of the influence of tram characteristics and rail profile on railway traffic ground-borne noise and vibration in the Brussels Region,” *Sci. Total Environ.*, vol. 482–483, no. 1, pp. 452–460, 2014.
- [32] G. Kouroussis, D. P. Connolly, M. C. Forde, and O. Verlinden, “Train speed calculation using ground vibrations,” *Proc. Inst. Mech. Eng. Part F J. Rail Rapid Transit*, vol. 229, no. 5, pp. 466–483, 2015.
- [33] D. Connolly, A. Giannopoulos, and M. C. Forde, “Numerical modelling of ground borne vibrations from high speed rail lines on embankments,” *Soil Dyn. Earthq. Eng.*, vol. 46, pp. 13–19, 2013.
- [34] D. P. Connolly, G. Kouroussis, a. Giannopoulos, O. Verlinden, P. K. Woodward, and M. C. Forde, “Assessment of railway vibrations using an efficient scoping model,” *Soil Dyn. Earthq. Eng.*, vol. 58, pp. 37–47, 2014.
- [35] J. A. Forrest and H. E. M. Hunt, “A three-dimensional tunnel model for calculation of train-induced ground vibration,” *J. Sound Vib.*, vol. 294, no. 4, pp. 678–705, 2006.
- [36] M. F. M. Hussein and H. E. M. Hunt, “An insertion loss model for evaluating the performance of floating-slab track for underground railway tunnels,” in *Tenth International Congress on Sound and Vibration*, 2003, pp. 1–8.
- [37] M. F. M. Hussein, S. Gupta, H. E. M. Hunt, G. Degrande, and J. P. Talbot, “An efficient model for calculating vibration from a railway tunnel buried in a half-space,” *Proc. Thirteen. Int. Congr. Sound Vib. Vienna*, 2006.
- [38] M. F. M. Hussein and H. E. M. Hunt, “A software application for calculating vibration due to moving trains in underground railway tunnels,” in *Noise and vibration: Emerging methods NOVEM*, 2009.
- [39] J. A. Forrest and H. E. M. Hunt, “Ground vibration generated by trains in underground tunnels,” *J. Sound Vib.*, vol. 294, no. 4, pp. 706–736, 2006.
- [40] G. Degrande, D. Clouteau, R. Othman, M. Arnst, H. Chebli, R. Klein, P. Chatterjee, and B. Janssens, “A numerical model for ground-borne vibrations from underground railway traffic based on a periodic finite element-boundary element formulation,” *J. Sound Vib.*, vol. 293, no. 3–5,

- pp. 645–666, 2006.
- [41] D. Clouteau, M. Arnst, T. M. Al-Hussaini, and G. Degrande, “Freefield vibrations due to dynamic loading on a tunnel embedded in a stratified medium,” *J. Sound Vib.*, vol. 283, no. 1–2, pp. 173–199, 2005.
  - [42] S. Gupta, M. F. M. Hussein, G. Degrande, H. E. M. Hunt, and D. Clouteau, “A comparison of two numerical models for the prediction of vibrations from underground railway traffic,” *Soil Dyn. Earthq. Eng.*, vol. 27, no. 7, pp. 608–624, 2007.
  - [43] D. P. Connolly, P. Alves Costa, G. Kouroussis, P. Galvin, P. K. Woodward, and O. Laghrouche, “Large scale international testing of railway ground vibrations across Europe,” *Soil Dyn. Earthq. Eng.*, vol. 71, pp. 1–12, 2015.
  - [44] G. Kouroussis, O. Verlinden, and C. Conti, “Influence of some vehicle and track parameters on the environmental vibrations induced by railway traffic,” *Veh. Syst. Dyn.*, vol. 50, no. 4, pp. 619–639, 2012.
  - [45] G. Kouroussis, D. P. Connolly, and O. Verlinden, “Railway-induced ground vibrations – a review of vehicle effects,” *Int. J. Rail Transp.*, vol. 2, no. 2, pp. 69–110, 2014.
  - [46] D. Connolly, A. Giannopoulos, W. Fan, P. K. Woodward, and M. C. Forde, “Optimising low acoustic impedance back-fill material wave barrier dimensions to shield structures from ground borne high speed rail vibrations,” *Constr. Build. Mater.*, vol. 44, pp. 557–564, 2013.
  - [47] P. A. V. Urgueira, “Dynamic analysis of coupled structures using experimental data,” Imperial College, University of London, 1989.
  - [48] B. Fornberg, “Generation of finite difference formulas on arbitrarily spaced grids,” *Math. Comput.*, vol. 51, no. 184, pp. 699–706, 1988.
  - [49] J. Kristek, P. Moczo, and R. J. Archuleta, “Efficient methods to simulate planar free surface in the 3D 4(th)-order staggered-grid finite-difference schemes,” *Stud. Geophys. Geod.*, vol. 46, no. 2, pp. 355–381, 2002.
  - [50] P. Galvín and J. Domínguez, “Experimental and numerical analyses of vibrations induced by high-speed trains on the Córdoba-Málaga line,” *Soil Dyn. Earthq. Eng.*, vol. 29, no. 4, pp. 641–657, 2009.
  - [51] G. Kouroussis, D. P. Connolly, B. Olivier, O. Laghrouche, and P. A. Costa, “Railway cuttings and embankments: Experimental and numerical studies of ground vibration,” *Sci. Total Environ.*, vol. 557–558, pp. 110–122, 2016.
  - [52] D. P. Connolly, G. Kouroussis, P. K. Woodward, O. Verlinden, A. Giannopoulos, and M. C. Forde, “Field testing and analysis of high speed rail vibrations,” *Soil Dyn. Earthq. Eng.*, vol. 67, pp. 102–118, 2014.
  - [53] G. Kouroussis, “Mesures de vibrations induites sur l’environnement par le passage de trains a grande vitesse,” 2005.
  - [54] G. Kouroussis, D. P. Connolly, K. Vogiatzis, and O. Verlinden, “Modelling the environmental effects of railway vibrations from different types of rolling stock: a numerical study,” *Shock Vib.*, vol. 2015, 2015.

## CURRICULUM VITAE

### PERSONAL INFORMATION

Surname, Name: Alan, Salih

Nationality: Turkish (TC)

Date and Place of Birth: 4 July 1984, Kızılcahamam

Marital Status: Single

Phone: +90 312 286 48 45

e-mail: salihalan@gmail.com

### EDUCATION

Degree	Institution	Year of Graduation
MS	METU Mechanical Engineering	2009
BS	METU Mechanical Engineering	2006
High School	Çorlu M. Akif Ersoy Anadolu High School, Tekirdağ	2002

### WORK EXPERIENCE

Year	Place	Enrollment
2014-Present	TARU Engineering	Vibration Specialist
2006-2013	METU Dept. of Mechanical Engineering	Teaching Assistant

### FOREIGN LANGUAGES

Advanced English, Basic German, Basic Italian

### PUBLICATIONS

1. Alan S. and Çalışkan M. "Prediction of railway ground vibrations: an efficient hybrid numerical model with modal domain solutions" (in preparation)
2. Alan S. and Çalışkan M. "Transient response of large linear mechanical systems by modal domain solutions" (in preparation)

3. Alan S. and Çalışkan M. “Ground transient response calculation by finite difference modal analyses” (in preparation)
4. Barutçu, B. N., Alan, S. and Çalışkan, M., “Earthquake response analysis of Ankara high speed train station by finite element modeling”, accepted to presented at Internoise 2016, Hamburg, Germany, (2016).
5. Alan S. and Çalışkan M. “Vibration isolation design of railroad tracks within Ankara high speed train station”, Acoustical Society of America Proceedings of Meetings on Acoustics, v. 23, 065001 (2015)
6. Alan S. and Çalışkan M. “Prediction and assessment of environmental vibrations from railway operations on Marmaray”, Acoustical Society of America Proceedings of Meetings on Acoustics, v. 21, 065003 (2014)
7. Budak E., Tunç L. T., Alan S. and Özgüven H. N. “Prediction of workpiece dynamics and its effects on chatter stability in milling”, ”, CIRP Annals – Manufacturing Technology, v. 61, p. 339-342 (2012)
8. Alan, S. and Çalışkan, M., “Experience with random process theory on prediction of ground borne vibration from underground metro systems”, ICSV 18, Rio de Janeiro, Brazil (2011)
9. Alan S., Budak E. and Özgüven, H. N., “Analytical Prediction of Part Dynamics for Machining Stability Analysis”, International Journal of Automation Technology (special issue on Modeling and Simulation of Cutting Process), v. 4, n. 3, (2010)

## **HOBBIES**

Table Tennis, Turkish Classical Music, Puzzle and Sudoku (National team member since 2007)